FEDERAL UNIVERSITY OF SAO CARLOS

CENTER FOR EXACT SCIENCES AND TECHNOLOGY

GRADUATE PROGRAM IN MATERIALS SCIENCE AND ENGINEERING

Mg-CONTAINING MULTICOMPONENT ALLOYS PRODUCED BY HIGH-ENERGY BALL MILLING FOR HYDROGEN STORAGE

Felipe Marques

São Carlos-SP

2020

FEDERAL UNIVERSITY OF SAO CARLOS
CENTER FOR EXACT SCIENCES AND TECHNOLOGY
GRADUATE PROGRAM IN MATERIALS SCIENCE AND ENGINEERING

Mg-CONTAINING MULTICOMPONENT ALLOYS PRODUCED BY HIGH-ENERGY BALL MILLING FOR HYDROGEN STORAGE

Felipe Marques

Dissertation presented to the Graduate Program in Materials Science and Engineering as a partial requirement to obtain the title of MASTER IN MATERIALS SCIENCE AND ENGINEERING.

Supervisor: Prof. Dr. Guilherme Zepon
Co-supervisor: Prof. Dr. Haroldo Cavalcanti Pinto
Funding agencies: FAPESP - Grant number: 2018/08956-0 and 2019/01857-9
Serrapilheira Institute - Grant number: Serra-1709-17362
CNPq – Grant number: 139296/2018-2

São Carlos-SP
2020

Candidate's Vitae

Materials and Manufacturing Engineer from the University of São Paulo (2017)

UNIVERSIDADE FEDERAL DE SÃO CARLOS

Centro de Ciências Exatas e de Tecnologia
Programa de Pós-Graduação em Ciência e Engenharia de Materiais

Folha de Aprovação

Assinaturas dos membros da comissão examinadora que avaliou e aprovou a Defesa de Dissertação de Mestrado do candidato Felipe Marques, realizada em 20/02/2020:

Prof. Dr. Walter José Botta Filho
UFSCar

Profa. Dra. Kátia Regina Cardoso
UNIFESP

Prof. Dr. Guilherme Zepon
UFSCar

Certifico que a defesa realizou-se com a participação à distância do(s) membro(s) Guilherme Zepon e, depois das arguições e deliberações realizadas, o(s) participante(s) à distância está(ao) de acordo com o conteúdo do parecer da banca examinadora redigido neste relatório de defesa.

Prof. Dr. Walter José Botta Filho

ACKNOWLEDGMENTS

I would like to thank my supervisor Prof. Dr. Guilherme Zepon, for the brilliant orientation and for the opportunities that he provided for me during this project. I also want to thank my co-supervisor Prof. Dr. Haroldo Cavalcanti Pinto for his cooperation.I want to mention and acknowledge the contributions of Prof. Dr. Daniel Rodrigo Leiva and Prof. Dr. Walter José Botta Filho for the project, and I want to thank the whole LH_2M, especially Renato Belli Strozi and Flávio José Antiqueira. During this project, I had a glad opportunity of doing a research internship at Max-Planck-Institut für Kohlenforschung, in Germany. For this, I would like to thank the whole Schüth group, especially Dr. Michael Felderhoff, for his great cooperation. I also want to thank Frederik Wilkelmann for his cooperation and Jan Ternieden and Priv.-Doz. Dr. Claudia Weidenthaler for the XRD measurements.

This study was financed in part by the Fundação de Amparo à Pesquisa do Estado de São Paulo (FAPESP), grant number: 2018/08956-0 and 2019/01857-9, in part by the Serrapilheira Insitute, grant number: Serra-1709-17362, and in part by the Conselho Nacional de Desenvolvimento Científico e Tecnológico (CNPq), grant number: 139296/2018-2. This study was financed in part by the Coordenação de Aperfeiçoamento de Pessoal de Nível Superior – Brasil (CAPES) – Finance Code 001. The study was mainly developed using the facilities of the Department of Materials Engineering (DEMa) at the Federal University of São Carlos (UFSCar). I am also grateful to the Laboratory of Structure Characterization (LCE) of the Department of Materials Engineering at Federal University of São Carlos (DEMa/UFSCar) for the microscopy facilities, and the Brazilian Synchrotron Light Laboratory (LNLS) for the facilities and assistance with the in-situ XRD measurements, especially Dr. Santiago Jose Alejandro Figureroa.

I want to thank my family for supporting me during this project, especially my parents, Luís Claudio Marques and Rogéria das Graças Paduelo Marques, and my girlfriend Carolina Souza Bonfin. I want to thank God for his grace, which has been my motivation in every aspect of life, including over this project.

ABSTRACT

Hydrogen is a promising energy carrier that allows the use of energy in a sustainable form. However, safe and efficient hydrogen storage is a scientific and technological challenge that still has to be overcome. Recently it was reported that some high entropy alloys (HEAs), multicomponent alloys that crystallize as extended solid solutions with simple crystalline structures (BCC or FCC, for instance), present promising hydrogen storage properties. For example, TiVZrNbHf alloy, which forms a BCC single-phase structure, presented higher storage capacity than conventional hydrides. However, most of the papers published so far report compositions based only on transition metal elements, which limit the gravimetric capacities due to their densities. Since Mg is a low-density element promising for hydrogen storage, the study of Mg-containing multicomponent compositions is opportune. Recently, our research group studied an Mg-containing A_2B type HEA system, namely, $MgTiZrFe_{0.5}Co_{0.5}Ni_{0.5}$. This alloy formed a BCC structure when milled under argon, and this phase absorbs up to 1.2 wt.% of H_2 before it undergoes a phase transition to FCC hydride during absorption kinetics. The gravimetric capacity of the alloy would have been 3.5 wt.% H_2 (hydrogen over metal atoms - H/M=2) if the transformation to the dihydride phase had happened. This master project aimed to study the hydrogen storage behavior of new alloys for the Mg-Ti-Nb-Cr-Mn-Ni and Mg-Ti-Nb-Ni systems. For alloys selection, a thermodynamic model that allows predicting which compositions have the highest tendency to form single-phase microstructures based on extended solid solutions was tested. The selected alloys were produced by high-energy ball milling (HEBM) and evaluated in terms of phase formation and stability and hydrogen storage behavior. All the synthesized alloys formed solid solutions, but no single-phase was obtained and the formation of elemental segregation was observed. The $Mg_{22}Ti_{22}Nb_{22}Cr_{11}Mn_{11}Ni_{11}$ alloy synthesized under argon atmosphere and under hydrogen pressure absorbed 1.18 wt.% of H_2 and desorbed 1.6 wt.% of H_2, respectively. The $Mg_{21}Ti_{31}Nb_{31}Ni_{17}$ alloy synthesized under argon atmosphere and under hydrogen pressure absorbed 1.3 wt.% of H_2 and desorbed 2.26 wt.% of H_2, respectively. Based on these results, the method of alloy selection and the approach of using Mg-containing compositions could be analyzed.

Keywords: Hydrogen storage; Metal hydrides, Multicomponent alloys; Ball milling

RESUMO

LIGAS MULTICOMPONENTES CONTENDO Mg PARA O ARMAZENAMENTO DE HIDROGÊNIO

O hidrogênio é um vetor energético promissor para o uso de energia de forma sustentável. Contudo, o armazenamento seguro e eficiente de hidrogénio é um desafio científico e tecnológico a ser superado. Recentemente foi relatado que ligas de alta entropia (LAE), ligas multicomponentes que se cristalizam como soluções sólidas estendidas com estruturas cristalinas simples (CCC ou CFC, por exemplo), podem apresentar promissoras propriedades de armazenamento . A liga TiVZrNbHf, que forma uma estrutura monofásica CCC, apresentou maior capacidade de armazenamento do que os hidretos convencionais. Porém, os trabalhos publicados até o momento relatam composições baseadas apenas em metais de transição, que limitam as capacidades gravimétricas devido às suas densidades. Como o Mg possui baixa densidade e é promissor para o armazenamento de hidrogênio, o estudo de composições multicomponentes contendo Mg é oportuno. Recentemente, nosso grupo de pesquisa propôs um sistema LAE tipo A_2B contendo Mg, MgTiZrFe0.5Co0.5Ni0.5. A liga formou uma estrutura CCC quando moída sob Ar, absorvendo 1,2 p.% de H_2 antes de sofrer uma transição de fase para o hidreto CFC durante a cinética de absorção. A capacidade gravimétrica da liga seria de 3,5 p.% H_2 (hidrogênio sobre átomos metálicos - H/M=2) caso a transformação para o dihidreto fosse completa. Este projeto de mestrado estudou o comportamento de armazenamento de hidrogênio de novas ligas para os sistemas Mg-Ti-Nb-Cr-Mn-Ni e Mg-Ti-Nb-Ni. Na seleção de ligas, foi testado um modelo termodinâmico que permite prever quais composições têm a maior tendência a formar soluções sólidas monofásicas. As ligas foram produzidas por moagem de alta energia (MAE) e avaliadas em termos de formação e estabilidade de fase e comportamento de armazenamento de hidrogênio. Todas as ligas sintetizadas formarão soluções sólidas, porém nenhuma microestrutura monofásica foi obtida e a formação de segregação de elementos foi observada. A liga $Mg_{22}Ti_{22}Nb_{22}Cr_{11}Mn_{11}Ni_{11}$ sintetizada sob atmosfera de argônio e pressão de hidrogênio absorveu 1.18 p.% H_2 e dessorveu 1.6 p.% H_2, respectivamente. Já a liga $Mg_{21}Ti_{31}Nb_{31}Ni_{17}$ sintetizada sob atmosfera de argônio e pressão de hidrogênio absorveu 1.3 p.% H_2 e dessorveu 2.26 p.% H_2, respectivamente. Com base nesses resultados, o método de seleção de ligas e a abordagem de utilização de composições contendo Mg foi analisado.

Palavras-chave: Armazenamento de hidrogênio; Hidreto metálico; Ligas multicomponentes; Moagem

PUBLICATIONS

MARQUES, F.; ZEPON, G.; PINTO, H. C.; BOTTA, W. J.; Mg-containing multi-principal element alloy synthesized using high-energy ball milling (HEBM) for hydrogen storage - XVIII B-MRS Meeting – Balneário Camboriú-SC, Brazil, September 22-26, 2019.

MARQUES, F.; PINTO, H. C.; FIGUEROA, S. J. A.; WINKELMANN, F.; FELDERHOFF, M.; BOTTA, W. J.; ZEPON, G.; Mg-containing multi-principal element alloys for hydrogen storage: a study of the MgTiNbCr0.5Mn0.5Ni0.5 and Mg0.68TiNbNi0.55 compositions – World Congress on High Entropy Alloys HEA 2019 - Seattle- WA, USA, November 17-20, 2019.

x

TABLE OF CONTENTS

INDEX OF TABLES

INDEX OF FIGURES

1. INTRODUCTION

Researchers and leaders around the world have been rethinking the methods of generation, transportation, and consumption of energy due to climate change, pollution, and the greenhouse effect. It is clear that the current energetic system has to evolve to a system based on renewable sources and low carbon emissions. In this context, Brazil has a prominent position in the world because most of the energy generated in the country comes from hydroelectric power plants. Brazil also has a high potential for the utilization of alternative renewable sources by using wind turbines and solar panels, even though they are not extensively exploited nowadays. Moreover, Brazilian hydropower plants have seasonal regimes with a high flux of water from December to April (rainy season) and reservoirs with low levels from July to October (dry season). Solar and wind sources are complementary to the seasonal regimes of hydropower plants since the lower irradiation levels and wind speed are found in the rainy months. Thus, solar panels and wind turbines connected to the electric grid can save water of the reservoirs in the critical months of drought [1].

This scenario makes Brazil a place with favorable conditions to become a country with an energy system largely based on renewable sources. However, for an energy system based on renewable sources to be efficient, economically favorable, and sustainable, technologies for Electrical Energy Storage (EES) are necessary. EES allows the conversion of electrical energy coming from a plant into a form that can be stored. When electrical energy is needed, the stored energy can be converted again. ESS allows energy to be produced at times of low demand and/or low generation cost or from intermittent energy sources (solar and wind, for example), and this same energy to be used at times of high demand, high production cost or when no other means of production is viable [2].

Hydrogen is considered the ideal energy carrier to exploit the benefits of renewable sources such as solar, wind and hydro. The energy generated by these sources can be used to produce hydrogen by several hydrolysis techniques [3]. Although the efficiency of hydrolysis techniques is not yet at their highest, many efforts have been made to improve the efficiency of water to hydrogen conversion. After hydrogen generation and storage, it can be used in fuel cells to

generate electricity again, in an electrochemical reaction whose byproduct is water, closing the environmentally friendly cycle. Thus, fuel cells are electrochemical devices that, basically, promote an electrochemical reaction between hydrogen and oxygen, generating water and electricity. There are plenty of fuel cell types and the technology is considered mature [4,5]. Among the fields of hydrogen production, storage and conversion to electricity, the storage field is the most undeveloped [6]. Therefore, one of the most urgent technological challenges for implementing this type of EES is to develop ways to store hydrogen safely, efficiently and cost-effectively.

In its gaseous form, hydrogen has a high gravimetric energy density of 120 MJ/kg (compared to 45 MJ/kg of gasoline). However, its volumetric energy density is low, only 1.9 MJ/l when stored at 20 MPa and 8.5 MJ/l when stored in the liquid state at -253 º C (compared to 31 MJ/l for gasoline). Due to this low volumetric energy density, researchers from universities, companies, and research centers around the world have been working to develop suitable materials for storing hydrogen in solid form [7].

Among the options for solid-state hydrogen storage, metal hydrides are one of the most promising [6]. These hydrides have been studied for decades and some materials, such as $LaNi_5$ and MgH_2, are available in the market [8]. Although there are already metal hydrides with commercial applications, no material yet meets all the requirements for stationary storage of hydrogen, and the field requires the design of better materials [6].

Recent works reported in the literature have shown that some HEA present interesting properties that can be exploited for application in hydrogen storage. High entropy alloy is a new alloying concept based on multi principal elements and can be defined as alloys with five or more alloying elements mixed in atomic concentrations between 5% and 35% [9]. TiVZrNbHf and TiZrNbHfTa alloys are examples of HEAs capable of absorbing considerable amounts of hydrogen [10,11]. However, most of the compositions proposed are based just on transition metal elements, which might limit the hydrogen storage gravimetric capacities due to their densities (<2.7 wt.% of H_2). One Mg-containing HEA, namely $MgTiZrFe_{0.5}Co_{0.5}Ni_{0.5}$, was proposed and classified as an A_2B type HEA, where

A is hydride forming metals (A = Mg, Ti, V, Zr, Nb, Hf, Ta) and B are transition metals with lower hydrogen affinity (B = Mn, Cr, Fe, Co, Ni) [12]. According to the authors, in the fully hydrogenated state, this alloy would have absorbed 3.5 wt.% of H_2, which motivates further investigations in similar compositions [12].

This master project proposed the study of new A_2B type HEA compositions based on the Mg-Ti-Nb-Cr-Mn-Ni system and derived compositions based on the Mg-Ti-Nb-Ni system, produced by high energy ball milling (HEBM) for hydrogen storage. In the selected alloys, a high tendency of formation of single-phase solid solutions was sought to facilitate the correlation of hydrogen storage properties with a characterized phase, avoiding study limitations due to the interaction between phases.

2. LITERATURE REVIEW

2.1 Multicomponent alloys for hydrogen storage

Several types of materials, such as hydrides (ionic, covalent, or metallic), amides ($Mg(NH_2)$), zeolites, etc., have been studied for the application of hydrogen storage [7]. Among these, metal hydrides are one of the most promising alternatives for solid-state hydrogen storage due to their high gravimetric and volumetric capacities, besides being a safe method of storage [13]. Most of the metallic elements can form hydrides, as can be seen in Figure 1, however, their dissociation pressures and operation temperatures are not adequate for most practical applications (temperatures between 0 and 100 ºC and hydrogen pressures between 1 and 10 bar). Only vanadium meets these criteria; however, its reversible gravimetric capacity is still very low.

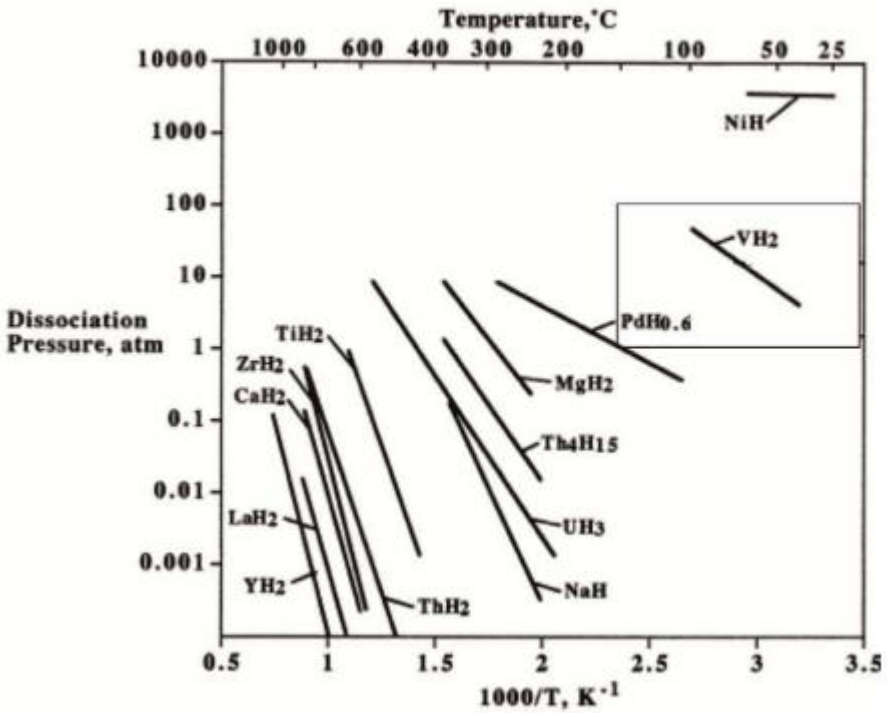

Figure 1: Dissociation pressure as a function of the temperature of some metal hydrides. The box delimits the appropriate operating range for practical applications in hydrogen storage (0-100 °C and 1-10 atm), taken from [14].

In the last decades, several alloys and composites have been studied aiming the application of hydrogen storage. The most important systems with the

greatest potential for technological application are Mg-based hydrides, complex hydrides (mainly Mg, Al or Li based), solid solutions with BCC structures (such as Ti-Cr-V system alloys) and intermetallic compounds from the AB, A_2B, AB_2, and AB_5 families, where A is hydride forming metals and B are typically transition metals (e.g., TiFe, Mg_2Ni, ZrV_2, and $LaNi_5$) [15,16,25–28,17–24]. Yet, no material meets all the requirements for stationary storage of hydrogen so far, and the field requires the design of better materials [6].

HEAs belong to a new class of metallic materials which, unlike conventional metallic alloys, are multicomponent alloys with five or more elements in close stoichiometric proportions. This new alloy concept was presented by Cantor, B. et. al. [29] in a publication in which the author described the first attempt to explore the central regions of the phase diagrams of multicomponent alloys. The major discovery was that, despite the high number of elements, the equiatomic CrFeNiCoMn alloy crystallized in a single-phase disordered solid solution with a face-centered cubic structure (FCC). In the same year, another research group in Taiwan reported some publications showing that other systems were also able to form multicomponent solid solutions with interesting properties [9,30]. The explanation for the formation of extended solid solutions instead of multiphase microstructures (with intermetallics, for example) was that the contribution of configurational entropy to the free energy of solid solutions in alloys with five or more elements allows this phase to be more stable in relation to a mixture of phases. Hence the name "high entropy alloys." The discovery of these alloys represented the beginning of a new field of metallurgy, which has as object study the center of phase diagrams instead of their edges. Since then, this new class of metallic materials has been extensively studied by researchers from all over the world [31,32].

Currently, there are two definitions for HEA [33]: (i) based on chemical composition: HEAs are alloys that contain at least five main elements in atomic fractions ranging from 5% to 35%. Thus, the Mn-Cr-Fe-Co-Ni system, for example, presents an equiatomic composition, several non-equiatomic compositions, and numerous compositions with additions of minority elements,

and (ii) based on configurational entropy: HEAs are defined as alloys that present configurational entropy (determined according to equation 1) greater than 1.5R.

$$S_C = -R\sum_{i=1}^{n} c_i ln c_i \qquad (1)$$

Being c_i the molar fraction of the ith component and R the universal constant of gases. According to definition (i) the minimum number of major elements in HEA is five, and because alloys with five equimolar elements have configurational entropy equal to 1.61R, 1.5R was stipulated as a reasonable value to define HEA. It should be noted that the definitions of HEAs described above do not limit this class of alloys to those that form only one solid solution, i.e., single phase. HEAs with one, two or more phases that may comprise different solid solutions or mixtures of solid solutions with intermetallic phases have been reported [31,34–39]. Multicomponent alloys that do not meet the HEA definitions are often called multiprincipal element alloys (MPEAs) [31].

Recently, the hydrogen storage properties of some HEAs and MPEAs have attracted attention. Kao, Y. et. al. [40] reported the hydrogen storage properties of alloys of the Co-Fe-Mn-Ti-V-Zr system with different Ti, V, and Zr contents. All studied alloys (processed by arc melting) presented microstructures composed of different multicomponent solid solutions with crystalline structures of the C14 Laves phase. The authors showed that some of these alloys are able to absorb significant amounts of hydrogen. For example, CoFeMnTiVZr2.6 alloy absorbed approximately 1.7 wt.% of H_2 (equivalent to a ratio of hydrogen atoms to metal atoms - H/M - of 1.15) at 25 ºC and 20 bar of H_2. Kunce, I. et. al. [41,42] reported the hydrogen storage properties of ZrTiVCrFeNi and TiZrNbMoV HEAs produced by laser fusion. The microstructure of the first alloy is mainly composed of a multicomponent solid solution with a C14 structure. The hydrogen storage properties were evaluated by PCI (pressure-composition-isotherm) measurements using Sievert-type apparatus. The results showed that after two hours of thermal activation at 500 ºC, PCI measurements at 50 ºC and 10MPa of H_2 indicated a hydrogen storage capacity of 1.8 wt.% of H_2. On the other hand,

the TiZrNbMoV alloy presented a more complex microstructure composed of a matrix formed by a multicomponent solid solution with a body-centered cubic structure (BCC) combined with an orthorhombic phase of TiNb4 type. Despite the complex microstructure, this alloy was able to absorb 2.5 wt.% of H_2 in less than 25 minutes without any kind of previous activation treatment at room temperature and 85 bar of H_2.

M. Sahlberg et al. [10] reported that the equiatomic TiVZrNbHf alloy has a storage capacity of hydrogen with an H/M of 2.5, which is considerably higher when compared to conventional hydrides that typically have H/M = 2. This alloy crystallizes with a single-phase BCC structure; however, when hydrogenated, the alloy undergoes a structural transformation forming a body-centered tetragonal structure (a type of distorted FCC structure). In the classical BCC alloys, like in the case of TiCrV alloys, hydrogenation begins with hydrogen entering by solid solution at the octahedral sites of the BCC lattice. At some point, a metallic hydride with FCC lattice and with hydrogen occupying the tetrahedral sites (in a CaF_2 type structure) is formed [27]. What calls attention is that for an H/M ratio of 2.5 the hydrogen has to occupy all the tetrahedral sites and 50 % of the octahedral sites of the FCC structure, which may be the reason why the authors found a BCT structure (distorted FCC) [10].

Continuing the research with the HfNbTiVZr HEA, M. Sahlberg et al [43] studied the mechanisms of hydrogen absorption through *in situ* XRD and *in situ* and *ex situ* neutron diffraction. By neutron diffraction, it was possible to verify that hydrogen (deuterium) occupies the tetrahedral and octahedral sites of the tetragonal structure formed at high temperature and pressure (500 °C and 50 bar D_2), although at room temperature the data indicated both the formation of tetragonal phase or cubic phase (CaF_2 type), with D occupying primarily the tetrahedral interstitial sites. Still, according to the authors, the hydrogen storage is reversible in this alloy at 500 °C and the elevated values of the atomic radii mismatch (δ) seem to facilitate the occupation of hydrogen in unexpected interstitial positions since it is believed that this atomic radii mismatch causes an internal lattice strain [43]. C. Zlotea et al. [44] studied the absorption/desorption of TiZrNbHfTa alloy, in which the element Ta replaces the V of HfNbTiVZr alloy

studied in [43]. The hydrogen absorption of TiZrNbHfTa alloy caused the two-stage structural transformation from initial BCC to body-centered tetragonal (BCT), with the formation of a hydride with H/M=1, followed by a transformation from BCT to FCC when reaching H/M=2. Unlike the BCT (distorted FCC) found in [10], this latter BCT is the result of the expansion of the BCC structure in the c axis. This behavior is in accordance with that observed for classical BCC alloys, however, in contrast with the results obtained in [43], in which hydrogen absorption was recorded in one step with the formation of a BCT hydride with H/M=2.5. Given these results, the authors suggested that the lattice deformation caused by the atomic radii mismatch (δ) presents an important role, that is, higher values of δ (found in [43]) may favor the reaction with hydrogen in only one stage (BCC → body-centered tetragonal (distorted FCC), with higher hydrogen absorption), while small values of δ (found in [45]) favor the reaction in two stages (BCC→ body-centered tetragonal (expanded BCC)→ FCC), also observed in conventional BCC alloys [45].

The atomic radii mismatch (δ) is an estimate of the difference between the atomic radii of the elements of the solid solution and can be calculated by equation 2.

$$\delta = \sqrt{\sum_{i=1}^{n} x_i \left(1 - \frac{x_i}{\sum_i^n x_i\, r_i}\right)^2} \quad (2)$$

where n, x_i, and r_i are the total number of alloy elements, the molar fraction and the atomic radius of the ith element, respectively [46]. If this delta parameter (δ) is high, the alloy tends to precipitate new phases [47]. This is based on the principle of Hume-Rothery, according to which for a solid solution to exist, the atomic radius of the solutes and solvents must be close. The term $\sum_i^n x_i\, r_i$, present in equation 2, corresponds to the average of the atomic radii of the alloy elements. The delta parameter and the mean of the atomic radius have been applied in the design of high entropy alloys [42,46].

Motivated by the results presented by Sahlberg et al. [10], Nygård *et al*. [48] investigated the structure and hydrogen storage properties of a series of HEAs based on Ti, V, Zr, Nb, and Ta. The authors intended to evaluate the influence of the varying degree of local lattice strain (δ) on the hydrogen storage properties. The alloys crystallize into a BCC structure and form FCC hydrides with H/M close to 2. However, no correlation between the hydrogen storage capacity and the local lattice strain was observed, which left the topic of the influence of δ on hydrogen storage properties under debate. Recently, the same group has studied a group of HEAs related to the ternary system TiVNb. These alloys also have BCC crystal structure and form FCC hydrides with H/M close to 2. The authors found that a larger expansion of the lattice during phase transition (BCC to FCC) may destabilize the metal hydrides, and the destabilization can be tuned by changing the valence electron concentration (VEC). Based on this, the group proposed the $TiVCrNbH_8$ as a suitable material for hydrogen storage [49]. Recently, Montero *et al*. [50] reported the synthesis optimization, physicochemical, and hydrogen storage properties of $Ti_{0.325}V_{0.275}Zr_{0.125}Nb_{0.275}$ multiprincipal element alloy. The alloy was synthesized both by arc melting and ball milling under Ar, forming a BCC phase that transforms into a BCT dihydride with a maximum hydrogen uptake of 1.7 H/M (2.5 wt.% H_2). The dihydride could be directly synthesized by reactive ball milling under hydrogen pressure, and this material presented the best hydrogen sorption properties.

Hitherto, HEAs and multiprincipal element alloys that crystallize into BCC or Laves phase structures have shown high potential for the development of new metal hydrides with excellent storage properties for practical applications. However, most of the compositions proposed are based just on transition metal elements, which might limit the hydrogen storage gravimetric capacities due to their densities. Mg is a promising element in terms of hydrogen storage, and the study of Mg-containing compositions may be interesting for the development of low-density multi-principal element alloys for hydrogen storage.

In the work of our research group, the behavior during hydrogenation of a new HEA, the $MgZrTiFe_{0.5}Co_{0.5}Ni_{0.5}$ alloy, was studied [12]. This HEA was

proposed by our group and its composition was based on the composition of A_2B type Mg-based complex hydrides, such as Mg_2FeH_6, Mg_2CoH_5 and Mg_2NiH_4 [20,22,23]. It is well known that the addition of transition metals such as Fe, Co, Ni, Mn, which are elements that form very unstable hydrides, alter the hydrogen properties of hydride forming metals such as Mg, Zr, Ti, V, etc., altering mainly the enthalpies of hydrogenation. Thus, our group named this alloy as an A_2B type HEA, where A is hydride forming metals and B are transition metals.

The $MgZrTiFe_{0.5}Co_{0.5}Ni_{0.5}$ alloy was produced by two routes, HEBM under 0.7 MPa of Ar atmosphere, called mechanical alloying (MA) and reactive milling (RM) under 3.0 MPa of H_2. In both processes, the alloy was produced from the pure elements. Both MA and RM were performed in a planetary type mill, with a rotation speed of 600 rpm, a ball-to-powder ratio of 40:1 and a milling time of 24 h. Such process parameters were selected based on the experience of the LH_2M/DEMa/UFScar research group in the synthesis of nanostructured magnesium-based hydrides by RM [20,22,23].

Figure 2a shows the X-ray diffraction pattern (XRD) of $MgZrTiFe_{0.5}Co_{0.5}Ni_{0.5}$ alloy prepared by MA, in which only one BCC phase with a lattice parameter of a = 3.075(6) Å is observed. Figure 2b shows the XRD pattern of the same RM alloy, which has been indexed as a single FCC phase with a lattice parameter of a = 4.642(6) Å [12]. In both cases, the lattice parameters were determined by Rietveld refinement. Thermal analysis, such as Differential Scanning Calorimetry (DSC) coupled with mass spectroscopy (MS), hydrogen absorption kinetics measurements using Sievert-type apparatus and *in situ* XRD experiments using synchrotron radiation were used to investigate the behavior of this alloy during hydrogen absorption/desorption. It was shown that during hydrogenation, the alloy that has BCC structure begins to absorb hydrogen by solid solution without any phase transformation occurring until a certain hydrogen content is reached. From a given hydrogen content, the alloy undergoes a structural transformation forming the FCC phase, the same obtained when the alloy is processed by RM. The results presented in Figure 3a and Figure 3b show that this alloy was able to absorb about 1.2 wt.% of H_2 in 1.5 h at 350 °C and 2 MPa of H_2. The full transformation to the dihydride phase (H/M=2) was not

complete due to kinetics and thermodynamics hindering, but if it had happened, the gravimetric capacity of the alloy would have been 3.5 wt.% H_2.

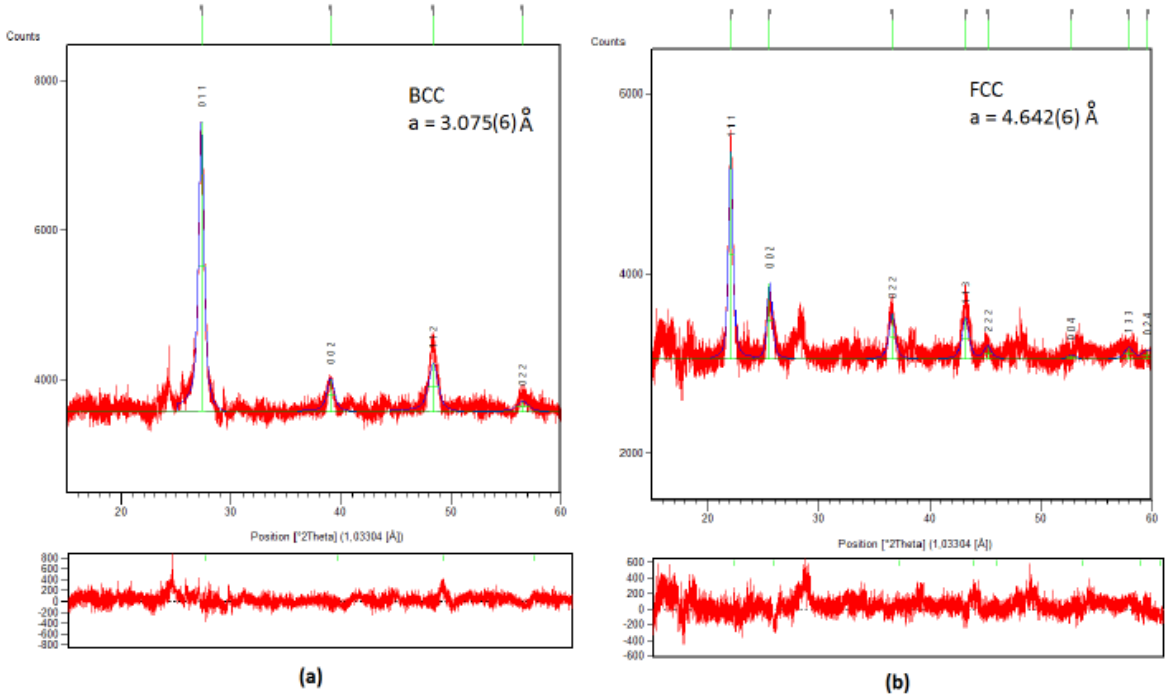

Figure 2: In situ XRD of $MgZrTiFe_{0.5}Co_{0.5}Ni_{0.5}$ alloy and Rietveld refinement of (a) sample produced by MA under 0.7 MPa of Ar; and (b) sample produced by RM under 3.0 MPa H_2 [12].

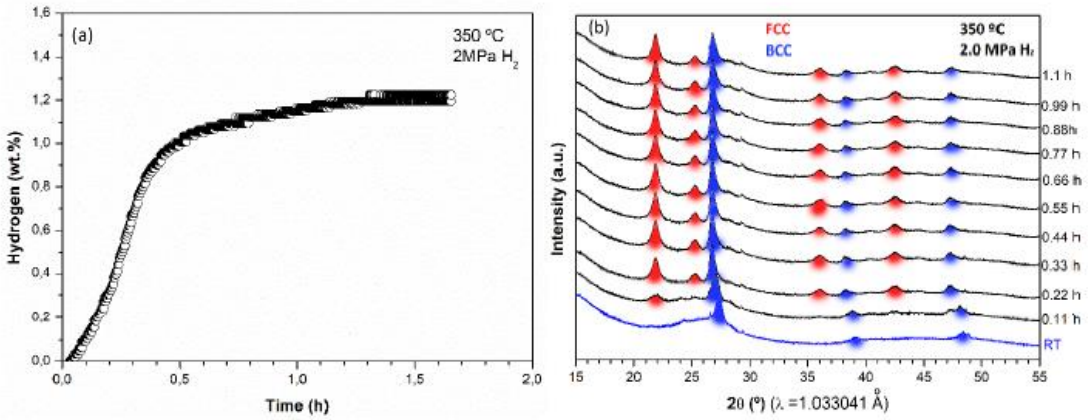

Figure 3: (a) Kinetic curve of hydrogen absorption at 350 ºC and 2MPa of H_2 of $MgZrTiFe_{0.5}Co_{0.5}Ni_{0.5}$ alloy produced by MA under 0.7 MPa of Ar. (b) In-situ XRD of $MgZrTiFe_{0.5}Co_{0.5}Ni_{0.5}$ alloy under 2 MPa of H2 and at 350 ºC [12].

These results showed that the $MgZrTiFe_{0.5}Co_{0.5}Ni_{0.5}$ A_2B-type HEA with BCC structure could be easily synthesized by MA and, in addition, that the

hydride $MgZrTiFe_{0.5}Co_{0.5}Ni_{0.5}H_x$ can be easily produced by RM under hydrogen atmosphere. Such results are very promising and encouraging since HEBM is a simple and fast processing route to investigate new HEA and multi-principal element compositions with good hydrogen storage properties.

The present work proposed the investigation of the hydrogen storage behavior of new Mg-containing A_2B type HEAs and multiprincipal element alloys processed by HEBM. One of the great attractions in the multicomponent alloys study is the enormous range of compositions not yet exploited. However, this makes the selection of compositions to be studied a complicated task, given a large number of possibilities. Thus, the selection of the alloys that were studied in this project was carried out through the use of thermodynamic models that allowed evaluating the compositions with a greater tendency to form extended solid solutions and single-phase microstructures. Furthermore, the atomic radii mismatch (δ) and the mean atomic radii that may be related to hydrogen storage properties were taken into account. Only the compositions with hydride forming elements besides Mg (A =Ti, V, Zr, Nb) and transition metals elements used to change the hydrogen storage properties (B = Cr, Mn, Fe, Co, and Ni) were considered. The following section presents the thermodynamic model that was used.

2.2. Criteria for selecting multicomponent compositions

Since the advent of HEAs, many authors have proposed different models to select multicomponent compositions capable of forming extended solid solutions and single-phase microstructures with promising properties [48,49,51,52]. In the present work, the thermodynamic parameter model φ proposed by Ye, Y.F, et al. was used [52]. In this model, the authors use some thermodynamic parameters, such as configurational entropy, excess entropy, mixing enthalpy and possible atomic packing to predict if an alloy will be single-phase or multiphase. The problem was formulated based on the theory established by G.A. Manssori et al. [53] in 1970, which says that the total entropy of an alloy (S_T) can be expressed according to equation 3, in which S_C is the mixing entropy for an ideal gas (calculated according to equation 1) and S_E is the

mixing entropy of excess, which is a function of atomic packing and atomic sizes of the alloy's elements. The equations for calculating S_E are presented in Appendix I at the end of this text.

$$S_T = S_C + S_E \quad (3)$$

Thus, the Gibbs free energy (Ga) of an alloy can be described according to equation 4, where Ha is the enthalpy of the alloy and T is the temperature.

$$G_a = H_a + TS_T \quad (4)$$

The enthalpy of the alloy (Ha) can be estimated according to Miedema's model, where Ha is expressed according to equation 5, where ΔHij is the mixing enthalpy of the ith and jth elements and Ci the composition of the ith element and Cj the composition of the jth element [54].

$$H_a = \sum_{i \neq j} 4\Delta H_{ij} c_i c_j \quad (5)$$

For entropy to be the parameter that controls the stability of a phase, at a given T, it is necessary that $|TS_T| \gg |Ha|$. Since S_E is always negative because it computes the deviation from the ideal model and S_C is always positive, we have $|TS_T| = T(S_C - |S_E|)$, and the criterion for dominance of entropy in phase stability can be formulated according to equation 6.

$$\frac{|S_E|}{S_C} \ll 1 - \frac{|H_a|}{TS_C} \quad (6)$$

In order to satisfy this inequality, it is necessary that S_c or T to be high, which agrees with the initial idea that alloys with higher configurational entropy tend to stabilize single-phase microstructures. However, only the values of S_c and T are not sufficient to guarantee the formation of single-phase alloys, since $|Ha|$ and $|S_E|/S_C$ must also be taken into account, and $|S_E|/S_C$ is related to the difference between the atomic size of the alloy elements and the atomic packaging.

Therefore, Ye. Y.F. et al. [51] proposed an adimensional thermodynamic parameter φ (phi), described according to equation 7, to be used in HEA design.

$$\varphi = \frac{S_C - S_H}{|S_E|} \quad (7)$$

S_H is defined as the complementary entropy derived from the enthalpy and is given by S_H=|Ha|/Tm, where Tm is the melting temperature of the alloy calculated according to the mixing rule, i.e., the weighted average of the melting temperature of the pure elements of the alloy. It is worth mentioning that the melting temperature was adopted because this parameter was created for application in alloys produced by casting.

To achieve a high entropic effect, it is necessary to maximize the parameter φ. In [52] the parameter φ was calculated for more than 50 types of HEA reported in the literature and it was verified whether there was a correlation between the value of this parameter and the tendency of single-phase or multiphase structures formation. Figure 4 shows this result in a graph where the parameter φ is plotted against S_C for the analyzed alloys. It can be observed that for the same Sc values both single-phase and multiphase alloys can be formed, indicating that only the Sc value is not sufficient to predict whether an alloy will form a single extended solid solution or a multiphase structure. On the other hand, it is clear that for higher values of φ the higher is the tendency of an alloy to be single-phase. The authors stipulated the critical value of φcrit = 20, above which only single-phase alloys are formed. Between φ=11 and φ=20 there is a region where both single-phase and multiphase are obtained. With this, the calculation of φ parameter can be used as a tool to select potential HEA compositions with a higher tendency to form single-phase alloys.

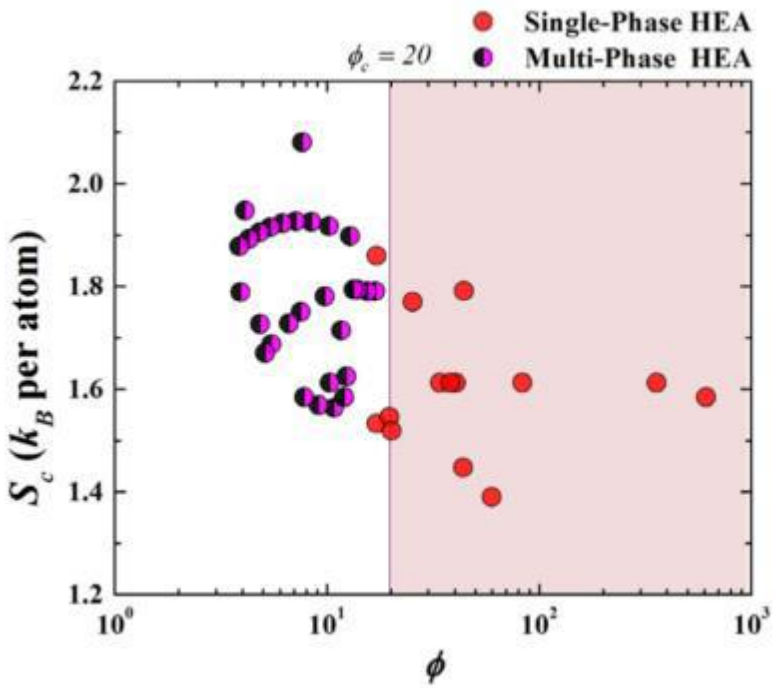

Figure 4: S_C versus φ plotted for a variety of HAE [52].

3. MATERIALS AND METHODS

3.1 Alloys selection

A_2B type HEAs and derived compositions that contain Mg as light element were selected to be studied. The main hydride forming metallic elements besides Mg were selected as A elements: Ti, V, Zr and Nb; and as B elements the main transition metals used to alter the hydrogen storage properties of metal hydrides were selected, being them: Cr, Mn, Fe, Co, and Ni. If only the compositions with six elements are considered, that is, with three type-A elements (one of them being Mg) in equal proportions and three type-B elements in equal proportions, a total number of 60 alloys could be studied. The number of alloys would be even greater if the quinary alloys are considered, that is, with two elements A (one of them being Mg) and three elements B or with three elements A (one of them being Mg) and two elements B. For the selection of alloys, the thermodynamic parameter φ was calculated for all 60 possible alloys with six elements (with type-A elements in equal proportions and type-B in equal proportions). The alloys with the highest values of φ were selected for the definition of A_2B type alloy systems to be analyzed. However, since, for a given system, the composition with an equiatomic ratio between type-A elements and between type-B elements is not necessarily the one that maximizes the tendency of solid solution formation (i.e. which maximizes the φ parameter), it had to be defined which exact alloy composition would maximize this parameter. A tool developed in MATLAB by the group of Dr. Yang from the City University of Hong Kong and adapted by the group of LH_2M/DEMa/UFSCar was used to calculate the φ parameter of more than 1300 alloy compositions of a given system and present the result in a ternary diagram. For example, considering the Mg-Ti-Zr-Fe-Co-Ni system, one can optimize the composition of the A_2B type as follows: Initially, the alloys with compositions $(Mg_xTi_yZr_z)_2(Fe_{0.33}Co_{0.33}Ni_{0.33})$ are considered, with x, y and z being the relative fraction of the hydride forming elements A (i.e. x+y+z=1). Through the developed MATLAB program the value of the φ parameter of different alloys can be calculated with contents of Mg, Zr, Ti varying from 2%at. in 2%at., and keeping the contents of Fe, Co and Ni equal (in this case, equiatomic). The values of φ for these alloys are shown in Figure 5a. With this, it is possible to determine the

relative fractions of Mg, Zr and Ti that maximize the parameter of interest. In this case, the values that maximize the parameter φ are x = 0.6, y = 0.25 and z = 0.15. Then, these values are fixed and it is verified which relative fractions (u, v and w) values of the transition metal elements B maximize the parameter φ for the alloy $(Mg_{0.6}Ti_{0.25}Zr_{0.15})_2(Fe_uCo_vNi_w)$. Figure 5b shows the values of φ for the different compositions in terms of Fe, Co and Ni. It can be verified that in this case the composition that would be selected considering only the maximization of the φ parameter and therefore would increase the tendency of forming solid solution is $(Mg_{0.6}Ti_{0.25}Zr_{0.15})_2(Fe_{0.5}Co_{0.3}Ni_{0.2})$.

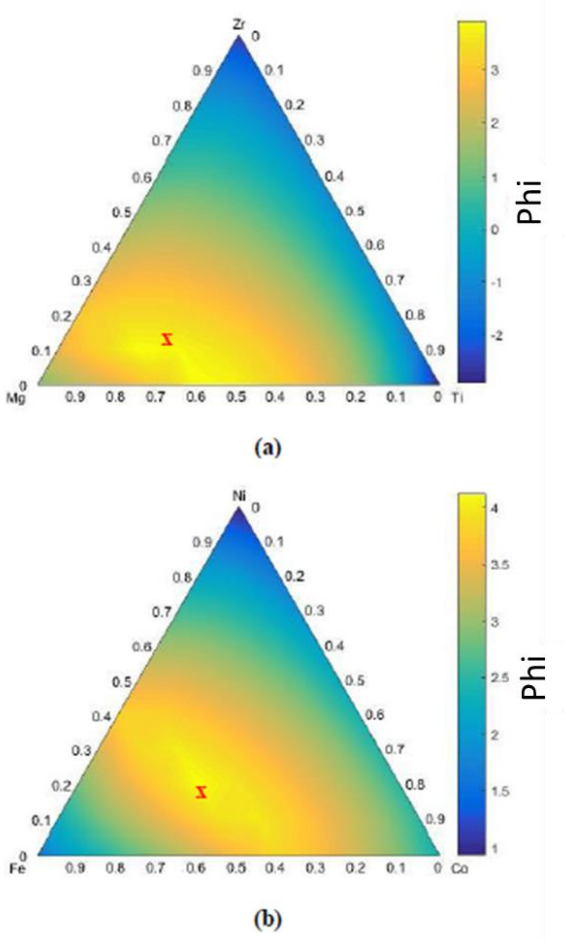

Figure 5: (a) φ parameter of $(Mg_xTi_yZr_z)_2(Fe_{0.33}Co_{0.33}Ni_{0.33})$ alloys. (b) φ parameter of $(Mg_{0.6}Ti_{0.25}Zr_{0.15})_2(Fe_uCo_vNi_w)$ alloys. The X in red marks the compositions selected in each case. The final composition of the selected alloy would be $(Mg_{0.6}Ti_{0.25}Zr_{0.15})_2(Fe_{0.6}Co_{0.3}Ni_{0.2})$.

However, the empirical delta (δ) and mean radius parameters were also evaluated in order to select compositions that result in the simultaneous optimization of the analyzed parameters. The methodology used to calculate, optimize and represent the data of the empirical parameters was the same as the one used for the thermodynamic parameter φ, that is, each empirical parameter was calculated according to its respective model for the compositions varying A and then varying B and the results were represented graphically. For the delta parameter, the highest possible values were desired. Although higher values of delta lead to the higher tendency of formation of secondary phases, only with the maximization of this parameter its influence on hydrogen storage properties could be analyzed. For the mean atomic radius, values above 1.35 Å were considered ideal, since for conventional BCC alloys the best absorption results are verified when the structure has lattice parameters above 3 Å (i.e., mean radius > 1.30 Å), as larger lattice parameters result in greater interstitial space and consequently a greater number of sites available for hydrogen [27].

For the selection of the specific composition within the regions of interest, both for the calculated parameters varying the elements A and B, two conditions were considered: (i) the composition in which φ was maximized and (ii) the composition in which δ was maximized, and for both conditions the mean radius value should be greater than 1.35 Å. In addition, the A_2B equiatomic composition of each system were also selected. Here, equiatomic means that all the elements A has the same atomic proportion among them, i.e., they are in equiatomic proportion, and so are the B elements. Given this proportion, A and B elements are equiatomic among them, but considering the whole composition the A_2B proportion is obtained.

After selecting the three compositions of the same system, they were produced and their hydrogen storage properties were evaluated.

Moreover, the influence of the synthesis process (mechanical alloying and reactive milling) on phase formation and alloy's hydrogen storage behavior was evaluated, and a comparative analysis between the selected A_2B system and a derivative system was performed.

3.2 Synthesis of the alloys

The selected multicomponent alloys were produced through the process of high energy ball milling (HEBM) under an atmosphere of 0.7 MPa of argon (Ar), called mechanical alloying (MA), and under an atmosphere of 3.0 MPa of hydrogen (H_2), called reactive milling (RM). All the milling processes were conducted from the pure elements in powder form. The metallic elements were weighted and placed inside a sealed steel milling vial (volume 250 cm^3) with steel balls (15 balls with 8 mm and 10 balls with 10 mm diameter). The ball-to-powder ration was 20:1. After sealing, the milling vials were submitted to five cycles of evacuation and purge with argon. The ball milling was performed in a Fritsch Pulverisette 6 model planetary mill, with a rotation speed of 600 rpm and milling time of 24 h. The powders resulting from the milling process were handled inside a MBRAUM glove box under an argon protective atmosphere. The glove box used is equipped with a gas purification system that keeps the H_2O and O_2 levels below 0.1 ppm. After ball milling, the samples were heat treated at 350°C for 12 h under dynamic vacuum in the Sievert-type apparatus. The objective of the heat treatment was to evaluate the thermal stability of the phases produced by milling.

3.3 Structural and microstructural characterization

Powder XRD for phase analysis was carried out using a D8 Advanced Eco from Brucker equipped with a Cu radiation (1.5406 Å) source. A generator setting of 40 kV and 20 mA was applied to the generator of X-rays. Data were collected in the 2θ range between 20 and 90° with a step width of 0.02°. The measuring time per step was 0,2 s. Moreover, it was used a Stoe STADI P transmission diffractometer using Mo radiation (0.70930 Å). The instrument is equipped with a primary Ge (111) monochromator ($MoK\alpha_1$) and a position-sensitive Mythen1K detector. A generator setting of 50 kV and 40 mA was applied for the generation of X-rays. Data were collected in the 2θ range between 5 and 50° with a step width of 0.015°. The measuring time per step was 40 s. For each sample, either 4 or 8 scans were collected and summed after data collection. For the measurements, the samples were filled into glass capillaries (0.5 mm). The in-situ XRD was also performed in the Stoe STADI P transmission diffractometer

from 30°C to 500°C. Data were collected in the 2θ range between 10 and 35° with a step width of 0.5°. The measuring time per step was 40 s. For each temperature, 4 scans were collected and summed after data collection. The measured patterns were evaluated qualitatively by comparison with entries from the ICCD PDF-2 powder patterns database and by comparison with simulated data (crystal structure data were taken from the ICSD database).

Microstructure examination and chemical microanalysis were executed by SEM using a FEG Philips XL-30 microscope equipped with Bruker Nano XFlash 6|60 EDX Detector, and TEM using a FEG FEI Tecnai G^2F20 microscope equipped with EDAX EDX detector and a cold FEG Hitachi HD-2700 C_S-corrected dedicated STEM 200 kV equipped with EDAX Octane T Ultra W 200 mm^2 SDD EDX detector.

In-situ synchrotron powder XRD was executed at the Brazilian Synchrotron Light Laboratory (LNLS) in Campinas-SP at XRD1 beamline [55]. The equipment set up is composed of a 3-circle heavy-duty diffractometer from Newport® and a Linear MYTHEN 24 K detector system from DECTRIS®, which allows high-speed data acquisition. The X-ray wavelength selected was 1.033041 Å (12 keV). During preparation, the samples were diluted in amorphous silica to avoid strong X-ray absorption and encapsulated in a specially developed quartz capillary cell located at the geometry center of the goniometer, which allowed either working under He flow or H_2 pressure. A gas blower model GSB1300 was used to heat the capillary cell up to 550 °C. For the alloys synthesized by MA, the in-situ hydrogen absorption measurement protocol consisted of heating the samples in two-step ramps (from 50 °C to 450 °C and from 450 °C to 550 °C) under 4 MPa of H_2 pressure and then cooling down the system to room temperature keeping the H_2 pressure. A complete XRD pattern was collected every two minutes during heating ramps and room temperature plateau for both alloys. The hydrogen desorption protocol for the alloys synthesized by RM consisted of heating the samples stepwise, keeping the plateau temperature for ten minutes, and then cooling down the system to room temperature at the end of the heating process. For the stepwise heating process, two heating rates (10 °C min^{-1} for the 100 °C steps and 5 °C min^{-1} for the 50 °C

steps) were applied. During measurements, the capillary system was kept under He flow, and a complete XRD pattern was collected every five minutes on the temperature plateaus. Pawley Fit of all the XRD patterns was done using GSAS-II software in which mainly scale factor, background, and lattice parameters were refined.

3.4. Hydrogen storage properties evaluation

The hydrogen storage properties of the HEAs produced by HEBM were evaluated through volumetric techniques using a Sievert-type apparatus of the SETARAM PCTPro model (E & E version). Measurements of hydrogen absorption kinetics at 350 °C of temperature and around 60 bar of H_2 were performed.

Thermal analysis was performed by using a Mettler Toledo TGA/DSC 1 (heating rate: 10 ºC min^{-1}) with a gas controller GC 200 (argon flow: 50 mL min^{-1}) coupled with a ThermoStar GSD 300 T2 MS gas analyzer for detection of H_2 (2g mol^{-1}).

Pressure-Composition-Isotherm (PCI) curves were measured with a PCT-Pro 2000 (SETARAM) equipped with MKS pressure transducer with an accuracy of 1.0%. The temperature of the sample was measured inside the sample holder well using a K-type thermocouple with an accuracy of ± 1.1 °C. High purity hydrogen was introduced step by step up to a maximum of 40 bar. Sample volume correction was taken into account when calculating the amount of hydrogen uptake. The sample was previously activated by two absorption/desorption cycles carried out at 30 bar H_2 pressure at 350 °C and under dynamic vacuum up to 375 °C, respectively.

4. RESULTS AND DISCUSSION

4.1 On the Mg-Ti-Nb-Cr-Mn-Ni system

4.1.1 Alloys selection

As indicated in the methodology, the φ parameter calculation for the 60 A_2B-type Mg containing alloys with six elements was performed and allowed to rank the alloy systems as a function of this thermodynamic parameter. In Appendix II, the results of the eleven best-ranked alloy systems are exhibited. Among the alloys that have Mg in their composition, the three best-ranked alloy systems were selected. Table 1 exhibits the results for the selected systems.

Table 1: Calculated values of the parameters for the three best-ranked A_2B-type alloy systems containing Mg.

Alloy	φ	δ (%)	Mean radius (Å)
$Mg_{22}Ti_{22}Nb_{22}Mn_{11}Fe_{11}Ni_{11}$	6.61	9.10	1.39
$Mg_{22}Ti_{22}Nb_{22}Mn_{11}Co_{11}Ni_{11}$	6.30	8.95	1.39
$Mg_{22}Ti_{22}Nb_{22}Cr_{11}Mn_{11}Ni_{11}$	6.15	8.57	1.43

Since the initial idea was to study all the selected systems, the system represented by the $Mg_{22}Ti_{22}Nb_{22}Cr_{11}Mn_{11}Ni_{11}$ composition was selected to start the investigations. After selecting the system and the equiatomic composition, two more compositions were chosen within this alloy system. One of these compositions was the one with the maximized φ parameter, to evaluate the effect of this parameter in obtaining single-phase solid solutions. The other one was the composition for which the δ parameter was maximized, in order to evaluate the influence of this parameter in phase formation and the alloy's hydrogen storage properties. In all the cases, the alloys might have a mean atomic radius of around 1.3 Å.

The φ, δ, and mean atomic radius parameters were calculated varying the atomic fractions of the elements A in the system whereas the atomic fractions of the elements B were fixed, within the set of compositions $(Mg_xTi_yNb_z)_2(Cr_{0.33}Mn_{0.33}Ni_{0.33})$. The results of these calculations are exhibited in Figure 6.

After determining the region of interest by the intersection of the optimization areas of each parameter, the compositions that presented the maximized value of φ and δ, respectively, were chosen. The compositions obtained in this first calculation step are indicated by the marks in yellow and blue in Figure 6d, respectively. For the condition of maximized φ, the resulting composition is $(Mg_{0.21}Ti_{0.27}Nb_{0.53})_2(Cr_{0.33}Mn_{0.33}Ni_{0.33})$, whereas for the condition of maximized δ, the resulting composition is $(Mg_{0.44}Ti_{0.21}Nb_{0.35})_2(Cr_{0.33}Mn_{0.33}Ni_{0.33})$.

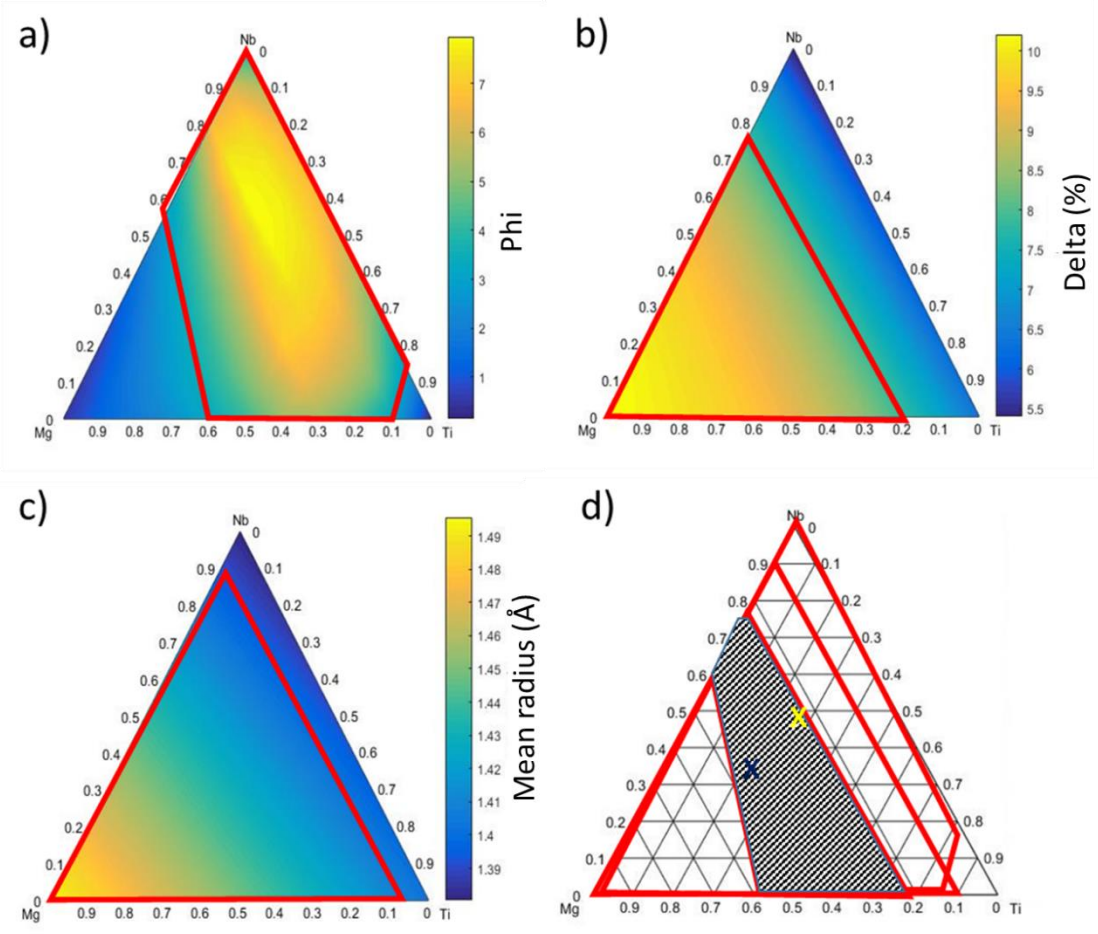

Figure 6: Calculated parameters varying only the elements A in the set of compositions *$(Mg_xTi_yNb_z)_2(Cr_{0.33}Mn_{0.33}Ni_{0.33})$* and selection of the compositions within the region of interest. (a) *φ* parameter (b) delta parameter (c) mean radius (d) final region of interest obtained from the simultaneous optimization of the parameters and selection of the compositions. The yellow mark refers to the composition with the maximized *φ,* and the blue mark refers to the composition with the maximized delta.

After setting the values of A, a new calculation was performed varying elements B for the two conditions separately. The results are exhibited in Figure 7 and Figure 8.

The final composition was determined using the region of interest for the set of compositions with maximized φ, as indicated by the yellow mark in Figure 7d. For this process of selection, the compositional definition of high entropy alloys was taken into account so that in the final composition all the elements have an atomic fraction between 5 %at. ≤ x ≤ 35 %at. Thus, the selected alloy is $(Mg_{0.21}Ti_{0.27}Nb_{0.53})_2(Cr_{0.15}Mn_{0.54}Ni_{0.31})$, whose chemical composition represented by the normalized atomic fraction of the elements and as integer numbers instead of decimals is $Mg_{14}Ti_{18}Nb_{35}Cr_5Mn_{18}Ni_{10}$ and henceforth was called "**high phi**."

Similarly, after defining the region of interest for the set of alloys with the δ parameter maximized, the final composition was determined, as illustrated by the blue mark in Figure 8d. The selected alloy is $(Mg_{0.44}Ti_{0.21}Nb_{0.35})_2(Cr_{0.45}Mn_{0.15}Ni_{0.40})$, whose chemical composition represented by the normalized atomic fraction of the elements and as integer numbers instead of decimals is $Mg_{30}Ti_{14}Nb_{23}Cr_{15}Mn_5Ni_{13}$, designated as "**high delta**."

Besides the two compositions aforementioned, the alloy with equiatomic fractions of elements A and elements B was chosen. The chemical composition of this alloy represented the normalized atomic fraction of the elements and as integer numbers instead of decimals is $Mg_{22}Ti_{22}Nb_{22}Cr_{11}Mn_{11}Ni_{11}$ and this alloy was identified as "**equiatomic**."

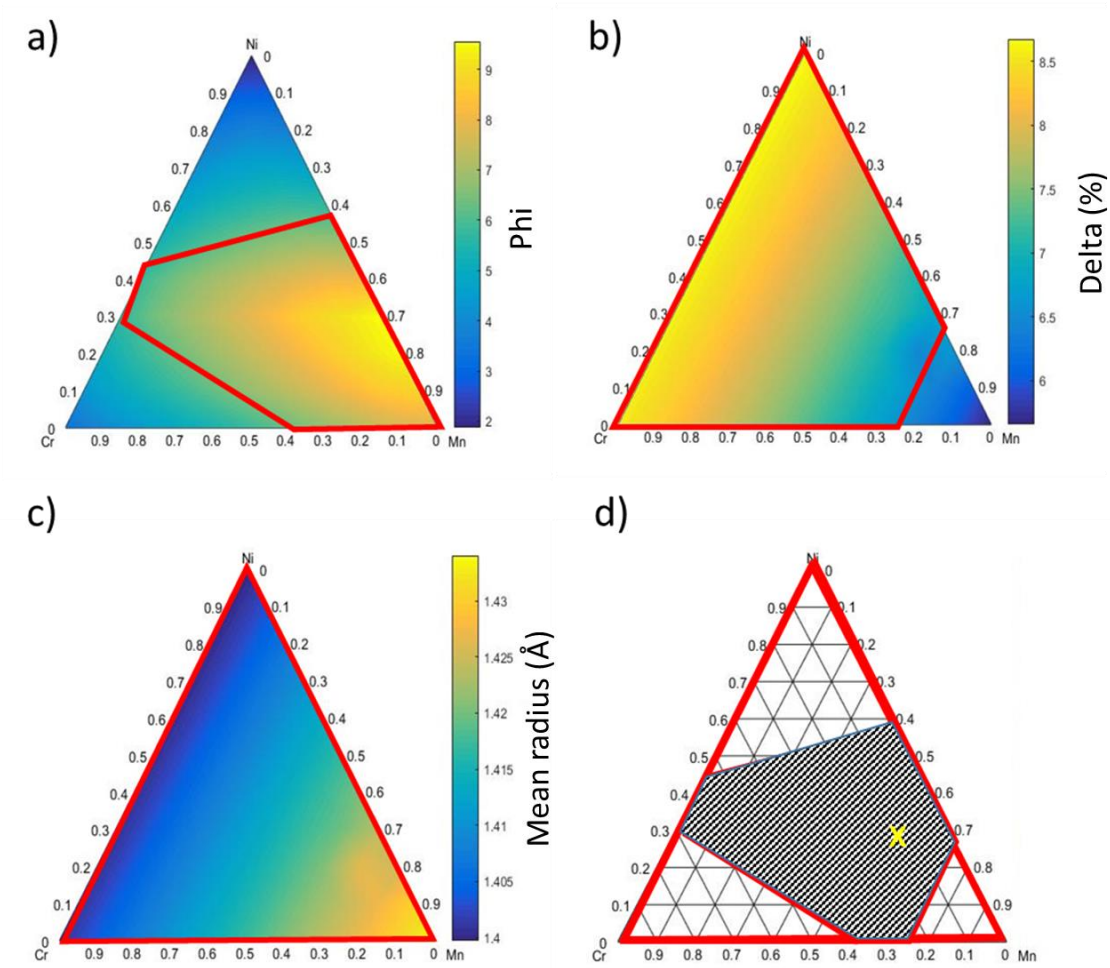

Figure 7: Calculated parameters varying only the elements B in the set of compositions $(Mg_{0.21}Ti_{0.27}Nb_{0.53})_2(Cr_uMn_vNi_w)$ and selection of the final composition within the region of interest. (a) φ parameter (b) delta parameter (c) mean radius (d) final region of interest obtained from the simultaneous optimization of the parameters considering the maximization of φ and selection of the composition. The yellow mark indicates the chosen composition.

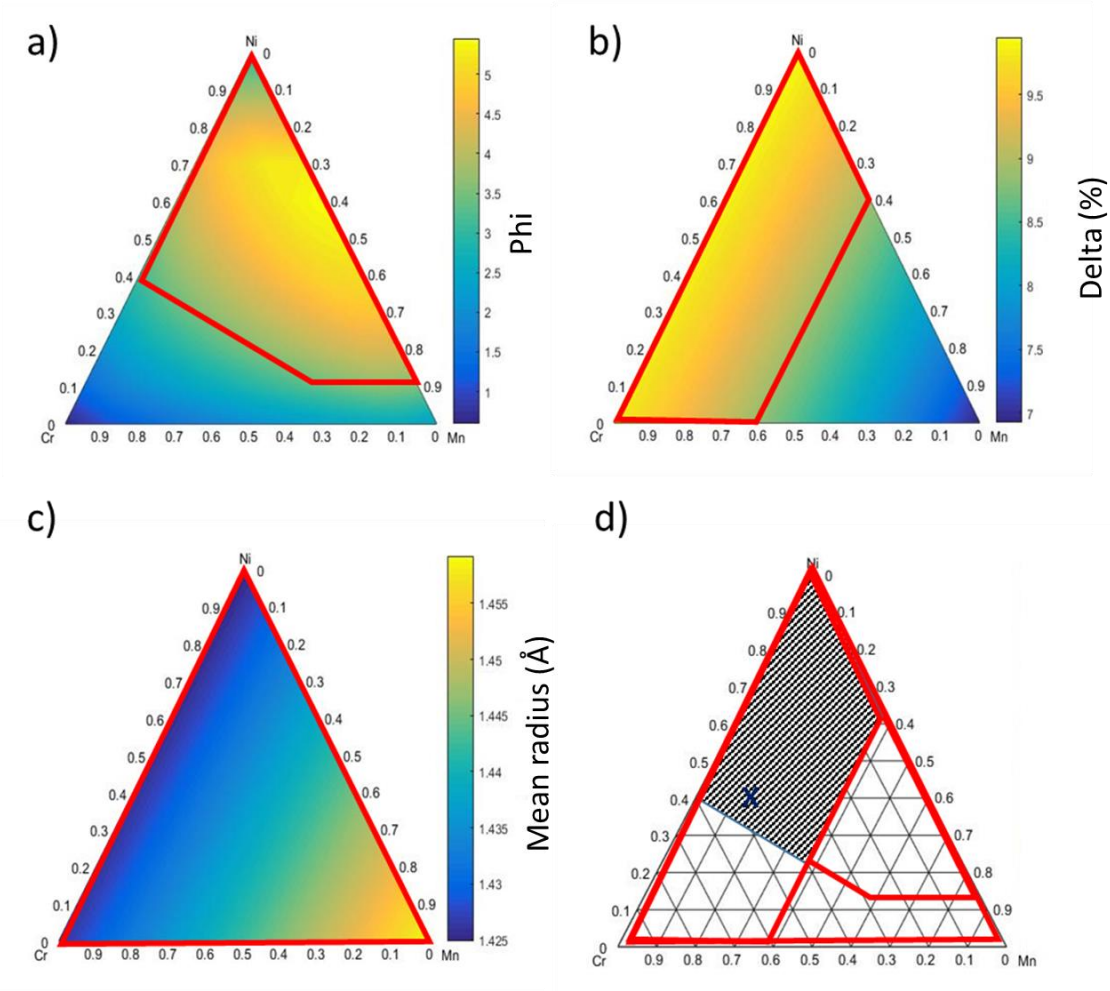

Figure 8: Calculated parameters varying only the elements B in the set of compositions $(Mg_{0,44}Ti_{0,21}Nb_{0,35})_2$(CruMnvNiw) and selection of the final composition within the region of interest. (a) φ parameter (b) delta parameter (c) mean radius (d) final region of interest obtained from the simultaneous optimization of the parameters and selection of the compositions.The blue mark indicates the chosen composition.

Table 2 summarizes the results of the calculations and the values of the parameters for every alloy along with their respective composition in normalized atomic fraction.

Table 2: Compositions of the selected alloys and calculated values for all parameters.

Alloy	Identification	φ	δ (%)	Mean radius (Å)
$Mg_{14}Ti_{18}Nb_{35}Cr_5Mn_{18}Ni_{10}$	High phi	9.07	7.19	1.42
$Mg_{30}Ti_{14}Nb_{23}Cr_{15}Mn_5Ni_{13}$	High delta	5.04	9.54	1.43
$Mg_{22}Ti_{22}Nb_{22}Cr_{11}Mn_{11}Ni_{11}$	Equiatomic	6.15	8.57	1.43

4.1.2 Structural characterization of mechanically alloyed samples

The alloys were synthesized via MA (HEBM under 0.7 MPa of argon) and heat-treated at 350 °C for 12 hours. The quantification of the elements present in the heat-treated samples was performed by SEM-EDX. In a region of the sample visible under the microscope, five areas were selected in which the elements were quantified, as represented in Figure 9. The average of the values obtained for each element in the different areas was calculated and this average value was considered representative of the general composition of the alloys. In Table 3, these calculated mean values are shown for each of the alloys, together with the new representation indicating the composition in atomic fraction obtained by EDX. From the table, it can be seen that the compositions obtained after processing by MA diverged from those established by the initial theoretical calculations. Frequently, the composition of the powder products of HEBM is similar to the proportion of starting elements [30]. In the present work, however, we suggest that the broad distribution of the alloy's particle sizes and the existence of compositional gradient between particles might have misled the microchemical analysis by EDX (will be shown later in the SEM-EDX results). Moreover, cold welding could not be entirely prevented, and some amount of material was lost as it was stuck in the milling vial. Table 4 shows the recalculated parameter values based on the composition of the alloys obtained by EDX.

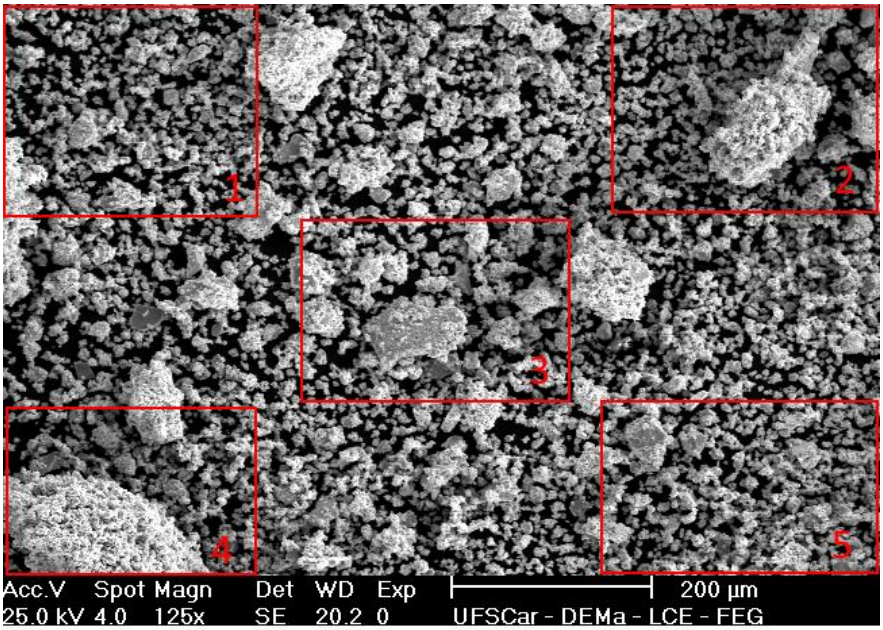

Figure 9: Indicated areas in which EDX analysis was performed for quantification of the alloy's composition.

Table 3: Average composition obtained from EDX measurements.

Alloy	Mg at. (%)	Ti at. (%)	Nb at. (%)	Cr at. (%)	Mn at. (%)	Ni at. (%)
$Mg_{14}Ti_{18}Nb_{35}Cr_5Mn_{18}Ni_{10}$ (high phi)	16	14	37	5	19	9
$Mg_{30}Ti_{14}Nb_{23}Cr_{15}Mn_5Ni_{13}$ (high delta)	39	13	21	12	5	10
$Mg_{22}Ti_{22}Nb_{22}Cr_{11}Mn_{11}Ni_{11}$ (equiatomic)	30	15	23	10	11	11

Table 4: Results of the recalculation of the parameters based on the composition obtained in EDX measurements.

EDX composition	Identification	φ	δ (%)	Mean radius (Å)
$Mg_{16}Ti_{14}Nb_{37}Cr_5Mn_{19}Ni_9$	High phi	8.10	7.10	1.42
$Mg_{39}Ti_{13}Nb_{21}Cr_{12}Mn_5Ni_{10}$	High delta	2.51	9.25	1.46
$Mg_{30}Ti_{15}Nb_{23}Cr_{10}Mn_{11}Ni_{11}$	Equiatomic	4.35	8.94	1.44

The recalculation of the parameters indicated that the magnitudes of them were modified, mainly for the φ parameter, due to the modification in the composition. However, these new compositions and recalculated values were still useful for the purpose of this section to evaluate the alloy selection method since the main characteristics of each alloy was maintained, i.e., the high phi alloy presented the highest φ value and close to the previous one, and similarly for the high delta e equiatomic alloys.

The as milled samples of the alloys produced by MA were characterized by XRD. The phases present in each alloy were identified, and the lattice parameter of the solid solution was obtained by the Pawley Fit method. In the application of this method, the scale factor, background, and lattice parameters were refined. Phase fraction was not refined because the overlapping of peaks at low angles was intense and no phase model could be created for the solid solution since its composition was unknown. Figure 10 shows the result of the three alloys. It can be seen that for all compositions there was the formation of a body-centered cubic (BCC) solid solution, with a lattice parameter of 3.2538(6) Å for the high phi alloy, 3.2861(8) Å for the high delta alloy, and 3.2883(9) Å for the equiatomic alloy. In addition, the presence of free Mg was identified in the equiatomic and high delta alloys, in addition to free Mn and Cr in all compositions.

Following the characterization step, the samples of the three compositions were subjected to heat treatment at a temperature of 350°C for 12 hours in order to evaluate the thermal stability of the obtained phases. This evaluation is of

fundamental importance since in volumetric experiments the material is subjected to temperature cycles over time.

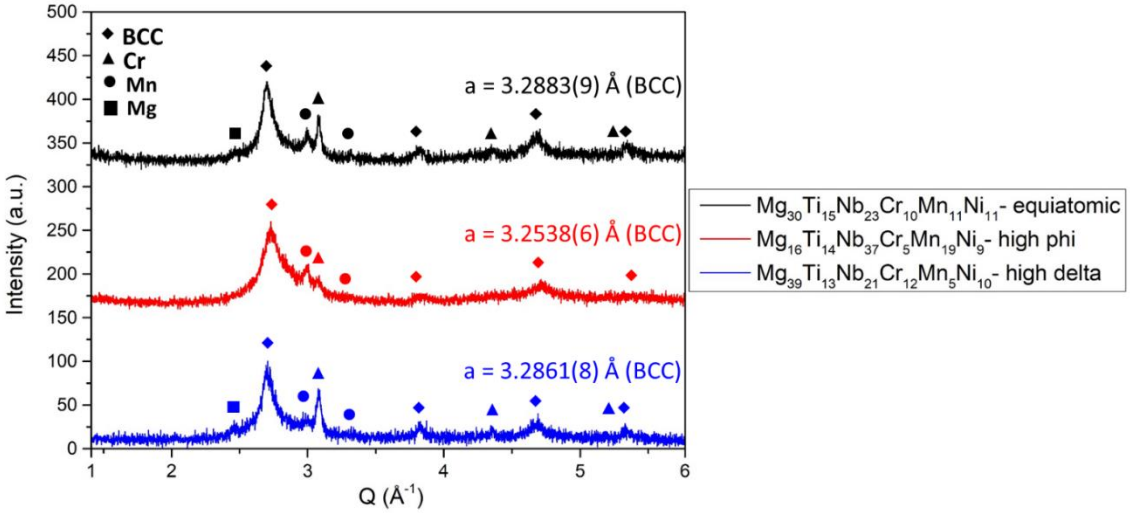

Figure 10: XRD patterns of the three alloys in the as milled condition. XRD measured with a Cu source (λ=1.5406 Å). The lattice parameters were obtained by Pawley Fit.

Figure 11 exhibits that there has been an improvement in the definition of the diffraction pattern for the heat-treated high delta alloy, mainly due to a narrowing of the diffraction peaks. This narrowing is related to an increase in crystallite size and a decrease in microstrain due to heat treatment. Another observed modification was a relative increase in the Mg and Cr peaks from the as milled alloy to the heat-treated one. These phenomena can also be related to an increase in the crystallite size of these phases and a decrease in the overlapping of the peaks, especially for peaks from Mg, that was overlapped by the BCC phase peaks around Q= 2.5 $Å^{-1}$.

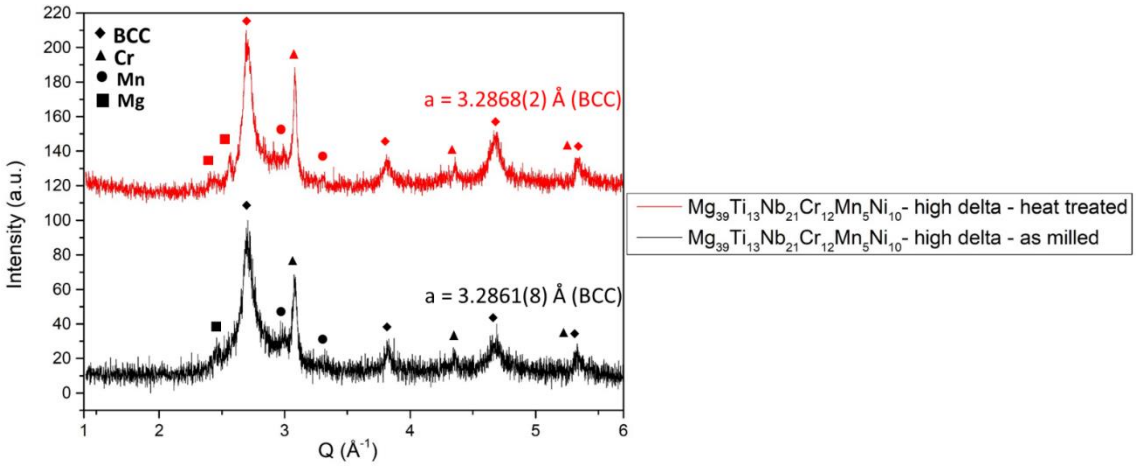

Figure 11: XRD pattern of the "**high delta**" alloy in the as milled and heat-treated conditions. XRD measured with a Cu source (λ=1.5406 Å). The lattice parameters were obtained by Pawley Fit.

Figure 12 shows the result for the high phi alloy. There was a small increase in the lattice parameter of the BCC structure and the relative maintenance of the Cr peaks intensity. Furthermore, there was no segregation of Mg after the heat treatment, indicating that this element remained in solid solution throughout the heat treatment.

The results for the equiatomic alloy are shown in Figure 13. In this figure, it is possible to notice a decrease in the lattice parameter of the BCC structure, a more evident relative increase in the intensity of the Mg peaks and a small relative increase in the intensity for the Mn and Cr peaks. These modifications can also be related to the influence of temperature on the crystallite size and microstrain of the sample synthesized by ball milling. Due to the narrowing of the diffraction peaks, especially for the peaks from the BCC phase, the fit of the lattice parameter could be adjusted and probably this is the main reason for the modification of the value of this parameter aforementioned.

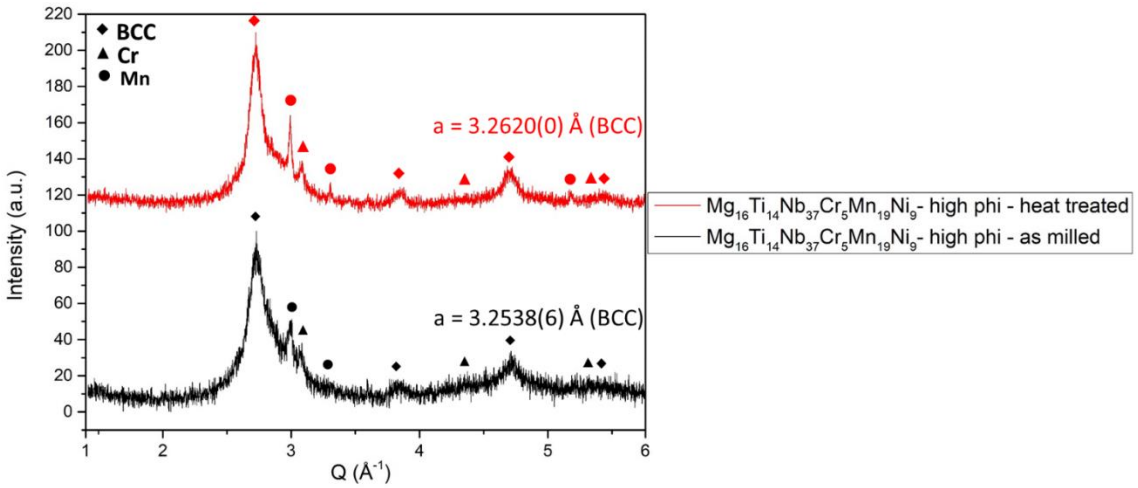

Figure 12: XRD pattern of the "**high phi**" alloy in the as milled and heat treated conditions. XRD measured with a Cu source (λ=1.5406 Å). The lattice parameters were obtained by Pawley Fit.

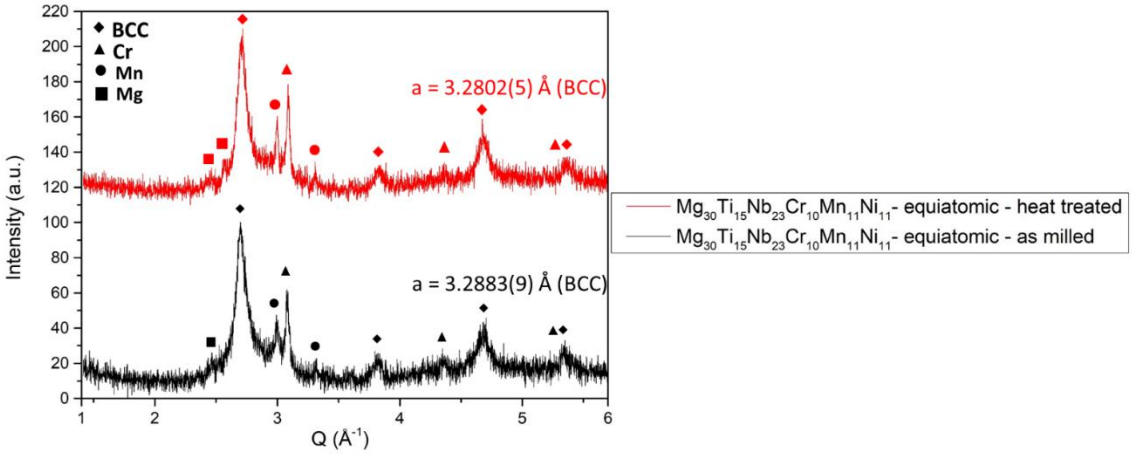

Figure 13: XRD pattern of the "**equiatomic**" alloy in the as milled and heat-treated conditions. XRD measured with a Cu source (λ=1.5406 Å). The lattice parameters were obtained by Pawley Fit.

The XRD results for the heat-treated samples indicate that for all compositions the main changes were due to the narrowing of the diffraction peaks and no important modification in the structure of the materials occurred. These results might indicate that the solid solutions of these alloys are stable at 350 ºC.

The morphology of the microstructure of the synthesized alloys was evaluated by means of SEM images in SE (Scattered Electrons) mode. In addition, an initial view of the chemical distribution could be obtained by means

of SEM images in BSE (Backscattered Electrons) mode. Figure 14a shows the SEM image in SE mode for the high delta alloy. It can be seen that the milled product consisted of rounded and other plate-shaped particles with a heterogeneous size distribution. In Figure 14b, the BSE-mode image indicates that a phase with good element distribution was formed during processing, although the presence of regions with different shades of grey indicates elements that did not mix or were segregated during the formation of the major phase. A more detailed analysis of the chemical distribution of the elements was performed by means of EDX mapping. In Figure 14d-i the results for the high delta alloy are shown. By evaluating these images it is possible to observe a good distribution of the elements, which may indicate the presence of a solid solution formed by the mixture of all elements. In addition, it is also possible to identify regions richer in Mn, others in Cr and still others in Mg, which indicate segregation of these chemical species in these regions.

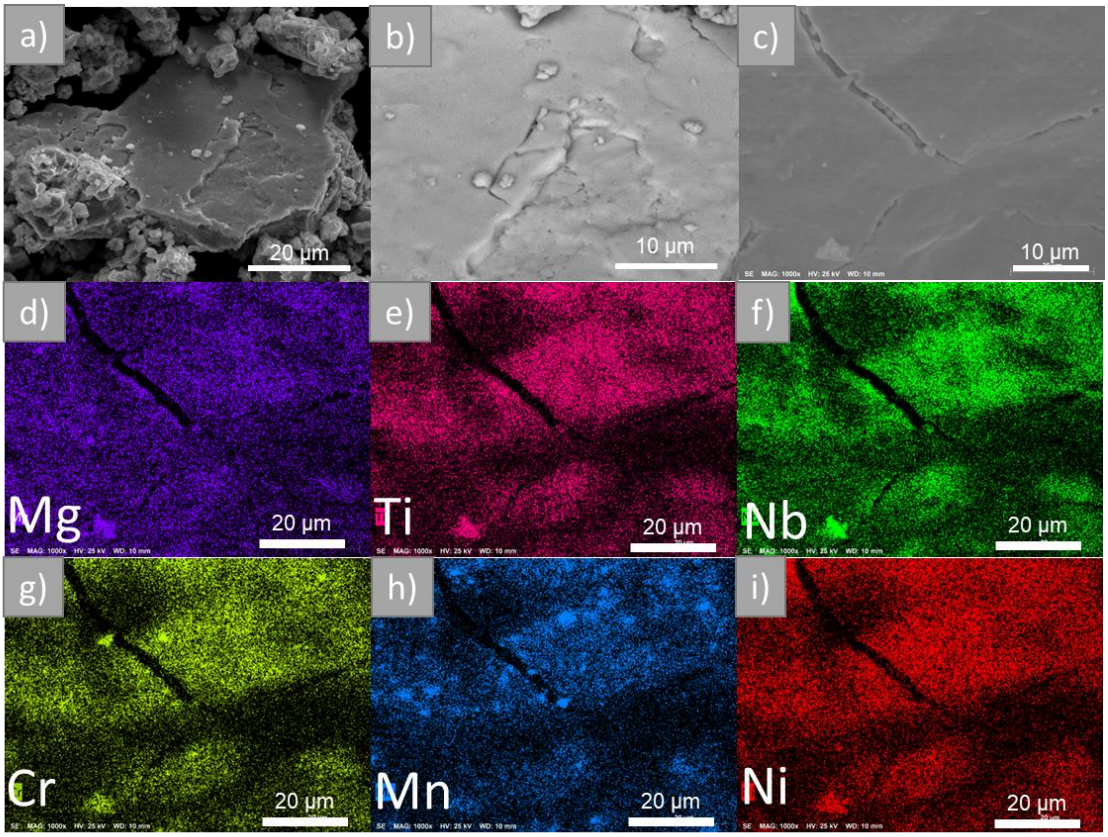

Figure 14: SEM images and EDX mapping of the "**high delta"** alloy, in which a) SEM-SE, b) SEM-BSE, c) SE-EDX, d) - i) EDX mapping.

Figure 15 shows the SEM images for the high phi alloy. Similar to the high delta alloy, the morphology of this alloy consisted of rounded and plate-shaped particles with a heterogeneous size distribution. From the image in BSE mode, it is possible to observe a good chemical distribution of the elements, with an absence of the evident segregation of elements presented by the high delta alloy. The EDX mapping of the high phi alloy indicates that there was a homogeneous distribution of most of the elements indicating the formation of a solid solution, although there are few regions richer in Mn and Cr. Furthermore, it is possible to verify regions where the presence of Mg was scarce.

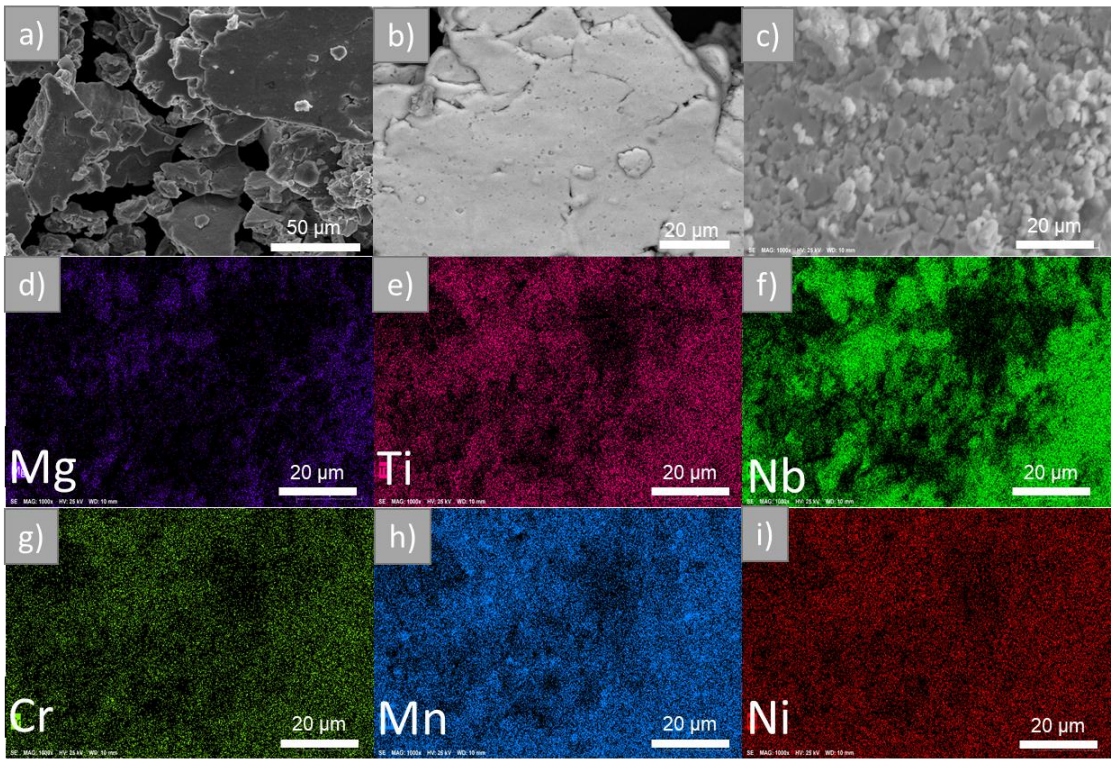

Figure 15: SEM images and EDX mapping of the "**high phi**" alloy, in which a) SEM-SE, b) SEM-BSE, c) SE-EDX, d) - i) EDX mapping.

Figure 16a shows the particle distribution resulting from the processing of the equiatomic alloy. Similar to other alloys, the morphology of this material also consisted of small round and plate-shaped particles of different sizes, although in this alloy the particles were more agglomerated. The image in BSE mode also

showed a good chemical distribution of the elements, with the presence of regions where there was segregation. The EDX mapping of this alloy also indicates a homogeneous distribution that seems to be a solid solution, together with the presence of regions rich in different elements. Mn, Cr, and Mg appear separately in clusters in several regions of the sample, as shown in Figure 16d-i.

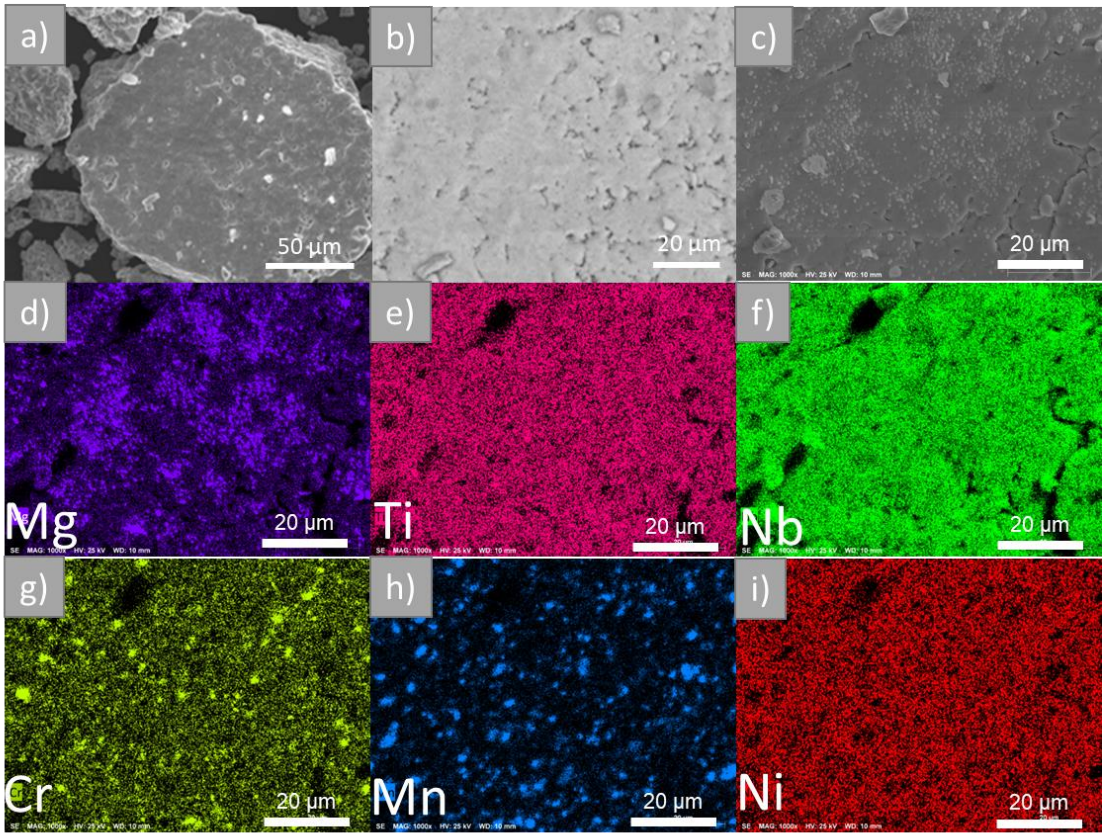

Figure 16: SEM images and EDX mapping of the "**equiatomic**" alloy, in which a) SEM-SE, b) SEM-BSE, c) SE-EDX, d) - i) EDX mapping

The initial results of XRD and SEM characterization suggested that the solid solution formed for all compositions is mostly composed of Ti, Nb, Ni, and Mg since these elements do not appear in the free form in XDR and EDX results. In the case of Mg, the detection of segregation occurs when this element is in excess of approximately 16% at. As more Mg is added, the greater the amount segregated, which indicates that this is more or less the solubility limit of this element in the solid solution. Regarding the elements Mn and Cr, the results indicated that these elements present low solubility in the solid solution, because

even when they are in amounts close to 5% at. they are detected in the free form. Yet, the solid solutions synthesized for all compositions are stable under the conditions of heat treatment applied, since no further segregation of elements or decomposition of the solid solution were observed.

4.1.3 Hydrogen storage behavior of mechanically alloyed samples

The hydrogen absorption kinetics was performed at 350 °C and around 60 bar of H_2 pressure. Before the kinetic curves were started, the alloys were subjected to thermal activation at 350 °C for 1.5 h with the vacuum pump activated. Figure 17 shows the results obtained for the three alloys. All compositions presented different results regarding the gravimetric capacity. The high phi alloy absorbed the lowest amount of hydrogen, approximately 0.3 wt.% of H_2, followed by the equiatomic alloy, with 1.18% wt.% of H_2 absorbed, approximately. The alloy that presented the highest absorption capacity was the high delta, around 1.45% wt.% of H_2.

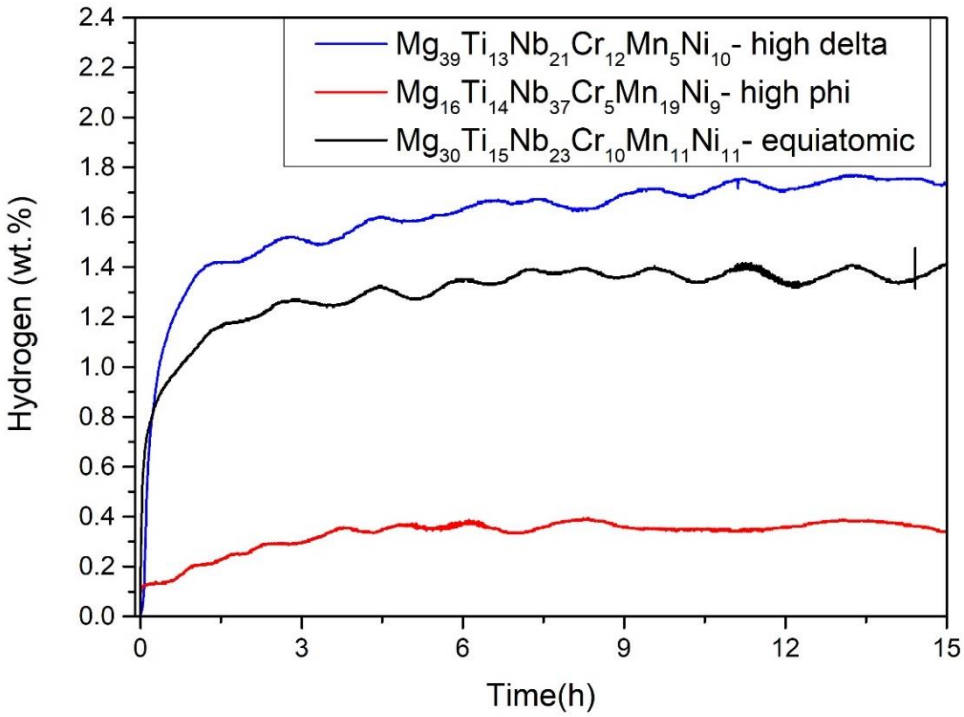

Figure 17: Hydrogen absorption kinetics for all the alloys at 350 °C and around 60 bar of H2.

The XRD of the samples after the absorption kinetics made it possible to evaluate the changes that occurred due to hydrogen entering the structure of the materials. Figure 18 shows the XRD patterns for the high delta alloy together with the identification of the phases present and the lattice parameter of the BCC solid solution. It is observed that for this alloy the hydrogen was absorbed into the BCC phase by means of solid solution, which resulted in an expansion of the crystalline structure of this phase. The lattice parameter increased from 3.2868(2) Å to 3.4301(8) Å after absorption, which means an increase of 13.66% in the volume of the unit cell. In addition, the formation of a new phase, identified as the Mg_2NiH_4 hydride, was observed.

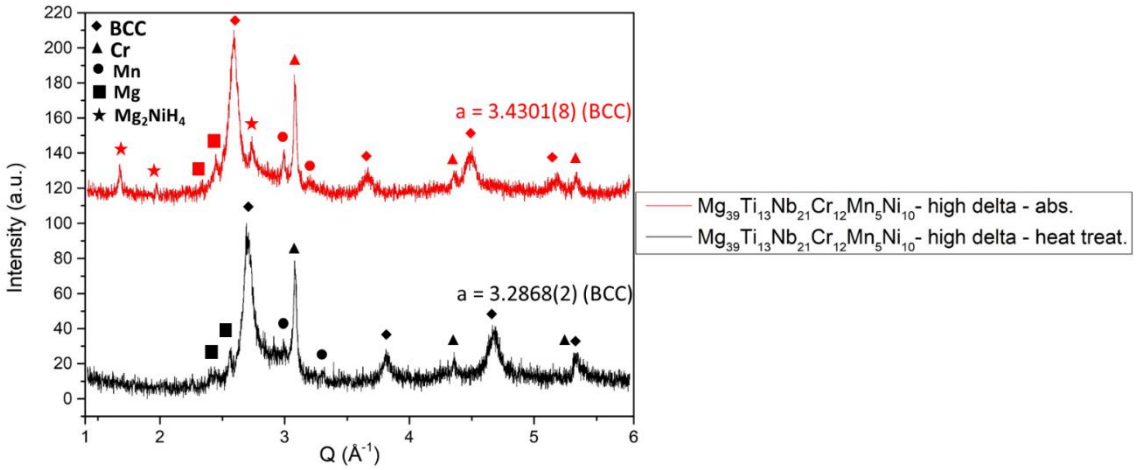

Figure 18: XRD pattern of high delta alloy in the heat-treated condition and after absorption kinetics. XRD measured with a Cu source (λ=1.5406 Å). The lattice parameters were obtained by Pawley Fit.

The high phi alloy also absorbed hydrogen by solid solution through the BCC phase, as shown in Figure 19. The expansion of the lattice by hydrogen input resulted in an increase of the lattice parameter from 3.2620(0) Å to 3.4310(0) Å, which accounts for a unit cell volume expansion of 16.36%. Unlike the high delta alloy, the high phi did not present Mg_2NiH_4 formation after the absorption kinetics.

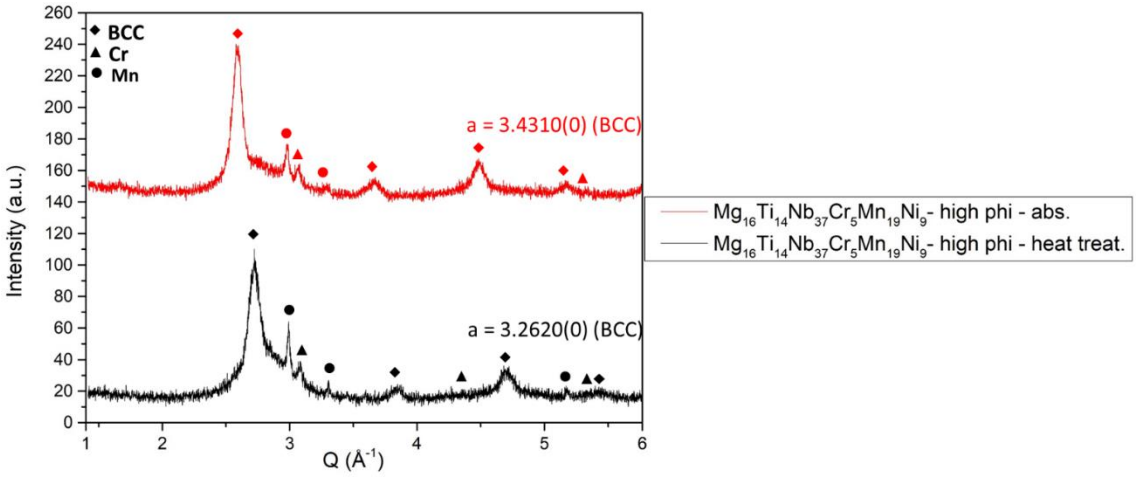

Figure 19: XRD pattern of high phi alloy in the heat-treated condition and after absorption kinetics. XRD measured with a Cu source (λ=1.5406 Å). The lattice parameters were obtained by Pawley Fit.

Figure 20 shows the XRD results for the equiatomic alloy. Like the high delta alloy, the equiatomic alloy absorbed hydrogen by solid solution through the BCC phase and by the formation of Mg_2NiH_4 hydride. Structural expansion by hydrogen input in the BCC phase resulted in an increase of the lattice parameter from 3.2802(5) Å to 3.4366(4) Å, which accounts for a 14.99% expansion in unit cell volume.

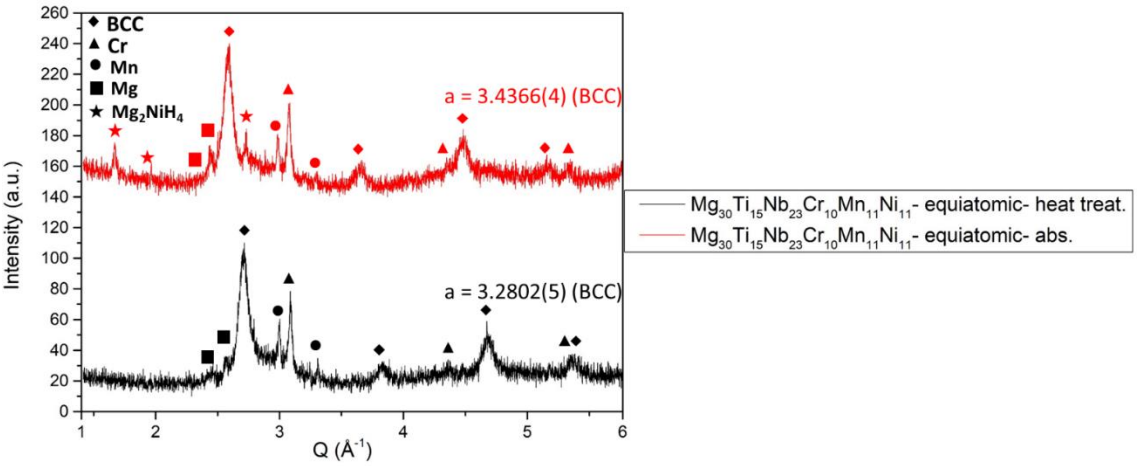

Figure 20: XRD pattern of equiatomic alloy in the heat-treated condition and after absorption kinetics. XRD measured with a Cu source (λ=1.5406 Å). The lattice parameters were obtained by Pawley Fit.

These results indicate that all alloys absorbed hydrogen by solid solution through the BCC phase. However, the high phi alloy showed greater structural

expansion followed by the equiatomic and high delta alloys, which may indicate that the amount of hydrogen absorbed by the BCC phase of each alloy was slightly different. It can be implied that the greater the structural expansion, the higher the amount of hydrogen stored by the solid solution of each alloy, since all solid solutions have BCC structure and hydrogen is responsible for the volume expansion. Moreover, in alloys with free Mg after heat treatment, the Mg_2NiH_4 hydride was formed during kinetics. This hydride was responsible for considerably increasing the maximum amount absorbed for the high delta and equiatomic alloys, as it has a gravimetric capacity of 3.3 wt. % of H_2 [6].

After absorption, the different compositions were submitted to a desorption experiment. In this experiment, the temperature of the sample holder was raised from room temperature to 450°C, while a free volume inside a gas reservoir in the Sievert-type apparatus was provided to allow the evolution of gases along with the heating. The crystallographic phases present in the materials after desorption were identified by XRD and the lattice parameters of the BCC phase were refined by Rietveld.

Figure 21 shows the results of the high delta alloy desorption. It is possible to notice that the alloy returned to a phase distribution similar to the one it presented before the absorption experiment. The lattice parameter decreased from 3.4301(8) Å to 3.3458(1) Å, which results in a unit cell volume contraction of 7.19%. The contraction of the crystal structure with the hydrogen output did not occur in the same magnitude in which the expansion had occurred, indicating the occurrence of a permanent increase of the crystal structure of the BCC phase after the absorption and desorption kinetics.

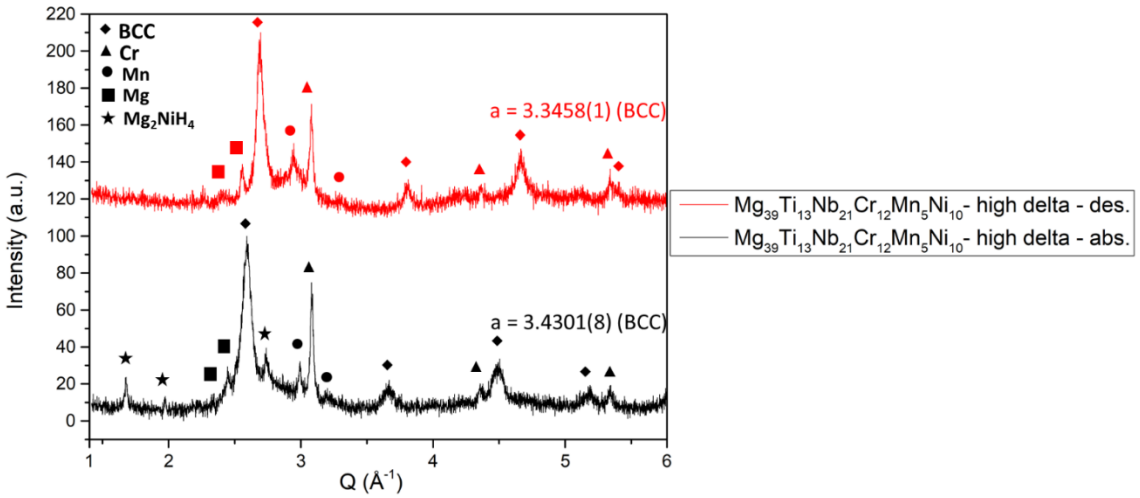

Figure 21: XRD pattern of high delta alloy after absorption kinetics and after desorption kinetics. XRD measured with a Cu source (λ=1.5406 Å). The lattice parameters were obtained by Pawley Fit.

Figure 22 exhibits the results for the high phi alloy. The phases present after desorption are similar to the ones found before absorption kinetics. The lattice parameter decreased from 3.4310(0) Å to 3.3313(0) Å, resulting in a unit cell volume contraction of 8.47%. This also indicates the presence of permanent expansion of the BCC phase crystal structure after absorption and desorption

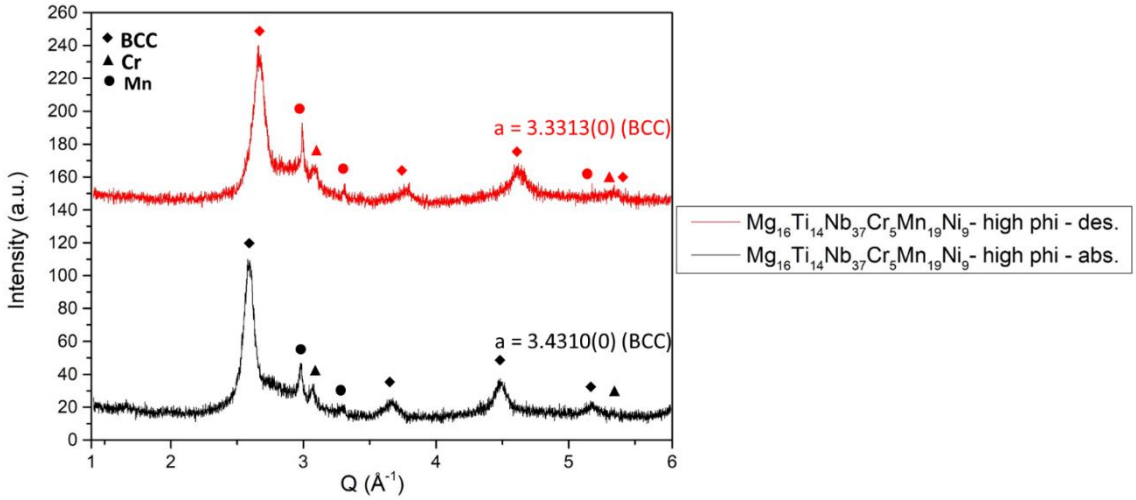

Figure 22: XRD pattern of high phi alloy after absorption kinetics and after desorption kinetics. XRD measured with a Cu source (λ=1.5406 Å). The lattice parameters were obtained by Pawley Fit.

The results for the equiatomic alloy are shown in Figure 23. If compared to the initial phases, there was no severe phase change after the

absorption/desorption cycle. The lattice parameter decreased from 3.4466(4) Å to 3.3139(5) Å, resulting in a unit cell volume contraction of 11.11%. For this alloy, there is also evidence of the presence of permanent expansion of the BCC phase crystal structure after absorption and desorption.

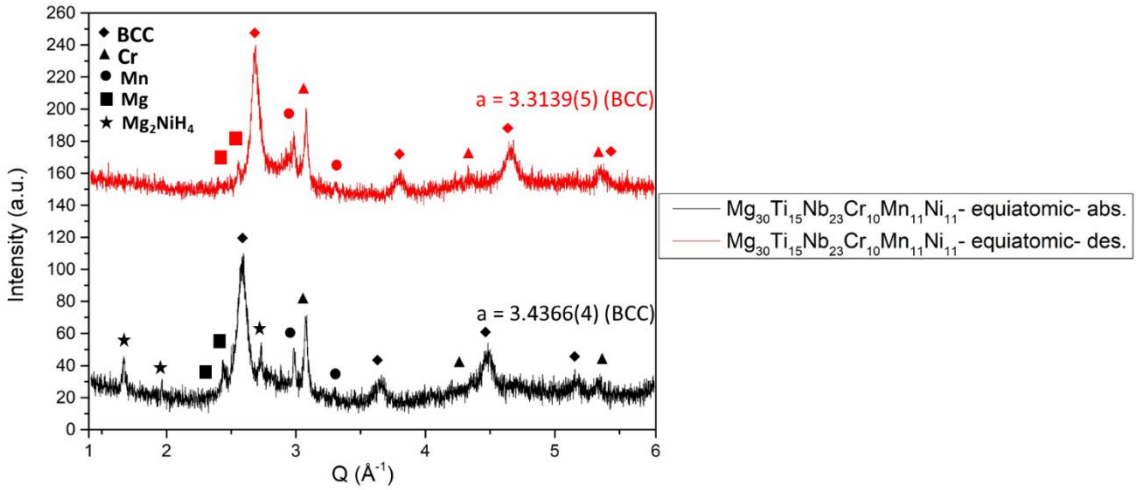

Figure 23: XRD pattern of equiatomic alloy after absorption kinetics and after desorption kinetics. XRD measured with a Cu source (λ=1.5406 Å). The lattice parameters were obtained by Pawley Fit.

The results of hydrogen desorption, with the presence of permanent expansion of the BCC phase for all alloys, suggested that just a fraction of the absorbed hydrogen was desorbed under the conditions applied during desorption. The alloy that presented the highest structural expansion was the high phi, but the equiatomic alloy presented the highest volume contraction, which might indicate that the solid solution of the high phi alloy absorbed the highest amount of hydrogen, whereas the equiatomic alloy desorbed the highest amount.

4.1.4 Considerations about the alloy selection method

Table 5 summarizes the results obtained for the evaluated alloy system.

Table 5: Summary of the results obtained for the alloy system evaluated

Calculated composition	EDX composition	Synthesized phases by MA	Capacity (wt.% H_2)	Phases after absorption	Phases after desorption
High phi $Mg_{14}Ti_{18}Nb_{35}Cr_5Mn_{18}Ni_{10}$	$Mg_{16}Ti_{14}Nb_{37}Cr_5Mn_{19}Ni_9$	BCC 3.2538 Å ↑Mn, Cr	0.3	BCC 3.4310 Å, ↑Mn, Cr	BCC 3.3313 Å, ↑Mn, Cr
High delta $Mg_{30}Ti_{14}Nb_{23}Cr_{15}Mn_5Ni_{13}$	$Mg_{39}Ti_{13}Nb_{21}Cr_{12}Mn_5Ni_{10}$	BCC 3.2861 Å Mg, Mn, ↑Cr	1.45	BCC 3.4301 Å, Mg_2NiH_4, Mg, Mn, ↑Cr	BCC 3.3458 Å, Mg, ↑Cr, Mn
Equiatomic $Mg_{22}Ti_{22}Nb_{22}Cr_{11}Mn_{11}Ni_{11}$	$Mg_{30}Ti_{15}Nb_{23}Cr_{10}Mn_{11}Ni_{11}$	BCC 3.2883 Å Mg, ↑Mn, ↑Cr	1.18	BCC 3.4366 Å, Mg_2NiH_4, Mg, ↑Mn, ↑Cr	BCC 3.3139 Å, Mg, ↑Cr, ↑Mn

All the compositions evaluated so far presented stable solid solutions along the segregation of metallic elements. No complex structure or intermetallic phases were obtained out of the mixture of the six elements used. According to [52] and [46], for values of $\varphi > 20$ and $\delta \cong 6.6\%$, a single-phase solid solution is expected to be obtained when the alloy is synthesized by the casting process. The results obtained so far in the present work might indicate that these boundaries values may be slightly lower in the case of HEBM process. The high phi alloy ($\varphi = 8.10$ and $\delta = 7.10$ %) was the one that presented so far the closest parameter values to the region of single-phase solid solutions and, accordingly, was the one with less presence of secondary phases (segregates) in the set of alloys evaluated. Yet, interestingly, even for a low value of φ and a high value of δ, as in the case of the high delta alloy ($\varphi = 2.51$ and $\delta = 9.25$ %), a solid solution was formed, even though it was not single-phase. It suggests that HEBM is a useful process for the mixing of elements when they are not likely to mix, which is supported by several publications [56].

The results also indicate that Mn, Cr, and Mg have low solubility in the solid solution and the difference in the parameters used for alloy selection leads to more or less segregation of these elements as a function of the composition. The presence of these segregated elements influenced the results of hydrogen storage sensibly.

Since all compositions presented similar mean atomic radius, the influence of this parameter could not be evaluated directly, although the fact that all solid solutions absorbed hydrogen may be related to, but not strictly, to the lattice parameter that they presented (which is related to the mean atomic radius), as it is in the case of classical BCC alloys [27]. The δ parameter couldn't be related directly to the hydrogen storage properties of the solid solutions. In the present work, the calculated values of this parameter represented not only the overall value for the alloys, due to the segregation of elements, but also influenced the amount of segregation, especially for Mg. The alloy that presented the highest δ (high delta) presented also the highest amount of Mg segregated since this element helped in the parameter maximization. Concurrently, the high delta absorbed the highest amount of hydrogen but also presented a significant

formation of the Mg_2NiH_4 hydride, which was responsible for most of the absorbed hydrogen. Thus, the increment in the gravimetric capacity came from the presence of Mg and Ni segregates, not from tailoring the solid solution properties by δ parameter maximization.

Even so, the alloy selection method used was valuable to guide the alloy design especially in terms of phase formation and stability. Regarding hydrogen storage, it was affected by the formation of segregates, that influenced the hydrogen storage properties of the alloys sensibly.

Since the process used for the alloy synthesis (HEBM) seemed to influence the phase formation and stability, in the following the focus of the present work was to evaluate the influence of mechanical alloying (MA) and reactive milling (RM) in the phase formation and hydrogen storage properties. The equiatomic composition was chosen to start this study since it presented a stable solid solution with promising hydrogen storage properties.

4.1.5 Mechanical alloying and reactive milling of $Mg_{22}Ti_{22}Nb_{22}Cr_{11}Mn_{11}Ni_{11}$ alloy

The results of the microchemical analysis by EDX for the $Mg_{22}Ti_{22}Nb_{22}Cr_{11}Mn_{11}Ni_{11}$ alloy synthesized by MA and RM are shown in Table 6. Given the theoretical composition, the results exhibit a quite good average composition obtained for both synthesis methods used. Nevertheless, it is worth mentioning that deviations from the nominal values were obtained mainly after MA, and especially for the elements Mg and Ti. The cause for these deviations might be the same as that mentioned in the study of the three compositions, that the broad particle sizes distribution and compositional gradient among the particles could mislead the EDX analysis alongside the occurrence of cold welding. (for further discussion about the EDX results see supplementary information in Appendix III from Fig. S1 to Fig. S9).

Table 6: Quantitative EDX analysis of the Mg22Ti22Nb22Cr11Mn11Ni11 alloy synthesized under 0.7 MPa of Ar (MA) and 3.0 MPa of H2 (RM).

Alloy	Mg at. (%)	Ti at. (%)	Nb at. (%)	Cr at. (%)	Mn at. (%)	Ni at. (%)
$Mg_{22}Ti_{22}Nb_{22}Cr_{11}Mn_{11}Ni_{11}$ MA	30.15	15.14	23.13	10.17	11.72	10.68
$Mg_{22}Ti_{22}Nb_{22}Cr_{11}Mn_{11}Ni_{11}$ RM	24.89	16.46	25.91	11.36	11.53	9.85
$Mg_{22}Ti_{22}Nb_{22}Cr_{11}Mn_{11}Ni_{11}$ Nominal	22.22	22.22	22.22	11.11	11.11	11.11

Figure 24 exhibits the powder XRD patterns for $Mg_{22}Ti_{22}Nb_{22}Cr_{11}Mn_{11}Ni_{11}$ alloy synthesized by MA, MA followed by heat treatment (named as MA HT) and RM. The MA and MA HT samples used for this XRD came from the same sample batch as used for the XRD measurements showed previously. However, the actual results were obtained by using a KαMo source, which is more energetic than a KαCu source and allows obtaining XRD patterns with more resolution.

The alloy synthesized by MA crystallizes into a BCC structure (W-type, $Im\bar{3}m$) with a lattice parameter of a = 3.2893(9) Å. Segregates of elemental Mg, Cr, and Mn were also identified. After HT, the BCC structure is stable, although the amount of elemental Mg, Cr, and Mn has increased, given the increment in the peak intensity related to these elements in the XRD pattern. Also, the lattice parameter of the BCC phase decreased to a = 3.2887(9) Å. These results can be related to the crystallite size and microstrain, as stated before, or even might suggest that some segregation of elements from a BCC disordered solid solution took place. Mg segregation could be responsible for the lattice parameter shrinkage considering that the atomic radius of Mg (1.50 Å) is considerably larger when compared to Ti (1.40 Å), Nb (1.45 Å), Cr (1.40 Å), Mn (1.40 Å), and Ni (1.35 Å) [57].

The alloy synthesized by RM presents a FCC hydride phase (MH_2 with CaF_2-type structure) with a fraction of elemental chromium and the Mg_2NiH_4 complex hydride. The lattice parameter of the FCC phase, according to the Pawley Fit, is a = 4.5001(4) Å. Direct synthesis of the hydride by RM is a promising process and has been reported for a few HEA [12] and multi-principal

element systems [50]. Interestingly, although Cr is still segregated in the RM sample, Mn seems to be part of the FCC hydride, which might indicate that the solubility of Mn in the FCC hydride is higher than in the BCC solid solution.

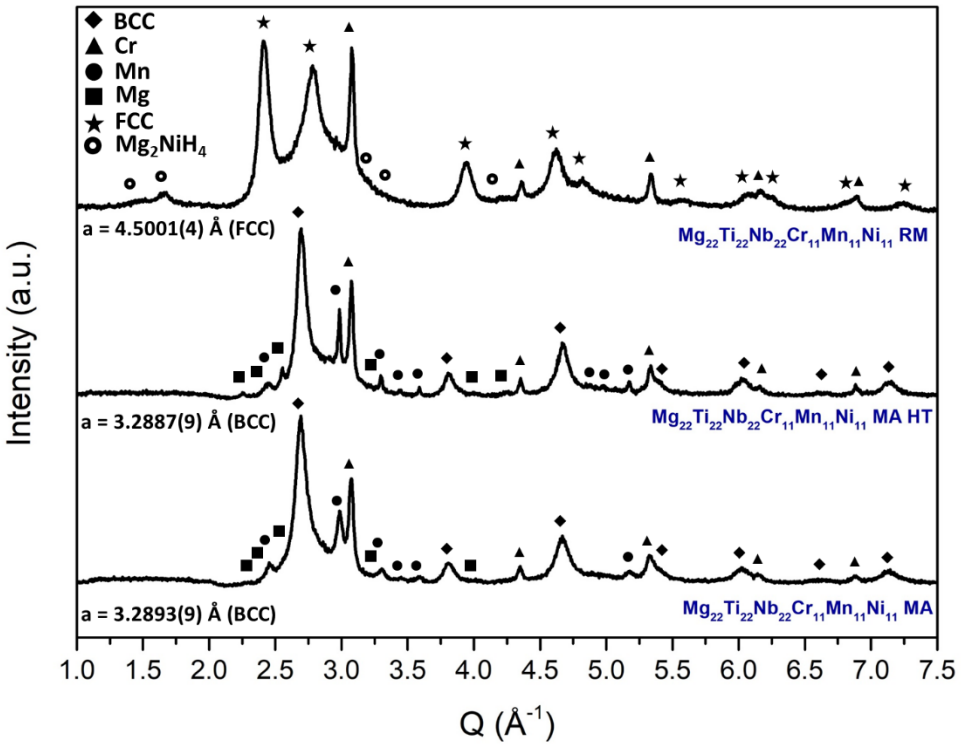

Figure 24: XRD patterns of the $Mg_{22}Ti_{22}Nb_{22}Cr_{11}Mn_{11}Ni_{11}$ alloy synthesized by MA, MA followed by heat treatment (HT - at 350 °C for 12 h), and RM. XRD measured with a Mo source (λ=0.70930 Å). The lattice parameters were obtained by Pawley Fit.

The SEM images and EDX elemental mapping for the $Mg_{22}Ti_{22}Nb_{22}Cr_{11}Mn_{11}Ni_{11}$ MA alloy after HT is shown again in Figure 25a for comparison. The microstructure characterization by SEM and EDX of the $Mg_{22}Ti_{22}Nb_{22}Cr_{11}Mn_{11}Ni_{11}$ RM alloy is shown in Figure 25b. In comparison to the MA alloy, the particle sizes of the RM one are smaller with a narrower distribution, probably due to embrittlement caused by hydrogen during milling. The BSE image of a single particle exhibits a homogeneous chemical composition (Figure 25b-II). The EDX mapping shows a main multicomponent solid solution phase with a proper distribution of the elements (Figure 25b – IV-IX). These results confirm that hydrogen promotes the solubility of these elements in the solid solution.

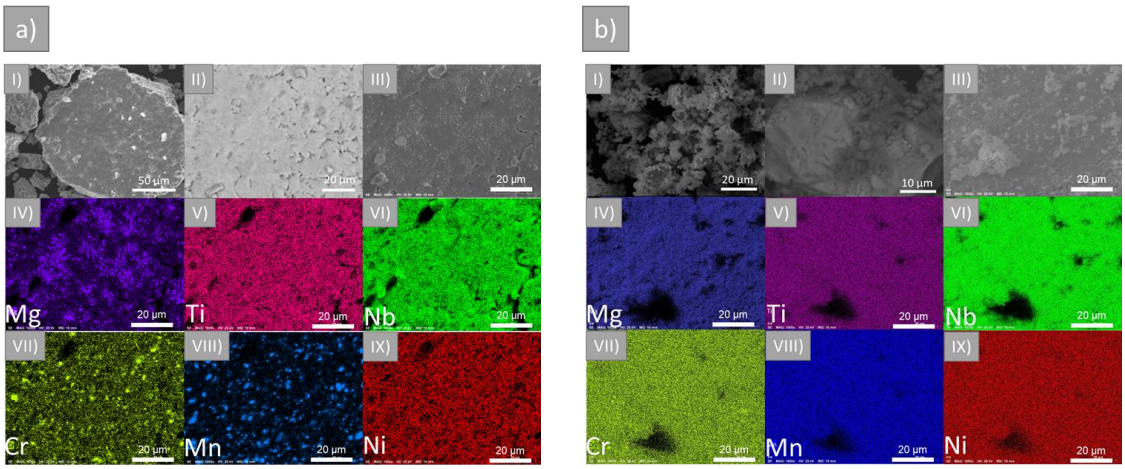

Figure 25: Comparative SEM images and EDX mapping of a) $Mg_{22}Ti_{22}Nb_{22}Cr_{11}Mn_{11}Ni_{11}$MA HT, in which I) SEM-SE, II) SEM-BSE, III) SE-EDX, IV) - IX) EDX mapping; and b) $Mg_{22}Ti_{22}Nb_{22}Cr_{11}Mn_{11}Ni_{11}$ RM, in which I) SEM-SE, II) SEM-BSE, III) SE-EDX, IV-IX) EDX mapping.

In further analysis with higher resolution by TEM, it could be observed for the MA sample of the $Mg_{22}Ti_{22}Nb_{22}Cr_{11}Mn_{11}Ni_{11}$ alloy crystallites with size <50 nm (Figure 26a and Figure 26b) displaying the same structure (Figure 26c) and a similar distribution of elements (Figure 26d-3j) as seen by XRD and SEM, respectively. For the RM sample, in the nanometer scale, crystallites with size ≤20 nm (Figure 27a and Figure 27b) displays the same FCC structure (Figure 27c), and distribution of elements (Figure 27d-4j), although in the TEM results the segregation of Cr is evident, which is in agreement with the XRD pattern.

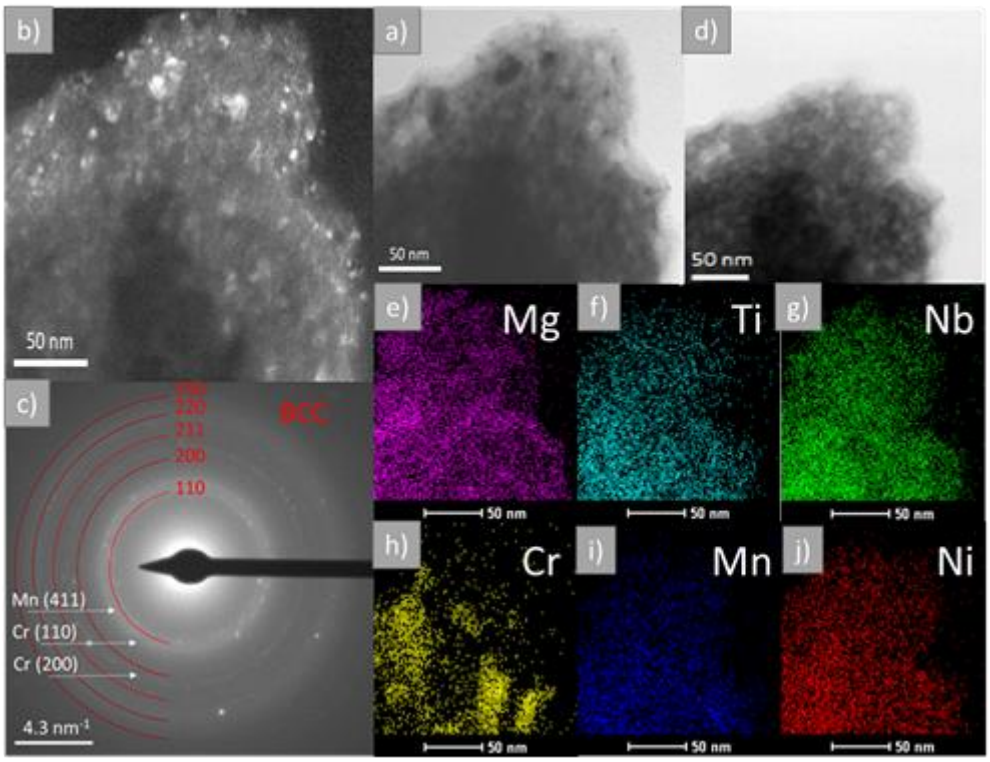

Figure 26: TEM analysis of the $Mg_{22}Ti_{22}Nb_{22}Cr_{11}Mn_{11}Ni_{11}$ MA HT, in which a) TEM-BF, b) TEM-DF, c) SAED, d) STEM-BF, and e) - j) EDX mapping.

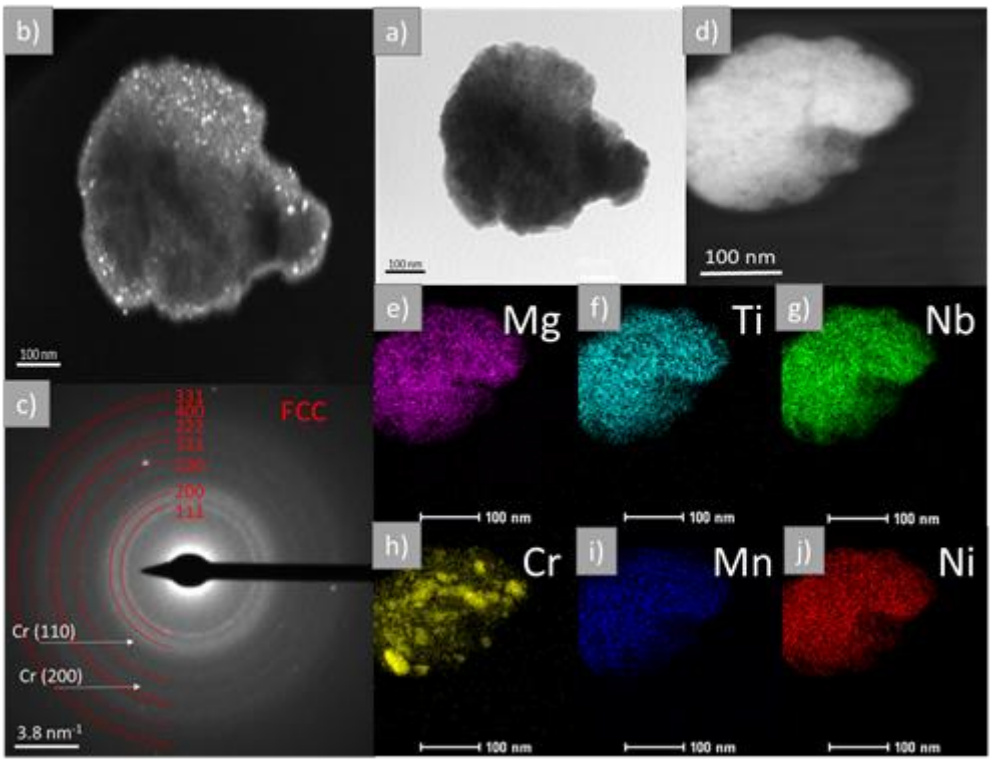

Figure 27: TEM analysis of the $Mg_{22}Ti_{22}Nb_{22}Cr_{11}Mn_{11}Ni_{11}$ RM, in which a) TEM-BF, b) TEM-DF, c) SAED, d) STEM-BF, and e) - j) EDX mapping.

Table 7 exhibits the values of enthalpy of mixing (ΔH_{mix}) for the binaries combinations in the Mg-Ti-Nb-Cr-Mn-Ni system. According to Otto *et al*.[58], the phase stability of higher-order alloys can be extended from the thermodynamic analyses of the constituent binaries. Mg presents high positive ΔH_{mix} (indicating immiscibility) with most elements except the Mg-Ni, which has ΔH_{mix} = -4 kJ/mol (indicating a tendency to forming intermediate phases). Cr presents positive ΔH_{mix} with Mg and Mn, but negative ΔH_{mix} with the other elements. A similar case is found for Mn, which has positive ΔH_{mix} only with Mg, and Cr. Ti and Nb also present positive ΔH_{mix} with two elements. However, both Ti and Nb have high interaction with Ni. The analysis of these binaries combinations might explain Mg, Cr, and Mn being identified as elemental segregates (even though Cr-Mn present some intermediate phases at room temperature [59]). Although the necessity of very low heats of mixing to form a solid solution in multicomponent systems has been advised, interestingly, this six-component system exhibits a BCC solid solution despite many atomic pairs displaying immiscibility (highly positive heats of mixing) or forming intermediate phases (highly negative heats of mixing) [47]. Synthesis of some multi-principal element solid solutions from transition metal elements and light elements, such as Mg, by non-equilibrium processes like HEBM, has been reported in the literature [60,61]. Moreover, hydrogen seems to influence sensibly the interaction among the elements, so that elements that are not likely to mix, based on the values of ΔHmix, was part of the same solid solution.

Table 7: Values of the enthalpy of mixing ΔHmix (kJ/mol) for the atomic pairs contained in the Mg-Ti-Nb-Cr-Mn-Ni system according to Ref. [31].

Element	Mg	Ti	Nb	Cr	Mn	Ni
Ti	16	-				
Nb	32	2	-			
Cr	24	-7	-7	-		
Mn	10	-8	-4	2	-	
Ni	-4	-35	-30	-7	-8	-

4.1.6 Hydrogen storage behavior of mechanically alloyed and reactive milled $Mg_{22}Ti_{22}Nb_{22}Cr_{11}Mn_{11}Ni_{11}$ alloy

In Figure 28 is shown the hydrogen desorption results from the DSC-TGA-MS measurements of the $Mg_{22}Ti_{22}Nb_{22}Cr_{11}Mn_{11}Ni_{11}$ RM. A two-peak desorption profile was recorded with an onset temperature of around 220 °C. The first endothermic peak at 300 °C corresponds to a 0.8 wt.% H_2 release, while the second one at 380 °C corresponds to another 0.8 wt.% H_2 release. The total amount of hydrogen desorbed from the reactive milled alloy is 1.6 wt.% H_2. The change in the alloy's structure after thermal analysis can be seen in Figure 28b. The decomposition of the hydride takes place with a structural transformation from FCC to BCC during hydrogen desorption, and the final structure is similar to the one obtained by MA (Figure 24). However, the lattice parameters of these alloys were different, and a shoulder in the high-Q side of the main BCC peak (110) of the alloy after desorption could not be indexed.

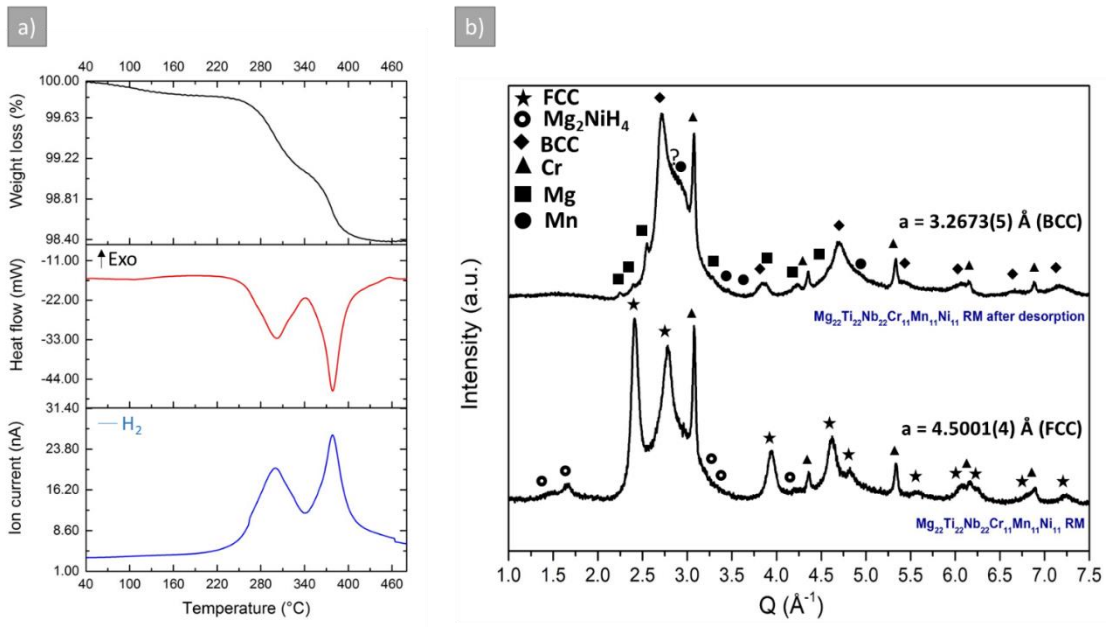

Figure 28: a) DSC/TGA and QMS of $Mg_{22}Ti_{22}Nb_{22}Cr_{11}Mn_{11}Ni_{11}$ RM. b) XRD patterns of $Mg_{22}Ti_{22}Nb_{22}Cr_{11}Mn_{11}Ni_{11}$ RM as-synthesized and after desorption in the DSC equipment. XRD measured with a Mo source (λ=0.70930 Å). The lattice parameters were obtained through Pawley Fit.

One possible explanation for the two-peak desorption profile recorded is that one of them is due to the decomposition of the Mg_2NiH_4 hydride and the other

one of the FCC hydride. According to Hou et. al., the Mg_2NiH_4 hydride synthesized by HEBM desorbs hydrogen at temperatures around 250 °C, which coincides with the first endothermic peak showed in Figure 28a [62].

The hydrogen storage behavior of the $Mg_{22}Ti_{22}Nb_{22}Cr_{11}Mn_{11}Ni_{11}$ alloy was also analyzed through in-situ synchrotron XDR measurements. The $Mg_{22}Ti_{22}Nb_{22}Cr_{11}Mn_{11}Ni_{11}$ MA HT sample was subjected to 4 MPa of H_2 and heated up to 550 ºC while XRD data were collected (Figure 29a). During heating, the reflections related to the BCC phase of the $Mg_{22}Ti_{22}Nb_{22}Cr_{11}Mn_{11}Ni_{11}$ MA HT alloy exhibited a shift towards lower Q-values, alongside the formation of non-identified reflections (represented as “?”). The main peak shift took place in the temperature range of 330°C to 450 °C (Figure 29b). After cooling to room temperature, the structure is stable. The XRD data could be fitted by Pawley Fit using a BCC structure with a lattice parameter of a = 3.4411(1) Å, which represents an expansion of the starting structure (see Fig. S9) that can be explained as hydrogen absorption by the solid solution phase. This mechanism of hydrogen absorption has been reported for some multi-principal element alloys as the first step of hydrogenation before the formation of the FCC hydride [12,43]. The behavior presented by the alloy during these in-situ measurements was similar to that recorded during the kinetics measurements exhibited previously. The expansion of the BCC phase aforementioned could be screened by in-situ XRD and again, the transformation BCC to FCC didn’t take place. The formation of the Mg_2NiH_4 hydride could not be evaluated during synchrotron measurements since no peaks from this hydride (at low angles) could be recorded due to the high background signal at low angle regions (not shown in the figures).

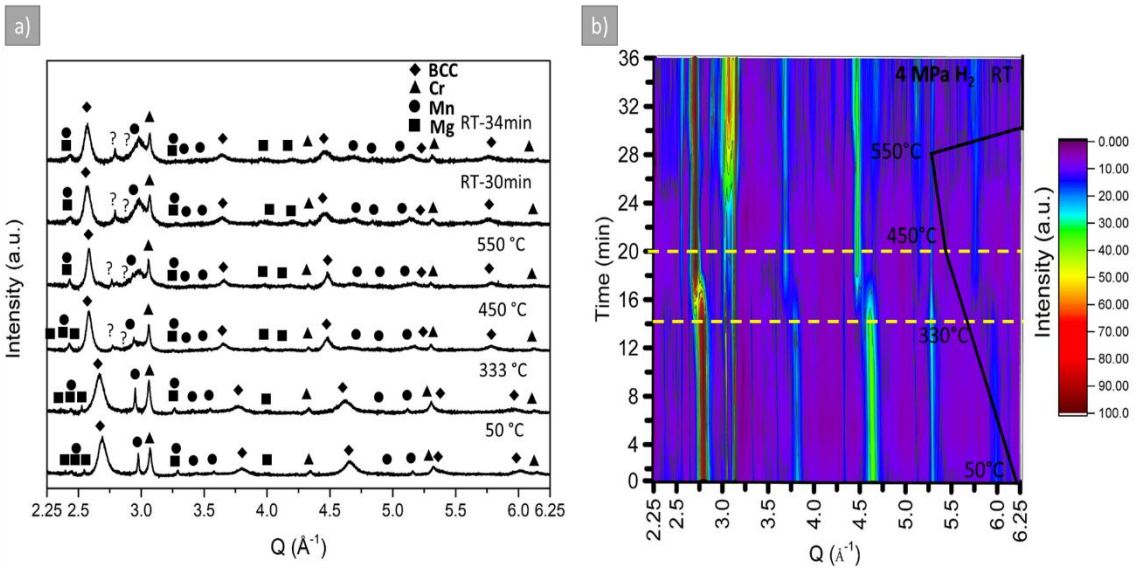

Figure 29: In-situ synchrotron powder XRD of $Mg_{22}Ti_{22}Nb_{22}Cr_{11}Mn_{11}Ni_{11}$ MA HT during hydrogen absorption. a) phase identification at different stages of the absorption process. b) XRD pattern evolution during the absorption process. The temperature range in which phase transformation takes place is highlighted. XRD measured with a synchrotron light source (λ=1.033041 Å).

The structural transformation aforementioned in the DSC-TGA-MS analysis for the $Mg_{22}Ti_{22}Nb_{22}Cr_{11}Mn_{11}Ni_{11}$ RM alloy could be screened (Figure 30) during in-situ hydrogen desorption. The formation of the BCC phase from the FCC hydride takes place instantaneously (Figure 30a). This structural transformation started at around 380 °C and finished at 450 °C (Figure 30b). Interestingly, the XRD pattern collected at the final stages of the in-situ synchrotron desorption fitted quite well using a BCC structure with lattice parameter a = 3.4300(0) Å (Fig. S10), which is similar to the structure obtained after the in-situ absorption measurements for the $Mg_{22}Ti_{22}Nb_{22}Cr_{11}Mn_{11}Ni_{11}$ MA HT (Fig. S11). These results indicate that desorption was not completed during in-situ synchrotron measurement, and remaining hydrogen was stored in the expanded BCC lattice.

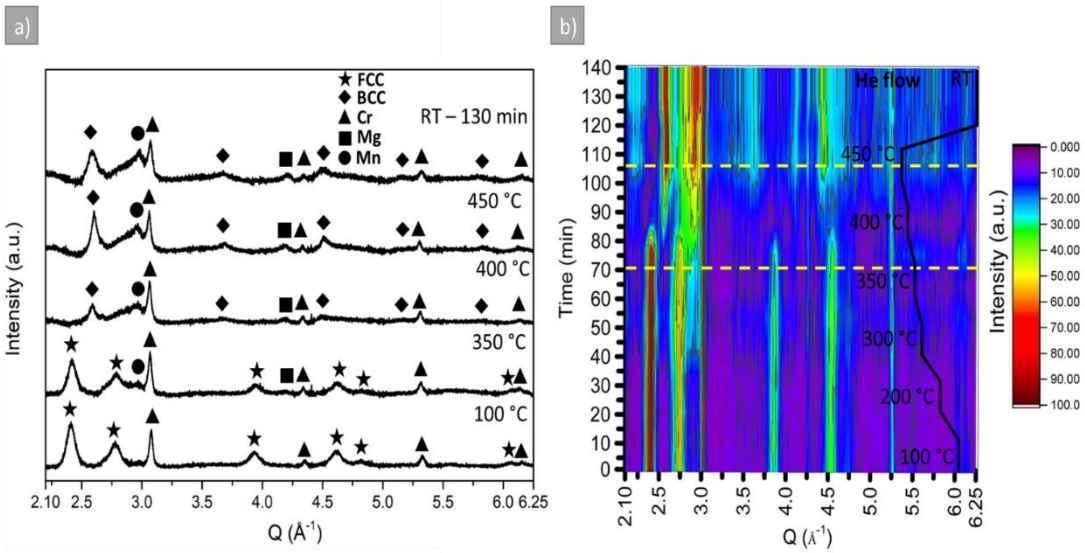

Figure 30: In-situ synchrotron powder XRD of $Mg22Ti22Nb22Cr_{11}Mn_{11}Ni_{11}$ RM during hydrogen desorption. a) Phase identification at different stages of the desorption process. b) XRD pattern evolution during the desorption process. The temperature range in which phase transformation takes place is highlighted. XRD measured with a synchrotron light source (λ=1.033041 Å).

The evaluation of the hydrogen storage behavior of $Mg_{22}Ti_{22}Nb_{22}Cr_{11}Mn_{11}Ni_{11}$ suggests that this alloy may absorb 1.6 wt. % H_2 when synthesized by RM. The results for the $Mg_{22}Ti_{22}Nb_{22}Cr_{11}Mn_{11}Ni_{11}$ MA are similar to those obtained by the kinetics measurements, i.e., the BCC phase absorbs hydrogen by solid solution expanding to a certain volume from which the absorption stops and no more transformations take place.

4.1.7 Considerations about the synthesis route

The study of the $Mg_{22}Ti_{22}Nb_{22}Cr_{11}Mn_{11}Ni_{11}$ alloy synthesized by MA and RM was helpful to understand the influence of the synthesis method in phase formation and hydrogen storage properties.

Regarding phase formation, one important aspect addressed first is that the affinity among the elements (represented by ΔH_{mix}) plays an important role in the phase formation of multicomponent element alloys. In the system under investigation, some elements presented very low miscibility when combined in pairs and consequently were segregated when mixed. It might suggest that, even though the methodology based on parameters might be helpful in alloy design,

the affinity between the elements ought to be considered since it tends to govern the phase formation during synthesis. This approach becomes fundamental when one wants to design alloys with low-density elements, not just transition metal elements, which imposes a more challenging scenario due to unfavorable ΔH_{mix} values.

Another aspect regarding phase formation is that hydrogen from RM helps in the miscibility of elements that are unlikely to mix. The presence of hydrogen in the interstitial sites of the solid solution seemed to help in the mixture of Mg and Mn with Ti, Nb, and Ni. RM also helped to increase the hydrogen storage capacity of the $Mg_{22}Ti_{22}Nb_{22}Cr_{11}Mn_{11}Ni_{11}$ alloy due to the formation of the FCC hydride. This FCC structure could not be obtained by means of hydrogen absorption from the MA sample. One explanation for this result is that RM provided the energy necessary for more complete hydrogenation.

4.2 On the Mg-Ti-Nb-Ni System

4.2.1 Selection of a new composition

Since Cr and Mn have low solubility in the solid solution of $Mg_{22}Ti_{22}Nb_{22}Cr_{11}Mn_{11}Ni_{11}$ alloy and resemble to do not influence the hydrogen storage properties (other than reducing capacity), a new composition of the Mg-Ti-Nb-Ni system was proposed in order to evaluate the influence of the removal of these elements in phase formation and hydrogen storage properties.

The selection of the composition within this new alloy system was performed considering the maximization of the φ parameter and δ parameter close to the value indicated for single-phase solid solutions (6.6 %).

Table 8 shows the values of the calculated parameters for the new composition and the equiatomic alloy for comparison.

Table 8: Calculated values of the parameters for the alloys of the Mg-Ti-Nb-Ni system.

Alloy	φ	δ (%)	Mean radius (Å)
$Mg_{25}Ti_{25}Nb_{25}Ni_{25}$	4.11	8.82	1.43
$Mg_{21}Ti_{31}Nb_{31}Ni_{17}$	6.66	7.59	1.44

The results indicate that the optimized composition, namely $Mg_{21}Ti_{31}Nb_{31}Ni_{17}$, presented better parameters towards single-phase solid solutions compared to the equiatomic one ($Mg_{25}Ti_{25}Nb_{25}Ni_{25}$).

In Figure 31, the selection of the $Mg_{21}Ti_{31}Nb_{31}Ni_{17}$ alloy is represented through the ternary diagrams. Figure 31a exhibits that the φ values increases toward the TiNb apex, which was expected since Ti and Nb present complete solubility. In order to increase the tendency to obtaining a single-phase solid solution the selected composition was chosen in a region that steps off the equiatomic one toward the TiNb apex. Considering the δ parameter, the equiatomic region presents a high value (Figure 31b), which was avoided. The value of the mean atomic radius was also optimized.

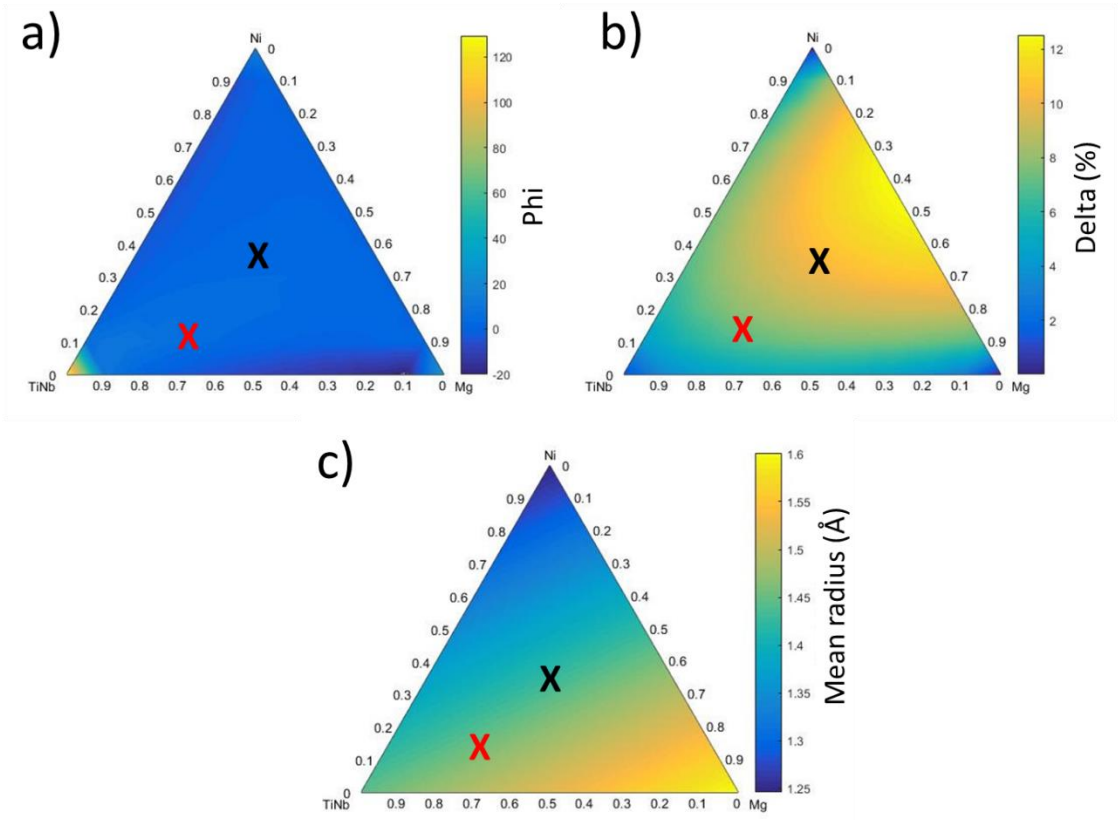

Figure 31: Calculated parameters varying all the elements in the set of compositions $Mg_xTi_{y/2}Nb_{y/2}Ni_z$ and comparison between the selected composition and the equiatomic one. (a) φ parameter (b) delta parameter (c) mean radius. The black mark refers to the equiatomic composition and the red mark refers to the selected composition.

4.2.2 Synthesis and phase formation of the $Mg_{21}Ti_{31}Nb_{31}Ni_{17}$ alloy

Table 9 exhibits the quantitative EDX results for the $Mg_{21}Ti_{31}Nb_{31}Ni_{17}$ alloy synthesized by MA and RM. As previously observed for the six-element alloys, the measured composition of $Mg_{21}Ti_{31}Nb_{31}Ni_{17}$ diverged from the theoretical one mainly for the MA process.

Table 9: Quantitative EDX results of the Mg21Ti31Nb31Ni17 alloy synthesized under 0.7 MPa of Ar (MA) and 3.0 MPa of H2 (RM).

Alloys	Mg at. (%)	Ti at. (%)	Nb at. (%)	Ni at. (%)
$Mg_{21}Ti_{31}Nb_{31}Ni_{17}$ MA	37.39	20.85	28.85	12.92
$Mg_{21}Ti_{31}Nb_{31}Ni_{17}$ RM	18.49	31.68	31.20	18.63
$Mg_{21}Ti_{31}Nb_{31}Ni_{17}$ Nominal	21.05	30.96	30.96	17.03

Figure 32 exhibits the XRD patterns collected for $Mg_{21}Ti_{31}Nb_{31}Ni_{17}$ MA, $Mg_{21}Ti_{31}Nb_{31}Ni_{17}$ MA HT, and $Mg_{21}Ti_{31}Nb_{31}Ni_{17}$ RM. The alloy synthesized by MA formed a BCC structure (W-type, $Im\bar{3}m$) with lattice parameter a = 3.2958(9) Å. After HT at 350 °C for 12 h, the BCC phase is stable even though the lattice parameter has decreased to a = 3.2877(2) Å. Concerning the presence of segregates and other phases, the $Mg_{21}Ti_{31}Nb_{31}Ni_{17}$ MA alloy represents an improvement toward a single-phase microstructure compared to the $Mg_{22}Ti_{22}Nb_{22}Cr_{11}Mn_{11}Ni_{11}$ alloy. The $Mg_{21}Ti_{31}Nb_{31}Ni_{17}$ MA just displayed two shoulders in the high Q-side of the main BCC peak (110). These reflections might be from the main peak of the TiNi phase and elemental Ni. However, since just one peak from these phases is visible, the previous statement should be considered with prudence. Moreover, elemental Ni could be replaced by FeNi (Fe being an impurity from the milling process). The XRD pattern of $Mg_{21}Ti_{31}Nb_{31}Ni_{17}$ MA HT indicates that segregation of elemental Mg from the solid solution took place during HT, which explains well the BCC's lattice parameter decrease. The intensities of the peaks from elemental segregation and additional phases suggest that the amount of them was low compared to the main BCC phase, although the real quantity of each phase could not be refined since the right composition of the solid solution is unknown.

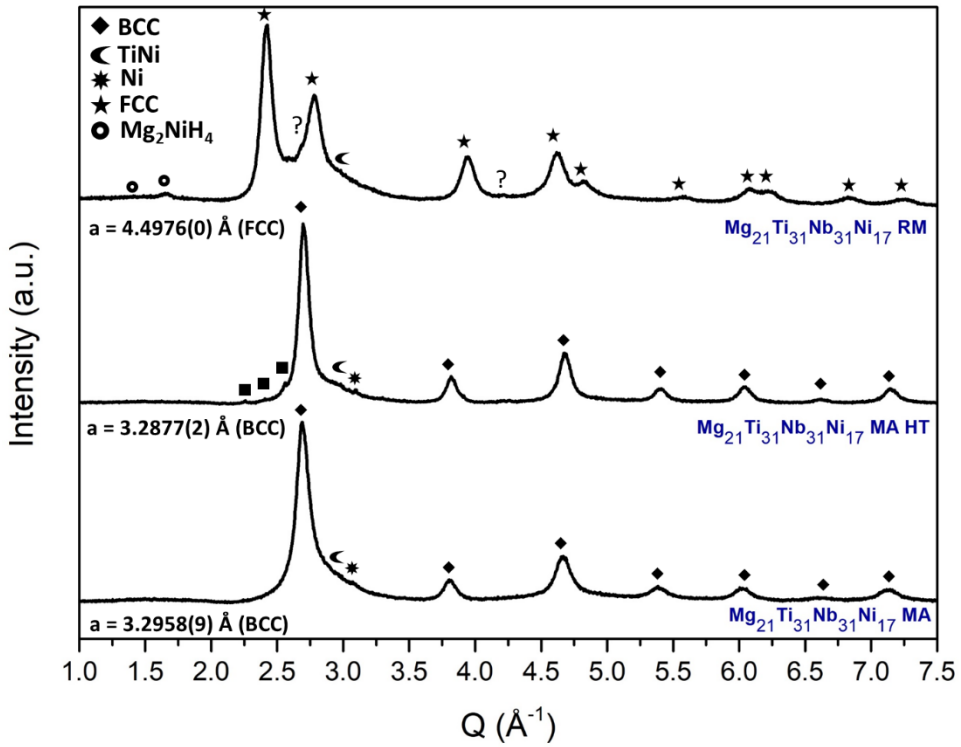

Figure 32: XRD patterns of the $Mg_{21}Ti_{31}Nb_{31}Ni_{17}$ alloy synthesized by MA, MA followed by HT (at 350 °C for 12 h), and RM. XRD measured with a Mo source (λ=0.70930 Å). The lattice parameters were obtained through Pawley Fit.

SEM images and the EDX mapping for the $Mg_{21}Ti_{31}Nb_{31}Ni_{17}$ MA HT are shown in Figure 33a. This alloy presented flat plaque particles with a broad size distribution (Figure 33a – I) and homogeneous microstructure (Figure 33a – II). The distribution of elements confirms the homogeneous microstructure, although the presence of segregated Mg is evident (Figure 33a – IV-VII). TEM images show that the crystallites with size <20 nm (Figure 34a and Figure 34b) exhibited the same structure (Figure 34c), and distribution of elements (Figure 34d-10h) in the nanometer scale. Regarding the stability of phases, it is interesting that for this alloy, a solid solution with just a few amount of secondary or segregated phases was synthesized. This might confirm that avoiding certain elements with low miscibility is fundamental for obtaining single-phase solid solutions (see Table 7). From Table 7, it was somehow expected segregation of elemental Mg as well as the formation of TiNi. However, the presence of elemental Ni is unlikely since it has negative ΔH_{mix} with all elements of the system. Comparing the solid solutions synthesized by MA from both alloys ($Mg_{22}Ti_{22}Nb_{22}Cr_{11}Mn_{11}Ni_{11}$ and

$Mg_{21}Ti_{31}Nb_{31}Ni_{17}$), it seems that they are similar in terms of structure, lattice parameter (just some deviations are noticed), and distribution of elements. Thus, it can be considered that the composition refinement towards the formation of a single BCC phase was successful.

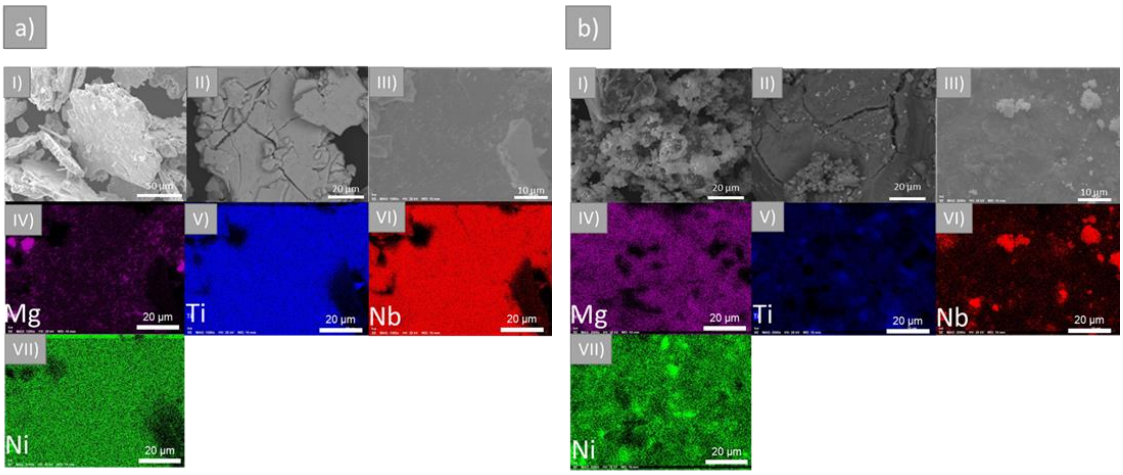

Figure 33: SEM images and EDX mapping of a) $Mg_{21}Ti_{31}Nb_{31}Ni_{17}$ MA, in which I) SEM-SE, II) SEM-BSE, III) SE-EDX, IV) - VII) EDX mapping, and b) $Mg_{21}Ti_{31}Nb_{31}Ni_{17}$ RM, in which I) SEM-SE, II) SEM-BSE, III) SE-EDX, IV-VII) EDX mapping.

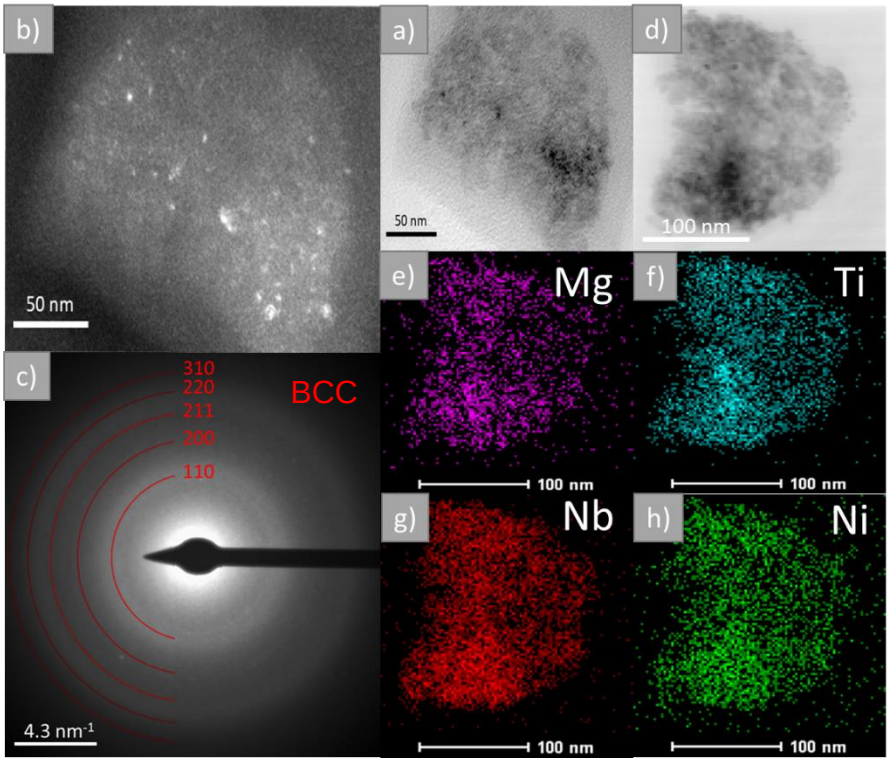

Figure 34: TEM analysis of the $Mg_{21}Ti_{31}Nb_{31}Ni_{17}$ MA HT, in which a) TEM-BF, b) TEM-DF, c) SAED, d) STEM-BF, and e) - h) EDX mapping.

The $Mg_{21}Ti_{31}Nb_{31}Ni_{17}$ alloy synthesized by RM also presents a FCC hydride phase (MH_2 with CaF_2-type structure) with a fraction of TiNi, Mg_2NiH_4, and unidentified phases. The lattice parameter of the FCC structure is a = 4.4976(0) Å (Figure 32). SE image exhibits particle sizes <10 µm (Figure 33b- I), and a microstructure with a major phase is seen in the BSE image (Figure 33b-II). The EDX mapping exhibits a main multicomponent solid solution phase (Figure 33b – IV-IX). However, some Ti-rich, Nb-rich, and Ni-rich areas were detected. These areas might correspond to the TiNi and unidentified secondary phases. In the nanometer scale, crystallites with size ≤25 nm (Figure 35a and Figure 35b) displays the same FCC structure (Figure 35c), but a homogeneous distribution of elements (Figure 35d-11h).

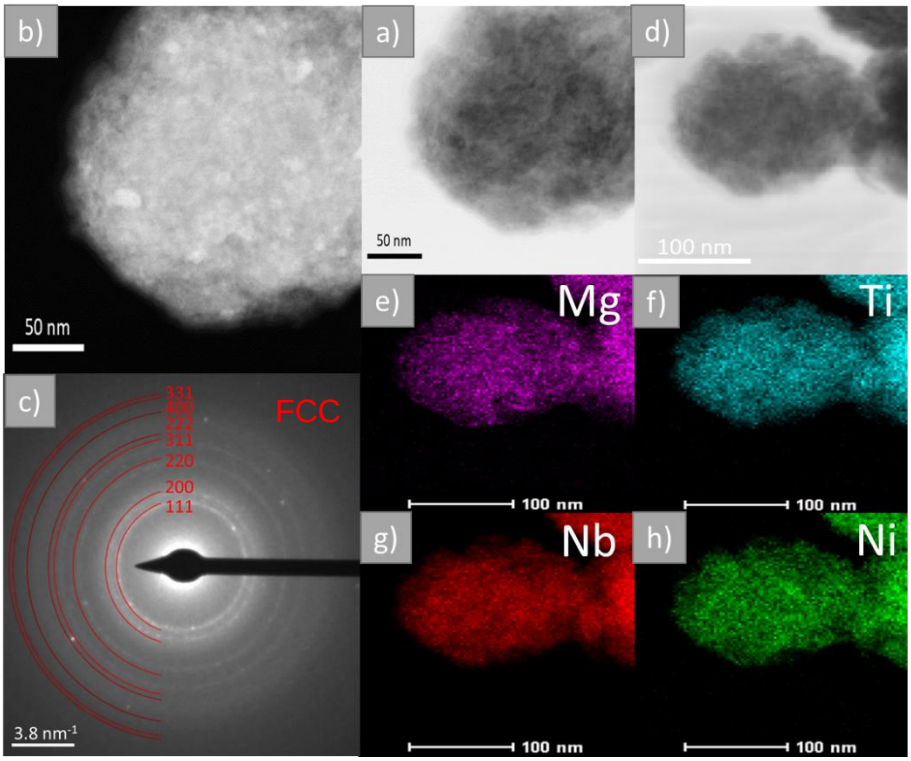

Figure 35: TEM analysis of the $Mg_{21}Ti_{31}Nb_{31}Ni_{17}$ RM, in which a) TEM-BF, b) TEM-DF, c) SAED, d) STEM-BF, and e) - h) EDX mapping.

4.2.3 Hydrogen storage behavior of the $Mg_{21}Ti_{31}Nb_{31}Ni_{17}$ alloy.

Figure 36a shows the DSC-TGA-MS results of the $Mg_{21}Ti_{31}Nb_{31}Ni_{17}$ RM. A two-peak desorption profile quite similar to the $Mg_{22}Ti_{22}Nb_{22}Cr_{11}Mn_{11}Ni_{11}$ RM

alloy was obtained, with an onset desorption temperature around 140 °C. The endothermic peaks, one at 240 °C and the other at 370 °C corresponds to a gravimetric capacity of 2.26 wt. % of H_2. Based on this result, it can be implied that the $Mg_{21}Ti_{31}Nb_{31}Ni_{17}$ alloy represents an improvement compared to the $Mg_{22}Ti_{22}Nb_{22}Cr_{11}Mn_{11}Ni_{11}$ RM in terms of gravimetric capacity. The explanation for these results concerning hydrogen storage capacity is that the relative presence of more hydride forming elements in the $Mg_{21}Ti_{31}N_{31}Ni_{17}$ alloy compared to $Mg_{22}Ti_{22}Nb_{22}Cr_{11}Mn_{11}Ni_{11}$ alloy leads to more hydrogen absorption, though the former alloy has higher molar mass (58.695 g/mol) compared to the latter (55.015 g/mol). Figure 36b exhibits the change in the alloy's structure after thermal analysis. The FCC to BCC phase transition took place during hydrogen desorption, and the final structure is slightly similar to the one obtained by MA (Figure 32). Regarding the presence of secondary phases and segregates after hydrogen desorption, the alloys' microstructure is composed of elemental Mg and Ni (possibly the products of Mg_2NiH_4 decomposition) and a substantial amount of TiNi.

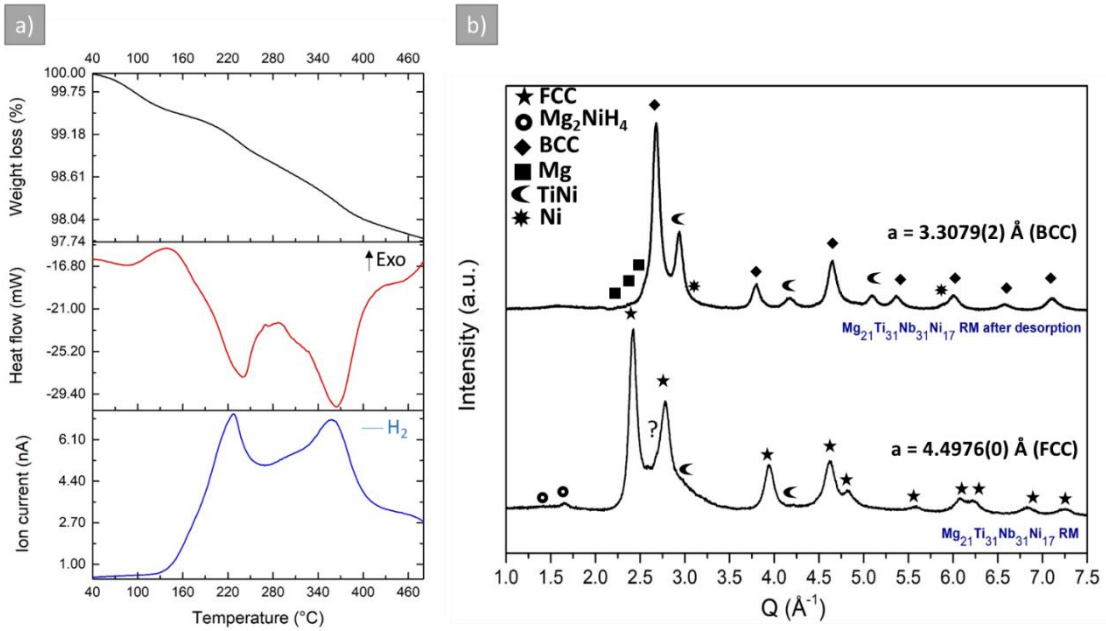

Figure 36: a) DSC/TGA and QMS of $Mg_{21}Ti_{31}N_{31}Ni_{17}$ RM. b) XRD patterns of $Mg_{21}Ti_{31}N_{31}Ni_{17}$ RM as-synthesized and after desorption in the DSC equipment. XRD measured with a Mo source (λ=0.70930 Å). The lattice parameters were obtained through Pawley Fit.

In-situ synchrotron XDR measurements were also used to evaluate the hydrogen storage behavior of the $Mg_{21}Ti_{31}N_{31}Ni_{17}$ alloy. The $Mg_{21}Ti_{31}N_{31}Ni_{17}$ MA HT was heated up to 550 ºC under 4.0 MPa of H_2 pressure (Figure 37). The reflections related to the BCC phase exhibited a shift towards lower Q-values during heating, alongside the formation of non-identified reflections (represented as “?”). The main peak shift at this stage took place in the temperature range of 350°C to 488 °C (Figure 37b). The XRD pattern could be fitted by Pawley Fit using a BCC structure with a lattice parameter of a = 3.4338(8) Å, which also represents an expansion of the starting BCC structure (see Fig. S11) that can be explained as absorption of hydrogen by the solid solution phase. In the course of cooling to room temperature, however, a fraction of the expanded BCC phase transformed into another structure that could be fitted as a FCC structure with a lattice parameter of a = 4.5523(9) Å (Fig. S11). Interestingly, the transition from BCC to FCC structures observed during cooling to room temperature is similar to what happens in the Nb-H system at high hydrogen weight percent [63]. It is well known that the equilibrium pressure of hydrogenation of metal hydrides as a function of temperature can be described by Van’t Hoff equation, which indicates that higher equilibrium pressures are found for higher temperatures [64]. Based on this, it can be implied that the equilibrium pressure for the observed transition is higher than 4 MPa at temperatures around 550 °C, yet it is lowered below 4 MPa during cooling to room temperature. In other words, it might be the case that the driving force for this transition was reached during cooling due to lower equilibrium pressure.

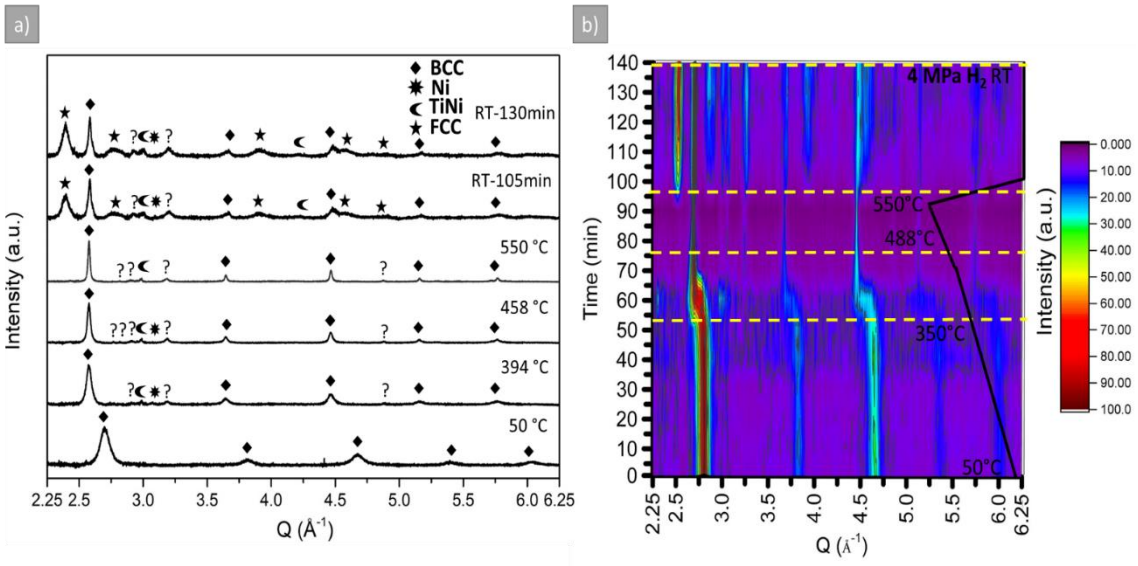

Figure 37: In-situ synchrotron powder XRD of $Mg_{21}Ti_{31}N_{31}Ni_{17}$ MA HT during hydrogen absorption. a) phase identification at different stages of the absorption process. b) XRD pattern evolution during the absorption process. The temperature ranges in which phases transformations take place are highlighted. XRD measured with a synchrotron light source (λ=1.033041 Å).

The behavior of the $Mg_{21}Ti_{31}N_{31}Ni_{17}$ RM alloy during desorption was also screened by in-situ synchrotron XRD (Figure 38). Here again, the formation of the BCC phase takes place with the consumption of the FCC hydride (Figure 38a). This structural transformation started at around 300 °C and finished at 350 °C (Figure 38b). The XRD pattern collected at the final stages of the in- situ synchrotron desorption fitted quite well using a BCC structure with lattice parameter a = 3.4212(1) Å (Fig. S12), which also indicates that desorption was not completed during in-situ synchrotron measurement since this structure is similar to the one obtained after the in-situ absorption measurements for the $Mg_{21}Ti_{31}N_{31}Ni_{17}$ MA HT (Fig. S11).

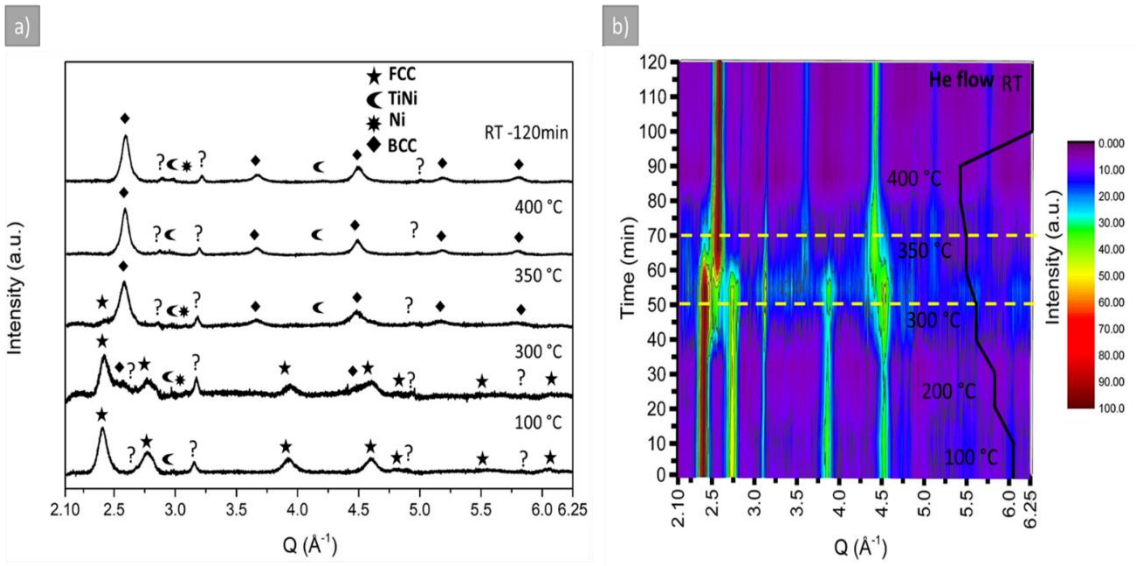

Figure 38: In-situ synchrotron powder XRD of $Mg_{21}Ti_{31}N_{31}Ni_{17}$ RM during hydrogen desorption. a) phase identification at different stages of the desorption process. b) XRD pattern evolution during the desorption process. The temperature range in which phase transformation takes place is highlighted. XRD measured with a synchrotron light source (λ=1.033041 Å).

To evaluate the complete dehydrogenation of the RM sample, another in-situ XRD experiment was performed, but this time using an STOE Powder Diffraction System, not a synchrotron beamline. This experiment was performed by heating the sample from 30°C to 500 °C by steps under Ar flow, and during the heating ramp, no diffraction pattern was recorded, that is why just the measuring time is exhibited in Figure 39. The initial desorption behavior exhibited in Figure 39 is similar to that one showed in Figure 38, that hydrogen was released and a structural transformation from FCC to BCC took place at temperatures up to 400 °C. Some differences regarding the temperatures at which the changes took place can be noted, but they might be related to the different heating systems and gas flow used. From 400 °C to 500 °C, it can be noted in Figure 39b that there was a shift in the peaks of the BCC phase towards high Q angles. This can be confirmed in Figure 39a and it can be seen that the lattice parameter of this phase shrank from a=3.4136(5) Å to a=3.3257(7) Å, which represents 8.14% of unit cell volume contraction. Alongside the BCC phase contraction, the presence of TiNi could be noticed as a function of temperature.

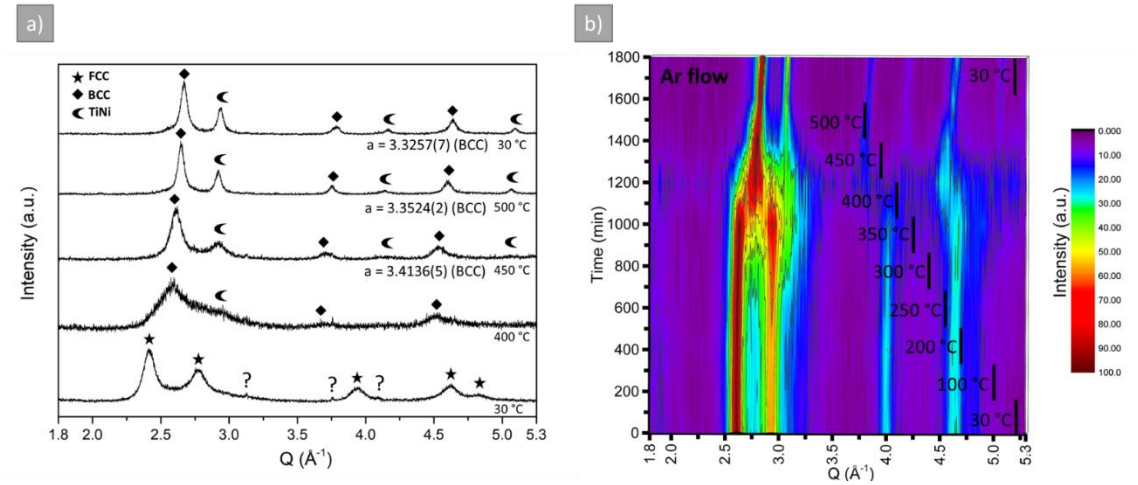

Figure 39: In-situ powder XRD of $Mg_{21}Ti_{31}N_{31}Ni_{17}$ RM during hydrogen desorption. a) phase identification at different stages of the desorption process. b) XRD pattern evolution during the desorption process. XRD measured with a Mo source (λ=0.70930 Å).

It can be considered that, during heating, there was a decomposition of the BCC phase with the formation of TiNi, which might correspond to the BCC shrinkage. However, it can be noticed that even in the as milled product (represent by the FCC pattern at 30 °C) there is a shoulder in the XRD pattern around Q=2.8 $Å^{-1}$, the region of the highest intense peak of TiNi. It might suggest that TiNi was formed during alloy synthesis, but it was very deformed due to ball milling. With temperature, recuperation and recrystallization took place, with an increase in the crystallite size and a reduction in the microstrain, diminishing the XRD pattern line broadening correspondent to this phase. Thus, one plausible explanation, combined with the DSC results of Figure 28 and Figure 36, is that hydrogen was released from the FCC structure during heating alongside the desorption of the Mg_2NiH_4 hydride (whose fraction is considerably lower when compared to the $Mg_{22}Ti_{22}Nb_{22}Cr_{11}Mn_{11}Ni_{11}$ RM alloy). After the end of structural transformation (FCC to BCC), hydrogen in solid solution in the BCC structure was released in another moment at higher temperatures, i.e., hydrogen was released from the multicomponent solid solution in two different temperatures. The divergences between the in-situ XRD, in-situ synchrotron and DSC measurements regarding temperatures at which transformations took place might

be due to differences in the heating systems and heating rates used, and because the experiments were performed under different gas flow (He and Ar) with different flow rates. Although this desorption mechanism considered in the explanation is not typical for the classical BCCs or even for high entropy alloys that form BCC solid solutions [27,45], it was reported for the $MgTiZrFe_{0.5}Co_{0.5}Ni_{0.5}$ alloy [12].

Another aspect of the hydrogen storage behavior of the $Mg_{21}Ti_{31}N_{31}Ni_{17}$ composition was analyzed by means of activation procedure and PCI measurements. The $Mg_{21}Ti_{31}N_{31}Ni_{17}$ MA was submitted to two cycles of hydrogen absorption/desorption in an autoclave as indicated in the methodology section. Figure 40 exhibits the XRD pattern for the alloy after activation. The BCC phase was preserved, but it has a lattice parameter of a= 3.3570(7) Å, which is higher than that of the heat treated sample (a=3.2877(2) Å from Figure 32). This result suggested that the BCC phase is expanded, probably due to the remaining hydrogen in the structure. Different secondary phases were also noted, indicating that during hydrogen cycling further segregation of elements or formation of phases takes place.

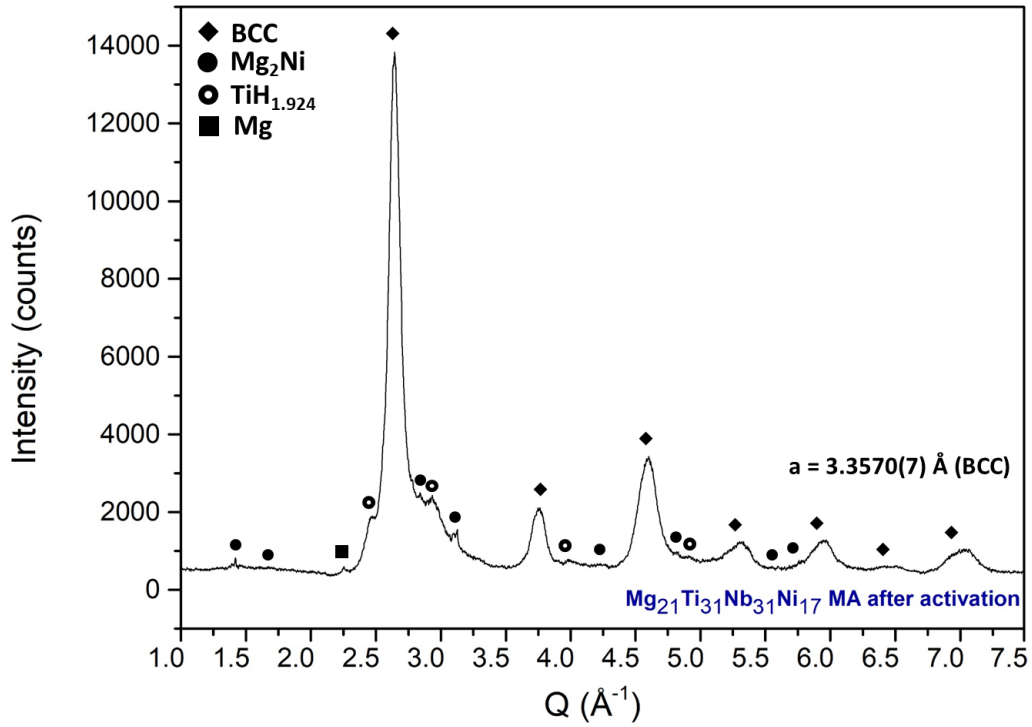

Figure 40: XRD pattern of the $Mg_{21}Ti_{31}N_{31}Ni_{17}$ MA HT after activation cycling. XRD measured with a Mo source (λ=0.70930 Å).

After the activation procedure in an autoclave, the sample was submitted to PCI measurements. All the measurements were performed for the same sample. Figure 41 shows the isotherms obtained during the experiment. The sample was submitted to a desorption procedure at 375 °C for 3h under a dynamic vacuum prior to the first isotherm. This desorption temperature was selected because it is the temperature for the second peak desorption obtained in the DSC/TGA of Figure 36. The sequence of measurements was from 350 °C to 300 °C and between each absorption isotherm, a desorption procedure at 375°C for 3h under dynamic vacuum was conducted. The temperatures from 350 °C to 300 °C were selected because no absorption was obtained below this range of temperature.

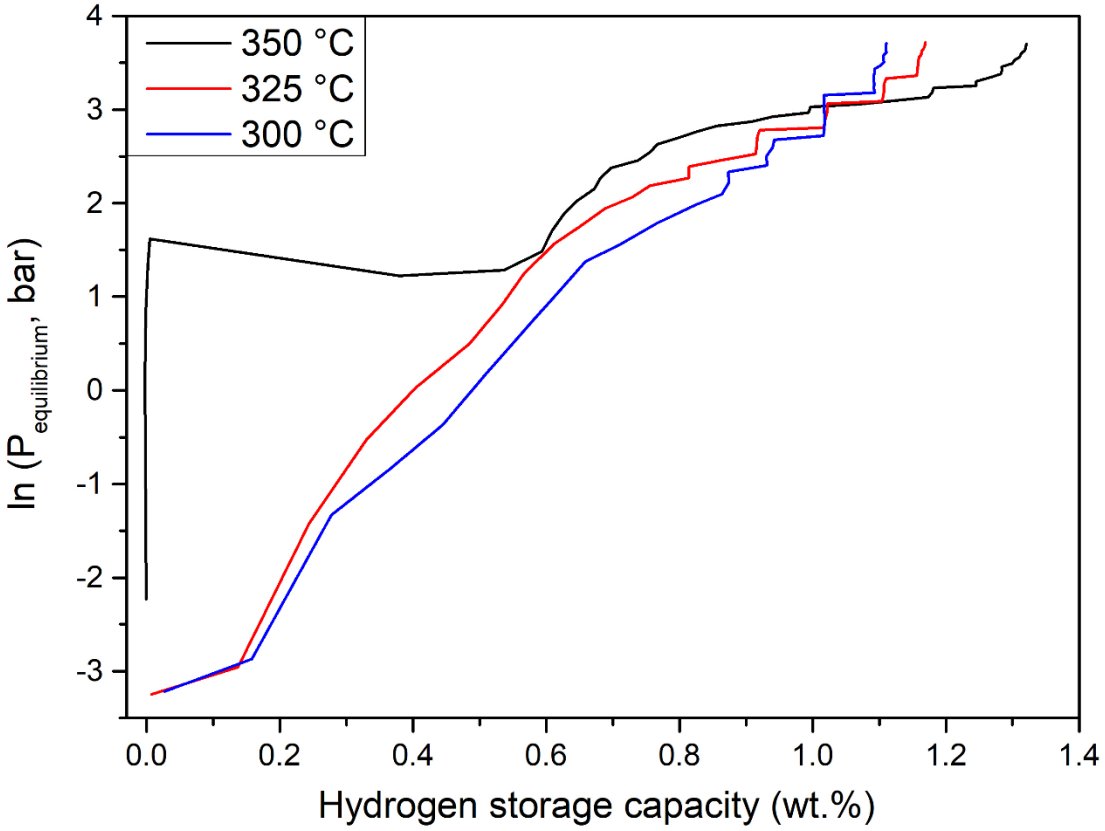

Figure 41: PCI isotherms performed with the $Mg_{21}Ti_{31}N_{31}Ni_{17}$ MA HT after activation at temperatures of 350 °C, 325°C and 300 °C with a maximum pressure of 40 bar.

The isotherms presented similar behavior, with an exception for the isotherm at 350 °C up to 4.48 bar (lnP_{eq}=1.5). This anomalous behavior for the

first region of the isotherm at 350 °C can be associated with an activation process since it was the first isotherm to be run after the transference from the autoclave to the PCT-Pro 2000 sample holder. Although standard procedures were used during the transference of the sample, there is no guarantee that it was not exposed to some content of air, causing oxidation after the activation procedure. Another possibility is that the activation was not completed previously, taking place during the first isotherm. Excluding the first region of the isotherm at 350 °C, associated with an activation process, there are no evident plateau regions in the isotherms recorded. The plateau region is characteristic of hydride formation when the equilibrium pressure for the hydrogenation reaction is achieved after the saturation of the solution phase [64]. The absence of a plateau might indicate that under the experimental conditions (temperature and pressure), either no hydride formation occurred and hydrogen was absorbed just by solid solution or that the major phase absorbed by solid solution and minor hydride formation took place. Higher values of pressure were found for the higher temperatures, which is in accordance with the thermodynamics and regarding the maximum hydrogen storage capacity, it is noticed that this value decreased slightly over the cycles, from 1.3 wt. % of H_2 at 350°C to 1.1 wt. % of H_2 at 300°C.

Figure 42 exhibits the XRD pattern for the sample after PCI at 300 °C without desorption procedure.

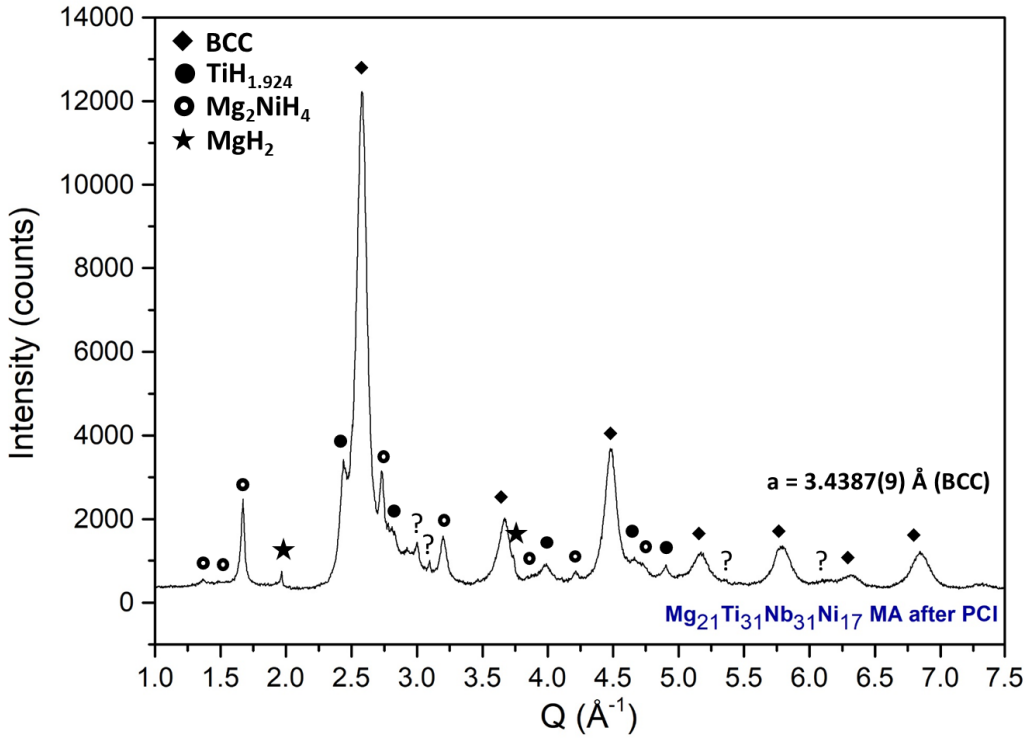

Figure 42: XRD patterns of the $Mg_{21}Ti_{31}N_{31}Ni_{17}$ MA HT after activation and PCI. XRD measured with a Mo source (λ=0.70930 Å).

This XRD pattern indicates that hydrogen was absorbed by the BCC phase by solid solution, resulting in its expansion, but also other types of hydrides besides the Mg_2NiH_4 hydride was formed. Evaluating the PCI based on the XRD of Figure 42, it can be implied that the behavior recorded by the isotherms represents majorly the BCC phase hydrogen absorption by solid solution. Considering that the calculated equilibrium pressure at 325 °C is around 0.26 bar (lnP_{eq}= -1.35), 2.64 bar (lnP_{eq}= 0.97), and 1.65x10^{-6} bar (lnP_{eq}= -13.31) for Mg_2NiH_4, MgH_2, and TiH_2, respectively, the formation of these hydrides are very likely under the PCI experimental condition performed, although it may be that the BCC solution formation has overlaid their plateaus. The equilibrium pressures were calculated considering the hydride's enthalpy and entropy found in [14] and [6]. The results also suggested that the BCC phase kept its capacity of absorbing hydrogen over 5 cycles; however, no structural transformation BCC to FCC was obtained again. Instead of the phase transition, further segregation and formation of secondary hydrides took place and influenced the hydrogen storage properties of the $Mg_{21}Ti_{31}N_{31}Ni_{17}$ alloy.

4.2.4 Considerations about the Mg-Ti-Nb-Ni system

The proposal of the $Mg_{21}Ti_{31}N_{31}Ni_{17}$ alloy based on the Mg-Ti-Nb-Ni system brought improvements in terms of phase formation and hydrogen storage behavior. This alloy presented a less complex microstructure (less secondary phases) compared to the $Mg_{22}Ti_{22}Nb_{22}Cr_{11}Mn_{11}Ni_{11}$ alloy, which indicates that single phase solid solution formation is conditioned to systems that present favorable miscibility, even when HEBM is used as a synthesis method. Regarding hydrogen storage behavior, the $Mg_{21}Ti_{31}N_{31}Ni_{17}$ alloy absorbed hydrogen reversibly and seemed to present a reversible structural transformation BCC to FCC under strict conditions. By PCI it could be observed that at temperatures from 350 °C to 300 °C the alloy absorbed hydrogen majorly by solid solution until the point of saturation with an expansion of the BCC phase and gravimetric capacity of around 1.3 wt.% of H_2. However, no further transformation took place, which might suggest that either this is the absorption limit or different conditions (temperature and pressure) must be applied for further hydrogen absorption. Indeed, the *in situ* synchrotron XRD results of Figure 37 indicated that further transformation may take place under conditions that allow reaching the driving force for the BCC to FCC transition (room temperature under 40 bar of H_2 or pressures higher than 40 bar of H_2 at temperatures around 350 °C). Thus, in the present work, the FCC hydride could be formed at room temperature under 40 bar of H_2 and by RM under 30 bar of H_2. The RM sample presented a gravimetric capacity of 2.26 wt. % of H_2. Yet, in the case that just a single-phase solid solution was synthesized and all the tetrahedral interstitial sites of the FCC phase were occupied by hydrogen, resulting in hydrogen over metal ratio - H/M=2, the gravimetric capacity of the $Mg_{21}Ti_{31}N_{31}Ni_{17}$ alloy would be 3.3 wt. % H_2, which suggests the potential for hydrogen storage of multicomponent alloys with low-density elements. The cycling behavior of the $Mg_{21}Ti_{31}N_{31}Ni_{17}$ alloy could be evaluated by means of the activation and the PCI measurements. The tendency of elements segregation and formation of secondary phases over cycling with reduction of the gravimetric capacity were evident, which might limit the possibility of application of this composition for hydrogen storage in reversible tanks.

5. CONCLUSION

In the present work, Mg-containing multicomponent compositions from the Mg-Ti-Nb-Cr-Mn-Ni and Mg-Ti-Nb-Ni systems were investigated in terms of phase formation, stability and hydrogen storage behavior. The following conclusions can be highlighted:

- The alloys High phi, High delta and Equiatomic formed BCC solid solutions. However, no single-phase was obtained and the formation of segregation of Mg, Mn and Cr was observed. Thus, unfavorable mixing enthalpy between some elements within the system limited the single-phase solid solution formation and the stability of the alloys, since the interaction between the pairs of elements tends to rule phase formation and stability of high-order alloys.
- Although all the three mentioned alloys absorbed hydrogen, no correlation between the hydrogen storage behavior of them and the calculated parameters could be established.
- The Equiatomic alloy ($Mg_{22}Ti_{22}Nb_{22}Cr_{11}Mn_{11}Ni_{11}$) forms a major BCC solid solution when synthesized by MA absorbing 1.18 wt.% of H_2 and forms a major FCC hydride when synthesized by RM desorbing 1.6 wt% of H_2.
- No phase transition BCC to FCC could be observed for the $Mg_{22}Ti_{22}Nb_{22}Cr_{11}Mn_{11}Ni_{11}$ alloy.
- The $Mg_{21}Ti_{31}N_{31}Ni_{17}$ alloy forms an almost single-phase BCC solid solution when synthesized by MA and an almost single-phase FCC hydride when synthesized by RM. It indicates that removal of unfavorable elements, such as Cr and Mn in the Mg-Ti-Nb-Cr-Mn-Ni system, was a successful strategy towards single-phase solid solution formation
- PCI measurements indicate that the $Mg_{21}Ti_{31}N_{31}Ni_{17}$ MA alloy absorbs around 1.3 wt.% of H_2, whereas DSC/TGA measurements indicate that the $Mg_{21}Ti_{31}N_{31}Ni_{17}$ RM desorbs 2.26 wt.% of H_2.
- The reversible transition BCC to FCC was observed for the $Mg_{21}Ti_{31}N_{31}Ni_{17}$ alloy. However, it happened under restrict conditions.
- Considering the effort in terms of research to increase the hydrogen storage gravimetric capacity of multicomponent alloys above 2.5 wt. %,

the use of light elements seems to be mandatory. Mg is a promising element; however phase formation and stability of Mg-containing compositions have to be improved.

6. FUTURE WORK PROPOSAL

The following suggestions for future work are proposed:

- Evaluate the accuracy of the alloy selection method in predicting single-phase solid solutions with compositions that present $\varphi \geq 20$. Obtaining single-phase solid solutions, evaluate the influence of δ in hydrogen storage properties.
- Evaluate the stability of phases of Mg-containing multicomponent compositions and, if possible, propose means of increasing phase stability for similar compositions.
- Investigate new low-density multicomponent compositions for hydrogen storage.

7. REFERENCES

[1] E.M. Do Sacramento, P.C.M. Carvalho, L.C. de Lima, T.N. Veziroglu, Feasibility study for the transition towards a hydrogen economy: A case study in Brazil, Energy Policy. 62 (2013) 3–9. doi:10.1016/j.enpol.2013.06.071.

[2] H. Chen, T.N. Cong, W. Yang, C. Tan, Y. Li, Y. Ding, Progress in electrical energy storage system: A critical review, Prog. Nat. Sci. 19 (2009) 291–312. doi:10.1016/j.pnsc.2008.07.014.

[3] F. Zhang, P. Zhao, M. Niu, J. Maddy, The survey of key technologies in hydrogen energy storage, Int. J. Hydrogen Energy. 41 (2016) 14535–14552. doi:10.1016/j.ijhydene.2016.05.293.

[4] A. Kirubakaran, S. Jain, R.K. Nema, A review on fuel cell technologies and power electronic interface, Renew. Sustain. Energy Rev. 13 (2009) 2430–2440. doi:10.1016/j.rser.2009.04.004.

[5] Y. Wang, D.F. Ruiz Diaz, K.S. Chen, Z. Wang, X.C. Adroher, Materials, technological status, and fundamentals of PEM fuel cells – A review, Mater. Today. xxx (2019). doi:10.1016/j.mattod.2019.06.005.

[6] Q. Lai, Y. Sun, T. Wang, P. Modi, C. Cazorla, U.B. Demirci, J.R. Ares Fernandez, F. Leardini, K.F. Aguey-Zinsou, How to Design Hydrogen Storage Materials? Fundamentals, Synthesis, and Storage Tanks, Adv. Sustain. Syst. 3 (2019) 1–64. doi:10.1002/adsu.201900043.

[7] L.F. Chanchetti, S.M. Oviedo Diaz, D.H. Milanez, D.R. Leiva, L.I.L. de Faria, T.T. Ishikawa, Technological forecasting of hydrogen storage materials using patent indicators, Int. J. Hydrogen Energy. 41 (2016) 18301–18310. doi:10.1016/j.ijhydene.2016.08.137.

[8] B. Sakintuna, F. Lamari-Darkrim, M. Hirscher, Metal hydride materials for solid hydrogen storage: A review, Int. J. Hydrogen Energy. 32 (2007) 1121–1140. doi:10.1016/j.ijhydene.2006.11.022.

[9] J.W. Yeh, S.K. Chen, S.J. Lin, J.Y. Gan, T.S. Chin, T.T. Shun, C.H. Tsau, S.Y. Chang, Nanostructured high-entropy alloys with multiple principal

elements: Novel alloy design concepts and outcomes, Adv. Eng. Mater. 6 (2004) 299-303+274. doi:10.1002/adem.200300567.

[10] M. Sahlberg, D. Karlsson, C. Zlotea, U. Jansson, Superior hydrogen storage in high entropy alloys, Sci. Rep. 6 (2016) 1–6. doi:10.1038/srep36770.

[11] C. Zlotea, M.A. Sow, G. Ek, J.-P. Couzinié, L. Perrière, I. Guillot, J. Bourgon, K.T. Møller, T.R. Jensen, E. Akiba, M. Sahlberg, Hydrogen sorption in TiZrNbHfTa high entropy alloy, J. Alloys Compd. (2018). doi:10.1016/j.jallcom.2018.10.108.

[12] G. Zepon, D.R. Leiva, R.B. Strozi, A. Bedoch, S.J.A. Figueroa, T.T. Ishikawa, W.J. Botta, Hydrogen-induced phase transition of MgZrTiFe0.5Co0.5Ni0.5high entropy alloy, Int. J. Hydrogen Energy. 43 (2018) 1702–1708. doi:10.1016/j.ijhydene.2017.11.106.

[13] G.G. Libowitz, Metallic hydrides; fundamental properties and applications, J. Phys. Chem. Solids. 55 (1994) 1461–1470. doi:10.1016/0022-3697(94)90571-1.

[14] G. Sandrock, Panoramic overview of hydrogen storage alloys from a gas reaction point of view, J. Alloys Compd. 293 (1999) 877–888. doi:10.1016/S0925-8388(99)00384-9.

[15] P. Dantzer, Metal-Hydride technology: A critical review, Hydrog. Met. III. 73 (1997) 279–340. doi:10.1007/BFb0103405.

[16] P. Chen, M. Zhu, Recent progress in hydrogen storage, Mater. Today. 11 (2008) 36–43. doi:10.1016/S1369-7021(08)70251-7.

[17] F.D. Manchester, D. Khatamian, The activation of FeTi for hydrogen absorption: progress and possibilities, J. Less-Common Met. 130 (1987) 459. doi:10.1016/0022-5088(87)90141-X.

[18] J.J. Reilly, R.H. Wiswall, Formation and properties of iron titanium hydride, Inorg. Chem. 13 (1974) 218–222. doi:10.1021/ic50131a042.

[19] M. Norek, T.K. Nielsen, M. Polanski, I. Kunce, T. Płociński, L.R. Jaroszewicz, Y. Cerenius, T.R. Jensen, J. Bystrzycki, Synthesis and decomposition mechanisms of ternary Mg2CoH 5 studied using in situ

synchrotron X-ray diffraction, Int. J. Hydrogen Energy. 36 (2011) 10760–10770. doi:10.1016/j.ijhydene.2011.05.126.

[20] D.R. Leiva, G. Zepon, A.A.C. Asselli, D. Fruchart, S. Miraglia, T.T. Ishikawa, W.J. Botta, Mechanochemistry and H-sorption properties of Mg 2FeH 6-based nanocomposites, Int. J. Mater. Res. 103 (2012) 1147–1154. doi:10.3139/146.110806.

[21] K.J. Gross, D. Chartouni, E. Leroy, A. Züttel, L. Schlapbach, Mechanically milled Mg composites for hydrogen storage: The relationship between morphology and kinetics, J. Alloys Compd. 269 (1998) 259–270. doi:10.1016/S0925-8388(97)00627-0.

[22] A.A.C. Asselli, D.R. Leiva, A.M. Jorge, T.T. Ishikawa, W.J. Botta, Synthesis and hydrogen sorption properties of Mg 2FeH 6-MgH 2 nanocomposite prepared by reactive milling, J. Alloys Compd. 536 (2012) S250–S254. doi:10.1016/j.jallcom.2011.12.103.

[23] G. Zepon, D.R. Leiva, M.J. Kaufman, S.J.A. Figueroa, R. Floriano, D.G. Lamas, A.A.C. Asselli, W.J. Botta, Controlled mechanochemical synthesis and hydrogen desorption mechanisms of nanostructured Mg2CoH5, Int. J. Hydrogen Energy. 40 (2015) 1504–1515. doi:10.1016/j.ijhydene.2014.11.085.

[24] M.D. Riktor, S. Deledda, M. Herrich, O. Gutfleisch, H. Fjellvåg, B.C. Hauback, Hydride formation in ball-milled and cryomilled Mg-Fe powder mixtures, Mater. Sci. Eng. B Solid-State Mater. Adv. Technol. 158 (2009) 19–25. doi:10.1016/j.mseb.2008.12.031.

[25] L. Mendoza-Zélis, M. Meyer, L. Baum, Complex quaternary hydrides Mg2(Fe,Co)Hyfor hydrogen storage, Int. J. Hydrogen Energy. 36 (2011) 600–605. doi:10.1016/j.ijhydene.2010.09.076.

[26] I.G. Fernández, G.O. Meyer, F.C. Gennari, Hydriding/dehydriding behavior of Mg2CoH5 produced by reactive mechanical milling, J. Alloys Compd. 464 (2008) 111–117. doi:10.1016/j.jallcom.2007.09.102.

[27] S. Miraglia, D. Fruchart, N. Skryabina, M. Shelyapina, B. Ouladiaf, E.K. Hlil, P. de Rango, J. Charbonnier, Hydrogen-induced structural transformation in TiV0.8Cr1.2studied by in situ neutron diffraction, J. Alloys Compd. 442

(2007) 49–54. doi:10.1016/j.jallcom.2006.10.168.

[28] K. Edalati, M. Matsuo, H. Emami, S. Itano, A. Alhamidi, A. Staykov, D.J. Smith, S. ichi Orimo, E. Akiba, Z. Horita, Impact of severe plastic deformation on microstructure and hydrogen storage of titanium-iron-manganese intermetallics, Scr. Mater. 124 (2016) 108–111. doi:10.1016/j.scriptamat.2016.07.007.

[29] B. Cantor, I.T.H. Chang, P. Knight, A.J.B. Vincent, Microstructural development in equiatomic multicomponent alloys, Mater. Sci. Eng. A. 375–377 (2004) 213–218. doi:10.1016/j.msea.2003.10.257.

[30] J.W. Yeh, S.K. Chen, J.Y. Gan, S.J. Lin, T.S. Chin, T.T. Shun, C.H. Tsau, S.Y. Chang, Formation of simple crystal structures in Cu-Co-Ni-Cr-Al-Fe-Ti-V alloys with multiprincipal metallic elements, Metall. Mater. Trans. A Phys. Metall. Mater. Sci. 35 A (2004) 2533–2536. doi:10.1007/s11661-006-0234-4.

[31] D.B. Miracle, O.N. Senkov, A critical review of high entropy alloys and related concepts, Acta Mater. 122 (2017) 448–511. doi:10.1016/j.actamat.2016.08.081.

[32] M.H. Tsai, J.W. Yeh, High-entropy alloys: A critical review, Mater. Res. Lett. 2 (2014) 107–123. doi:10.1080/21663831.2014.912690.

[33] J.W. Yeh, Physical Metallurgy of High-Entropy Alloys, Jom. 67 (2015) 2254–2261. doi:10.1007/s11837-015-1583-5.

[34] D. Choudhuri, B. Gwalani, S. Gorsse, C. V. Mikler, R. V. Ramanujan, M.A. Gibson, R. Banerjee, Change in the primary solidification phase from fcc to bcc-based B2 in high entropy or complex concentrated alloys, Scr. Mater. 127 (2017) 186–190. doi:10.1016/j.scriptamat.2016.09.023.

[35] C. Zhang, F. Zhang, H. Diao, M.C. Gao, Z. Tang, J.D. Poplawsky, P.K. Liaw, Understanding phase stability of Al-Co-Cr-Fe-Ni high entropy alloys, Mater. Des. 109 (2016) 425–433. doi:10.1016/j.matdes.2016.07.073.

[36] H.W. Yao, J.W. Qiao, J.A. Hawk, H.F. Zhou, M.W. Chen, M.C. Gao, Mechanical properties of refractory high-entropy alloys: Experiments and modeling, J. Alloys Compd. 696 (2017) 1139–1150.

doi:10.1016/j.jallcom.2016.11.188.

[37] S. Syed Ghazi, K.R. Ravi, Phase-evolution in high entropy alloys: Role of synthesis route, Intermetallics. 73 (2016) 40–42. doi:10.1016/j.intermet.2016.03.002.

[38] T.M. Butler, M.L. Weaver, Investigation of the phase stabilities in AlNiCoCrFe high entropy alloys, J. Alloys Compd. 691 (2017) 119–129. doi:10.1016/j.jallcom.2016.08.121.

[39] F. He, Z. Wang, Q. Wu, J. Li, J. Wang, C.T. Liu, Phase separation of metastable CoCrFeNi high entropy alloy at intermediate temperatures, Scr. Mater. 126 (2017) 15–19. doi:10.1016/j.scriptamat.2016.08.008.

[40] Y.F. Kao, S.K. Chen, J.H. Sheu, J.T. Lin, W.E. Lin, J.W. Yeh, S.J. Lin, T.H. Liou, C.W. Wang, Hydrogen storage properties of multi-principal-component CoFeMnTi xVyZrz alloys, Int. J. Hydrogen Energy. 35 (2010) 9046–9059. doi:10.1016/j.ijhydene.2010.06.012.

[41] I. Kunce, M. Polanski, J. Bystrzycki, Microstructure and hydrogen storage properties of a TiZrNbMoV high entropy alloy synthesized using Laser Engineered Net Shaping (LENS), Int. J. Hydrogen Energy. 39 (2014) 9904–9910. doi:10.1016/j.ijhydene.2014.02.067.

[42] I. Kunce, M. Polanski, J. Bystrzycki, Structure and hydrogen storage properties of a high entropy ZrTiVCrFeNi alloy synthesized using Laser Engineered Net Shaping (LENS), Int. J. Hydrogen Energy. 38 (2013) 12180–12189. doi:10.1016/j.ijhydene.2013.05.071.

[43] D. Karlsson, G. Ek, J. Cedervall, C. Zlotea, K.T. Møller, T.C. Hansen, J. Bednarčík, M. Paskevicius, M.H. Sørby, T.R. Jensen, U. Jansson, M. Sahlberg, Structure and Hydrogenation Properties of a HfNbTiVZr High-Entropy Alloy, Inorg. Chem. 57 (2018) 2103–2110. doi:10.1021/acs.inorgchem.7b03004.

[44] C. Zlotea, M.A. Sow, G. Ek, J.P. Couzinié, L. Perrière, I. Guillot, J. Bourgon, K.T. Møller, T.R. Jensen, E. Akiba, M. Sahlberg, Hydrogen sorption in TiZrNbHfTa high entropy alloy, J. Alloys Compd. 775 (2019) 667–674. doi:10.1016/j.jallcom.2018.10.108.

[45] C. Zlotea, M.A. Sow, G. Ek, J.P. Couzinié, L. Perrière, I. Guillot, J. Bourgon, K.T. Møller, T.R. Jensen, E. Akiba, M. Sahlberg, Hydrogen sorption in TiZrNbHfTa high entropy alloy, J. Alloys Compd. 775 (2019) 667–674. doi:10.1016/j.jallcom.2018.10.108.

[46] F.G. Coury, T. Butler, K. Chaput, A. Saville, J. Copley, J. Foltz, P. Mason, K. Clarke, M. Kaufman, A. Clarke, Phase equilibria, mechanical properties and design of quaternary refractory high entropy alloys, Mater. Des. 155 (2018) 244–256. doi:10.1016/j.matdes.2018.06.003.

[47] S. Guo, C.T. Liu, Phase stability in high entropy alloys: Formation of solid-solution phase or amorphous phase, Prog. Nat. Sci. Mater. Int. 21 (2011) 433–446. doi:10.1016/S1002-0071(12)60080-X.

[48] F. Tancret, I. Toda-Caraballo, E. Menou, P.E.J. Rivera Díaz-Del-Castillo, Designing high entropy alloys employing thermodynamics and Gaussian process statistical analysis, Mater. Des. 115 (2017) 486–497. doi:10.1016/j.matdes.2016.11.049.

[49] Y.F. Ye, Q. Wang, J. Lu, C.T. Liu, Y. Yang, The generalized thermodynamic rule for phase selection in multicomponent alloys, Intermetallics. 59 (2015) 75–80. doi:10.1016/j.intermet.2014.12.011.

[50] J. Montero, C. Zlotea, G. Ek, J. Crivello, L. Laversenne, M. Sahlberg, TiVZrNb Multi-Principal-Element Alloy : Sorption Properties, (2019).

[51] D.J.M. King, S.C. Middleburgh, A.G. McGregor, M.B. Cortie, Predicting the formation and stability of single phase high-entropy alloys, Acta Mater. 104 (2016) 172–179. doi:10.1016/j.actamat.2015.11.040.

[52] Y.F. Ye, Q. Wang, J. Lu, C.T. Liu, Y. Yang, Design of high entropy alloys: A single-parameter thermodynamic rule, Scr. Mater. 104 (2015) 53–55. doi:10.1016/j.scriptamat.2015.03.023.

[53] G.A. Mansoori, N.F. Carnahan, K.E. Starling, T.W. Leland, Equilibrium Thermodynamic Properties of the Mixture of Hard Spheres, J. Chem. Phys. 54 (1971) 1523–1525. doi:10.1063/1.1675048.

[54] A. Takeuchi, A. Inoue, Classification of Bulk Metallic Glasses by Atomic Size Difference, Heat of Mixing and Period of Constituent Elements and Its

Application to Characterization of the Main Alloying Element, Mater. Trans. 46 (2005) 2817–2829. doi:10.2320/matertrans.46.2817.

[55] A.M.G. Carvalho, D.H.C. Araújo, H.F. Canova, C.B. Rodella, D.H. Barrett, S.L. Cuffini, R.N. Costa, R.S. Nunes, X-ray powder diffraction at the XRD1 beamline at LNLS, J. Synchrotron Radiat. 23 (2016) 1501–1506. doi:10.1107/s1600577516012686.

[56] C. Suryanarayana, Mechanical alloying and milling, n.d.

[57] J.C. Slater, Atomic radii in crystals, J. Chem. Phys. 41 (1964) 3199–3204. doi:10.1063/1.1725697.

[58] F. Otto, Y. Yang, H. Bei, E.P. George, Relative effects of enthalpy and entropy on the phase stability of equiatomic high-entropy alloys, Acta Mater. 61 (2013) 2628–2638. doi:10.1016/j.actamat.2013.01.042.

[59] M. Venkatraman, J.P. Neumann, The Cr-Mn (Chromium-Manganese) system, Bull. Alloy Phase Diagrams. 2 (1981) 104–105. doi:10.1007/BF02873717.

[60] K.M. Youssef, A.J. Zaddach, C. Niu, D.L. Irving, C.C. Koch, A novel low-density, high-hardness, high-entropy alloy with close-packed single-phase nanocrystalline structures, Mater. Res. Lett. 3 (2014) 95–99. doi:10.1080/21663831.2014.985855.

[61] W. Sun, X. Huang, A.A. Luo, Phase formations in low density high entropy alloys, Calphad Comput. Coupling Phase Diagrams Thermochem. 56 (2017) 19–28. doi:10.1016/j.calphad.2016.11.002.

[62] X. Hou, R. Hu, T. Zhang, H. Kou, W. Song, J. Li, Hydrogen desorption performance of high-energy ball milled Mg2NiH4 catalyzed by multi-walled carbon nanotubes coupling with TiF3, Int. J. Hydrogen Energy. 39 (2014) 19672–19681. doi:10.1016/j.ijhydene.2014.09.170.

[63] H. Okamoto, H-Nb (Hydrogen-niobium), J. Phase Equilibria Diffus. 34 (2013) 163–164. doi:10.1007/s11669-012-0165-2.

[64] M. Dornheim, Thermodynamics of Metal Hydrides: Tailoring Reaction Enthalpies of Hydrogen Storage Materials, Thermodyn. - Interact. Stud. - Solids, Liq. Gases. (2011). doi:10.5772/21662.

[65] J. Bloch, M.H. Mintz, Kinetics and mechanisms of metal hydrides formation - A review, J. Alloys Compd. (1997). doi:10.1016/S0925-8388(96)03070-8.

Appendix I

The formulation for the calculation of excess entropy of mixture

According to the theory of Carnahan and Starling [50], the Z compressibility for mixtures of hard spheres can be expressed as

$$Z = [(1 + \xi + \xi^2) - 3\xi(y_1 + y_2\xi) - \xi^3 y_3](1 - \xi)^{-3} \quad (8A)$$

where:

$$y_1 = \sum_{j>i=1}^{m} \Delta_{ij}(d_i + d_j)(d_i d_j)^{-\frac{1}{2}} \quad (8B)$$

$$y_2 = \sum_{j>i=1}^{m} \Delta_{ij} \sum_{k=1}^{m} (\frac{\xi_k}{\xi}) \frac{(d_i d_j)^{\frac{1}{2}}}{d_k} \quad (8C)$$

$$y_3 = \left[\sum_{i=1}^{m} \left(\frac{\xi_i}{\xi}\right)^{\frac{2}{3}} c_i^{\frac{1}{3}}\right]^3 \quad (8D)$$

$$\Delta_{ij} = \left[(\xi_i \xi_j)^{\frac{1}{2}}/\xi\right]\left[\left(d_i - d_j\right)^2/d_i d_j\right](c_i c_j)^{\frac{1}{2}} \quad (8E)$$

$$\xi = \sum_{i=1}^{m} \xi_i \quad (8F)$$

$$\xi_i = \frac{1}{6}\pi\rho d_i^3 c_i \quad (8G)$$

where d_i is the atomic diameter of the ith element, c_i is the molar fraction of the ith element, ρ is the density number and ξ is the general atomic packaging fraction for a given ρ.

The excess entropy of mixture $S_E$is then expressed, in terms of c_i,, d_i and ξ, as follows:

$$\frac{S_E}{k_B} = \frac{(F - F^{id})}{k_B T} - lnZ - (3 - 2\xi)(1 - \xi)^{-2} + 3 + ln[(1 + \xi + \xi^2 - \xi^3)(1 - \xi)^{-3}] \quad (9A)$$

where

$$\frac{(F - F^{id})}{k_B T} = -\frac{3}{2}(1 - y_1 + y_2 + y_3) + (3y_2 + 2y_3)(1 - \xi)^{-1} + \frac{3}{2}(1 - y_1 - y_2 - \frac{1}{3}y_3)(1 - \xi)^{-2} + (y_3 - 1)\ln(1 - \xi) \quad (9B)$$

Appendix II

Classification of alloy systems according to φ parameter.

The following list displays the 11 alloy systems with the highest values of φ within the initial set of 60 systems and the MgTiNbCrMnNi system.

Alloy	Sc/kB	SE/kB	φ	Tm (K)	Ha/kB	r mean (Å)	δ (%)
$Mg_{22}Ti_{22}Nb_{22}Mn_{11}Fe_{11}Ni_{11}$	1.79	0.253	6.613	1809.56	209.65	1.39	9.10
$Mg_{22}Ti_{22}Nb_{22}Mn_{11}Co_{11}Ni_{11}$	1.79	0.247	6.292	1804.78	429.61	1.39	8.95
$Mg_{22}Ti_{22}Nb_{22}Cr_{11}Mn_{11}Ni_{11}$	1.79	0.248	6.149	1850.56	491.70	1.43	8.57
$Mg_{22}Ti_{22}Nb_{22}Mn_{11}Fe_{11}Co_{11}$	1.79	0.250	6.148	1814.00	459.90	1.39	9.03
$Mg_{22}Ti_{22}Nb_{22}Fe_{11}Co_{11}Ni_{11}$	1.79	0.301	5.005	1837.22	526.63	1.37	9.94
$Mg_{22}V_{22}Nb_{22}Mn_{11}Co_{11}Ni_{11}$	1.79	0.290	5.567	1858.56	325.43	1.36	8.94
$Mg_{22}Ti_{22}V_{22}Mn_{11}Fe_{11}Ni_{11}$	1.79	0.303	5.560	1683.56	178.69	1.36	9.29
$Mg_{22}Ti_{22}Nb_{22}Cr_{11}Co_{11}Ni_{11}$	1.79	0.295	5.559	1878.22	279.01	1.37	9.83
$Mg_{22}Ti_{22}Nb_{22}Cr_{11}Fe_{11}Ni_{11}$	1.79	0.302	5.307	1883.00	356.64	1.37	9.96
$Mg_{22}Ti_{22}Zr_{22}Cr_{11}Mn_{11}Fe_{11}$	1.79	0.316	5.206	1721.56	246.35	1.41	10.54
$Mg_{22}Ti_{22}V_{22}Cr_{11}Mn_{11}Ni_{11}$	1.79	0.298	5.203	1724.56	413.15	1.37	9.18
$Mg_{22}Ti_{22}Nb_{22}Fe_{11}Co_{11}Ni_{11}$	1.79	0.300	5.005	1837.22	526.63	1.37	9.93

Appendix III

The distribution of particle sizes of the alloys for both systems after HEBM was very broad, especially for those synthesized by MA, as can be seen in Fig. S1, S2, S3, and S4.

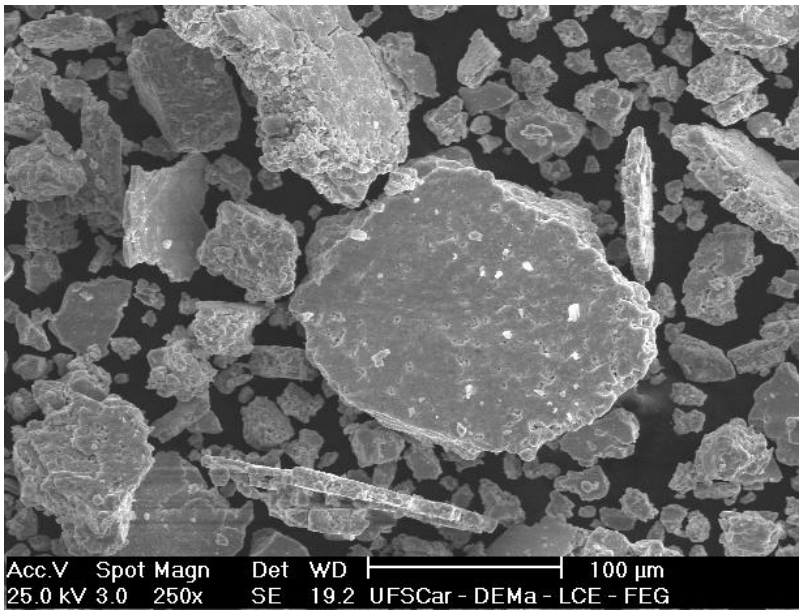

Figure S1: SEM image of the $Mg_{22}Ti_{22}Nb_{22}Cr_{11}Mn_{11}Ni_{11}$ MA right after synthesis. As the image exhibits, the MA synthesized particles have a flattened shape and the size of the particles ranges from 4 µm to 184 µm.

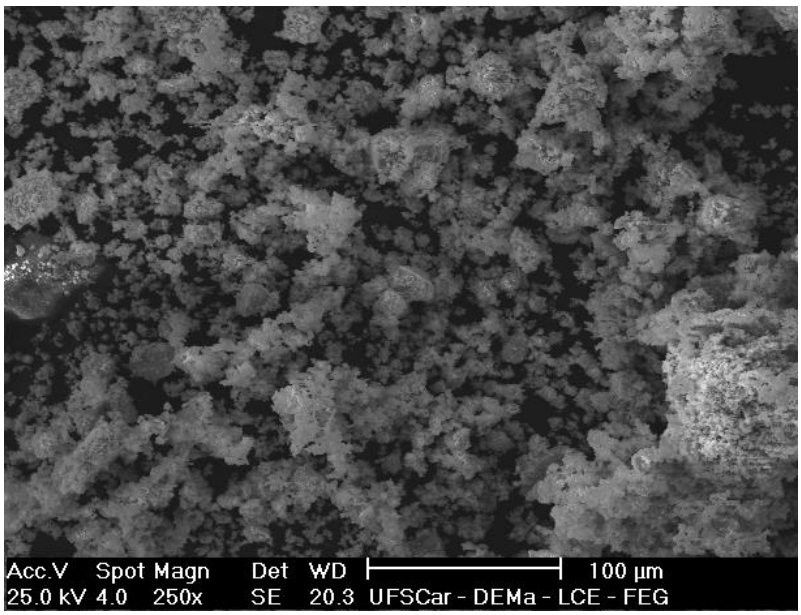

Figure S2: SEM image of the $Mg_{22}Ti_{22}Nb_{22}Cr_{11}Mn_{11}Ni_{11}$ RM right after synthesis. The alloy produced by RM exhibited smaller particle sizes and a more homogeneous distribution (from 2 µm to 48 µm) than that synthesized by MA.

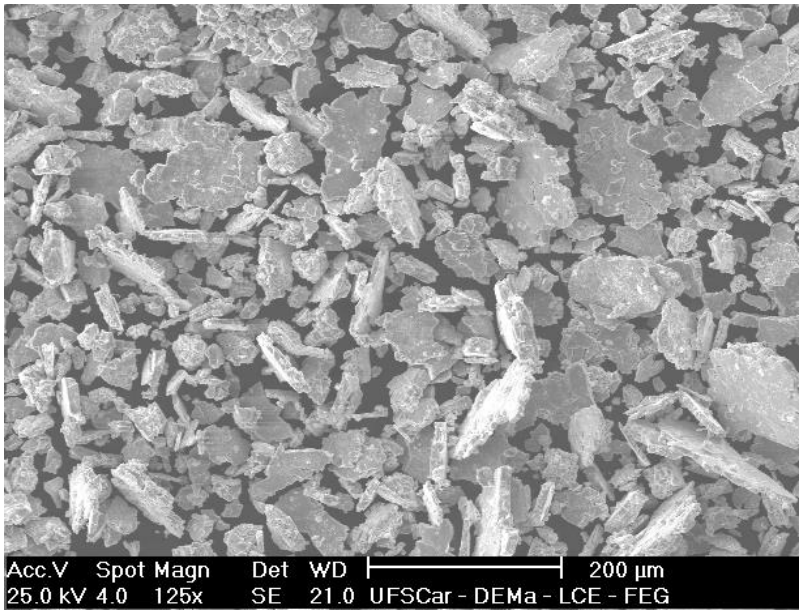

Figure S3: SEM image of the $Mg_{21}Ti_{31}N_{31}Ni_{17}$ MA right after synthesis. As the image exhibits, the MA synthesized particles have a flattened shape, and the size of the particles ranges from 8 µm to 200 µm.

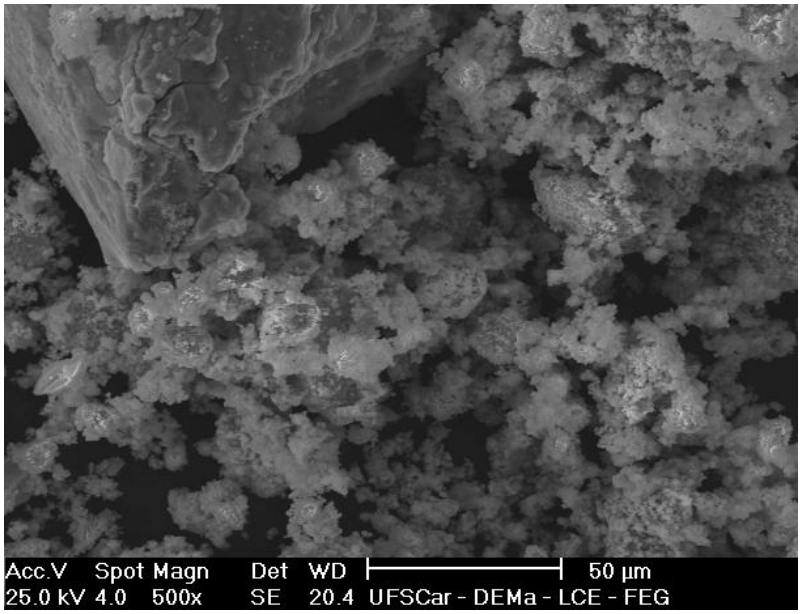

Figure S4: SEM image of the $Mg_{21}Ti_{31}N_{31}Ni_{17}$ RM right after synthesis. The alloy produced by RM exhibited smaller particle sizes and a more homogeneous distribution (from 2 µm to 100 µm) than that synthesized by MA.

In comparison to the MA-particles, the RM-particles have more homogeneous particle size distribution. Furthermore, it does not exhibit a flattened shape. This may be attributed to the mechanical properties of the

hydride phase since metal hydrides usually posses a lower ductility compared to the pure metals/alloys [65]. Alongside the broad particle size distribution, the presence of the compositional gradient between particles was identified by TEM-EDX analysis. Fig. S5 shows the microchemical analysis for a small particle of the $Mg_{22}Ti_{22}Nb_{22}Cr_{11}Mn_{11}Ni_{11}$ MA alloy. Disregarding the elements that certainly was not part of the system (Si, Co, and Al) and impurities (Fe and O), the quantification results presented in Fig. S6 diverges from the theoretical and average values exhibited in Table 5 of the main text, evidencing a sharp compositional gradient. It is worth noting that the particle analyzed in Fig. S5 is considerably smaller than the average particle size measured by SEM. Thus, this result must be analysed carefully. It shows that there exists some gradient of composition and that some elements, such as Mn and Mg, does not mix easily with the other elements of the alloy, which is in agreement with the XRD results presented in the manuscript. However, a quantitive analysis of such a composition gradient is rather difficult.

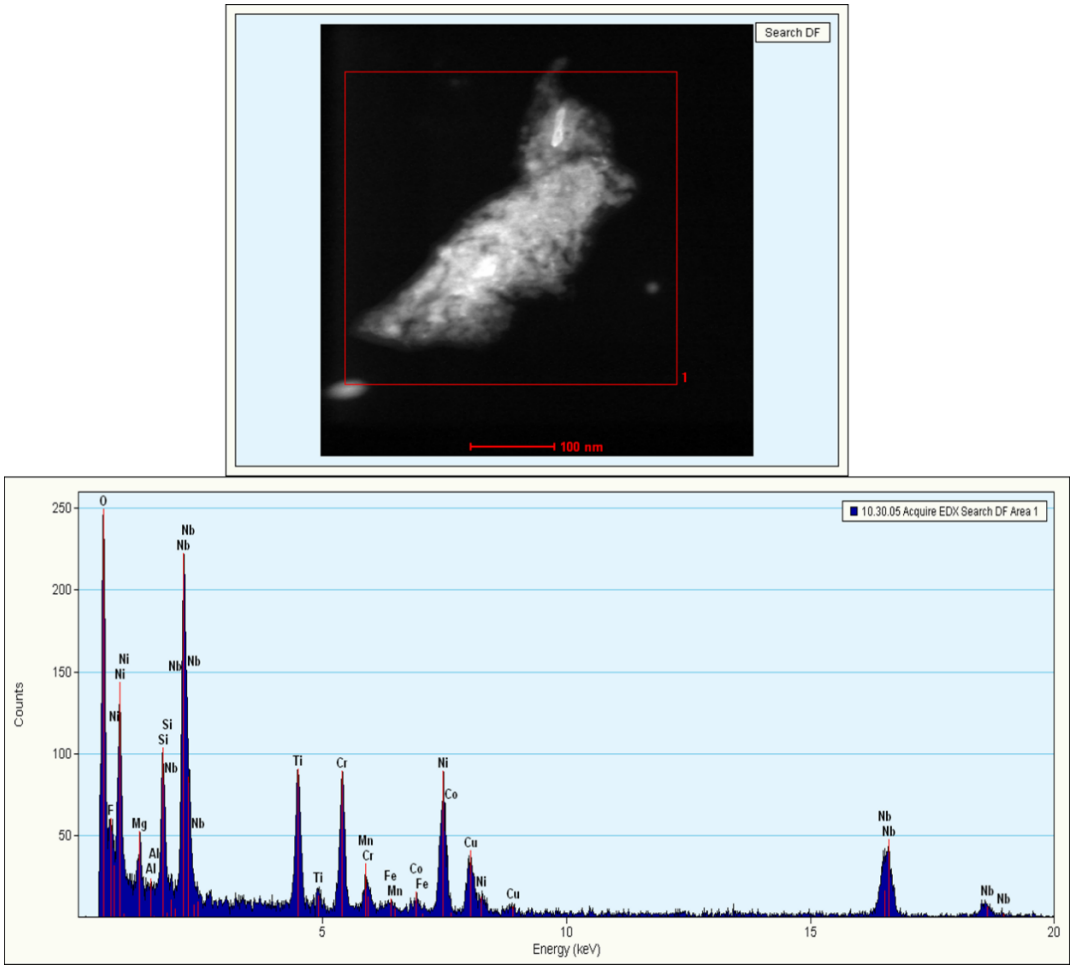

Figure S5: TEM image of the $Mg_{22}Ti_{22}Nb_{22}Cr_{11}Mn_{11}Ni_{11}$ MA alloy (top) and EDX spectrum of the selected region (bottom).

Quantification Results

Correction method: None

Element	Weight %	Atomic %	Uncert. %	Detector Correction	k-Factor
Mg(K)	1.15	3.00	0.18	0.88	1.046
Ti(K)	14.59	19.36	0.41	0.98	1.229
Cr(K)	16.96	20.72	0.48	0.99	1.304
Mn(K)	5.83	6.74	0.22	0.99	1.375
Ni(K)	20.38	22.06	0.54	0.99	1.511
Nb(K)	41.07	28.08	1.38	0.99	3.997

Figure S6: TEM-EDX quantification results of the $Mg_{22}Ti_{22}Nb_{22}Cr_{11}Mn_{11}Ni_{11}$ MA alloy.

Fig. S7 shows the microchemical analysis for a small particle of the $Mg_{22}Ti_{22}Nb_{22}Cr_{11}Mn_{11}Ni_{11}$ RM alloy. Disregarding the presence of oxygen impurities, the quantification results in Fig. S8 shows a slight variation in the composition compared to the theoretical and average ones. The slight variation exhibited by this alloy is much smaller than that presented by the MA alloy. The compositional gradient observed for the $Mg_{22}Ti_{22}Nb_{22}Cr_{11}Mn_{11}Ni_{11}$ alloy by EDX analysis is illustrative of the results obtained for the $Mg_{0.68}TiNbNi_{0.55}$ alloy (not shown here to be concise).

Moreover, cold welding is a common problem that may happen in ball-milling processes when ductile powder metal, such as Ti, Nb, and Ni are used. The loss of materials due to cold welding may unbalance the alloy composition [56].

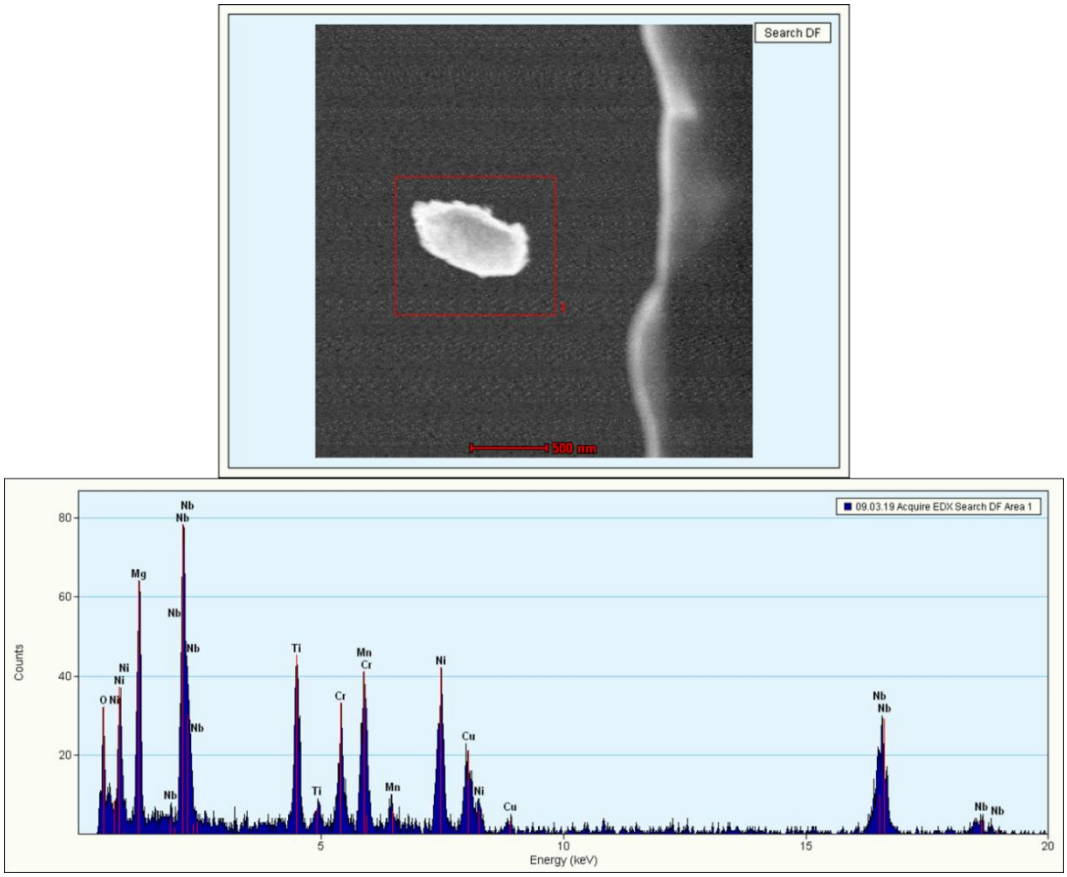

Figure S7: TEM image of the $Mg_{22}Ti_{22}Nb_{22}Cr_{11}Mn_{11}Ni_{11}$ RM (top) and EDX spectrum of the selected region (bottom).

Quantification Results

Correction method: None

Element	Weight %	Atomic %	Uncert. %	Detector Correction	k-Factor
Mg(K)	9.81	22.69	0.54	0.88	1.046
Ti(K)	13.88	16.28	0.60	0.98	1.229
Cr(K)	7.58	8.19	0.52	0.99	1.304
Mn(K)	16.11	16.47	0.70	0.99	1.375
Ni(K)	12.85	12.30	0.73	0.99	1.511
Nb(K)	39.74	24.03	1.92	0.99	3.997

Figure S8: TEM-EDX quantification results of the $Mg_{22}Ti_{22}Nb_{22}Cr_{11}Mn_{11}Ni_{11}$ RM alloy.

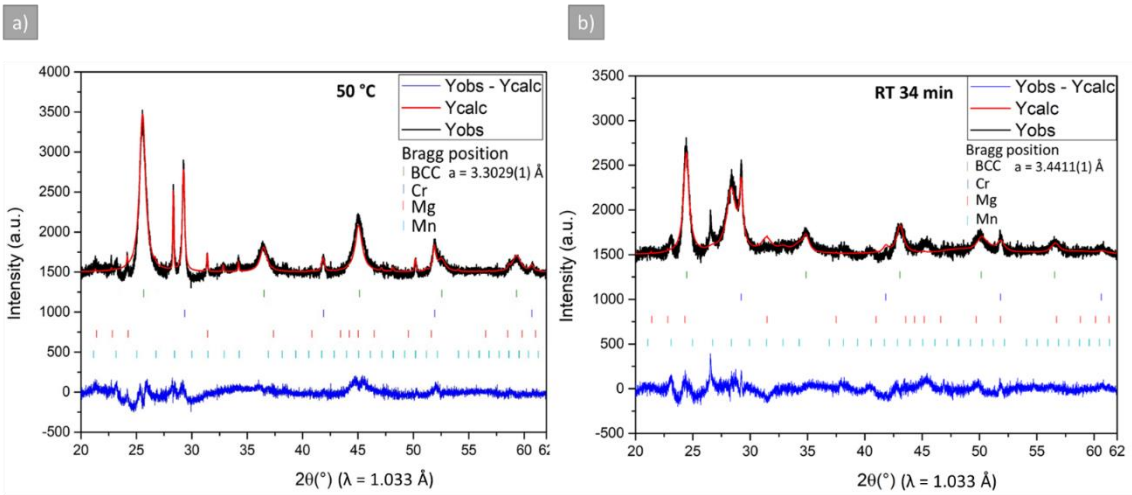

Figure S9 – Synchrotron powder XRD pattern for $Mg_{22}Ti_{22}Nb_{22}Cr_{11}Mn_{11}Ni_{11}$ MA and Pawley Fit results. a) at 50 °C at the beginning of the measurements; b) room temperature (RT) after 34 minutes of measurements.

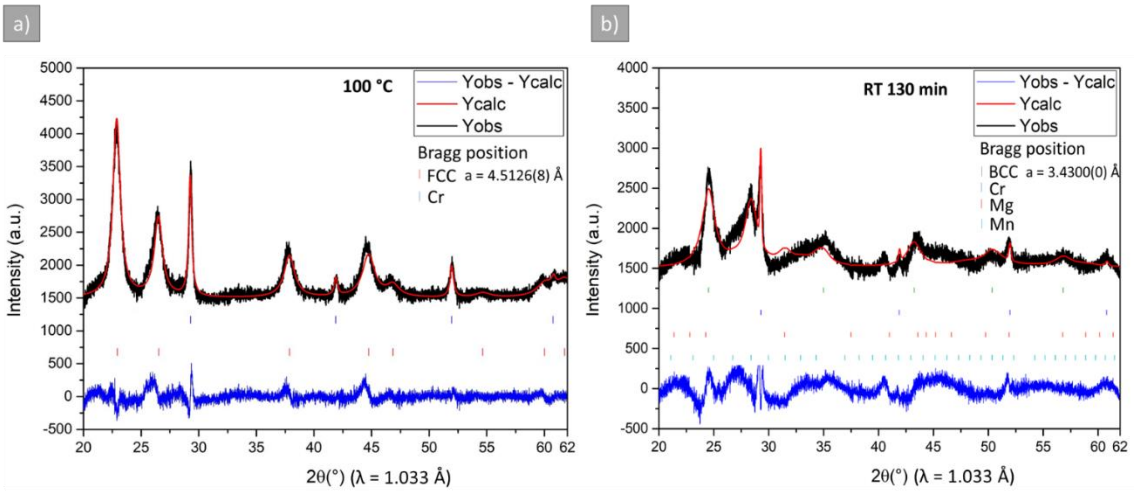

Figure S10 – Synchrotron powder XRD pattern for $Mg_{22}Ti_{22}Nb_{22}Cr_{11}Mn_{11}Ni_{11}$ RM and Pawley Fit results. a) at 100 °C at the beginning of the measurements; b) room temperature (RT) after 130 minutes of measurement.

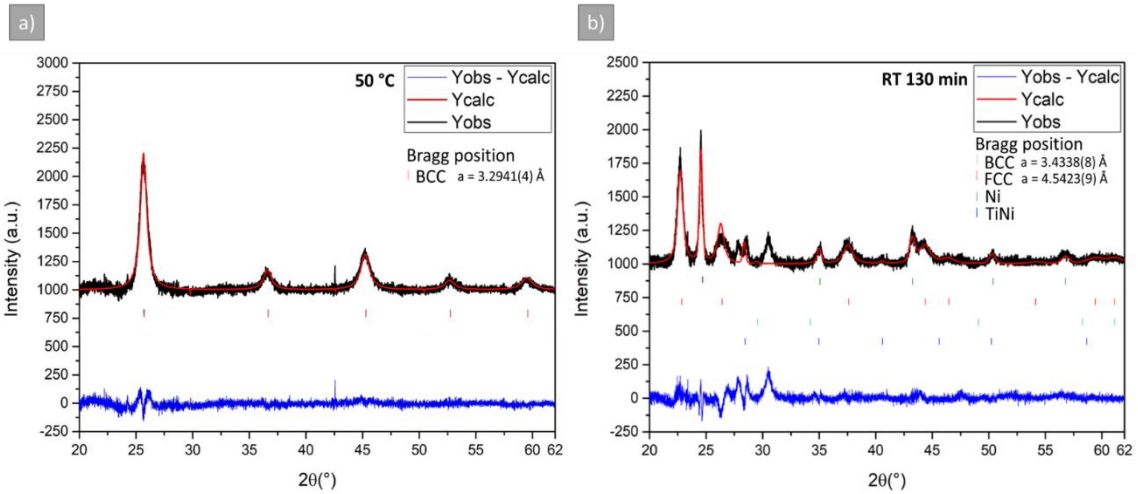

Figure S11 – Synchrotron powder XRD pattern for Mg21Ti31Nb31Ni17 MA and Pawley Fit results. a) at 50 °C at the beginning of the measurements; b) room temperature (RT) after 130 minutes of measurement.

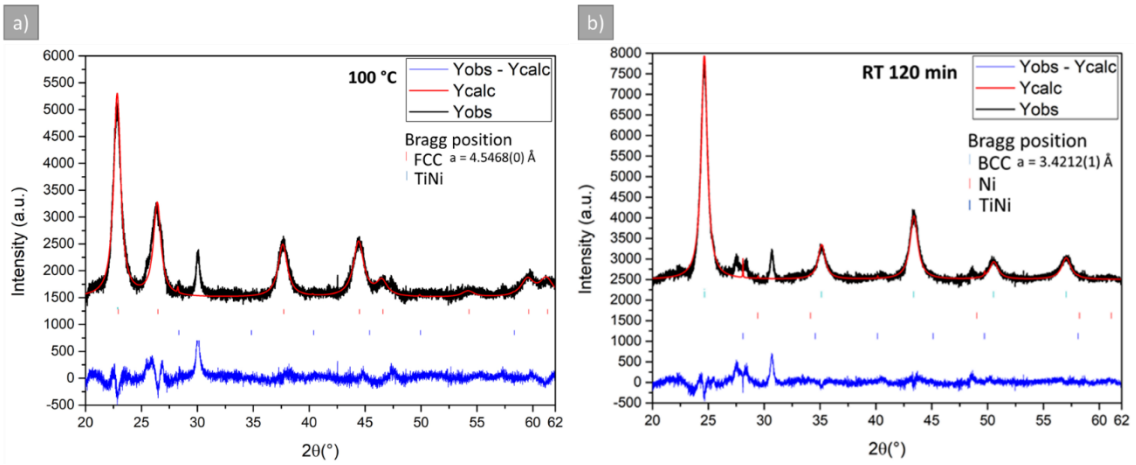

Figure S12 – Synchrotron powder XRD pattern for $Mg_{21}Ti_{31}N_{31}Ni_{17}$ RM and Pawley Fit results. a) at 100 °C at the beginning of the measurements; b) room temperature (RT) after 130 minutes of measurement.